The Relationship Between micro-Electrocorticography and Intracortical Signals

By

Thomas J. Richner

A dissertation submitted in partial fulfillment of
the requirements for the degree of

Doctor of Philosophy

(Biomedical Engineering)

at the

UNIVERSITY OF WISCONSIN-MADISON

2014

Date of the final oral examination: 5/8/2014

The dissertation is approved by the following members of the Final Oral Committee:
Justin C. Williams, Associate Professor, Biomedical Engineering
M. Elizabeth Meyerand, Professor, Biomedical Engineering, Medical Physics
Barry D. Van Veen, Professor, Electrical and Computer Engineering
Willis J. Tompkins, Professor, Biomedical Engineering
Kevin Eliceiri, Director, LOCI, Biomedical Engineering

© Copyright by Thomas J. Richner 2014
All Rights Reserved

To my Parents and Grandma

Acknowledgments

I would like to thank my advisor, Justin Williams. Your patience, creativity, optimism, and collaborative spirit are among many qualities you instill in those around you. Thank you for the opportunity to explore new paths knowing that you would be a champion of the result. I have never more enjoyed working for someone.

Thank you, Lisa Krugner-Higby. I am entirely obliged, but I can only begin to list all of the generous ways you have guided and supported this work from beginning to end. In the beginning, you patiently trained this inexperienced engineer in a field entirely un unfamiliar. Throughout, you persistently raised expectations for the quality and refinement of all of our experimental work. In hard times, your excellent wit matched your diagnostic skill. Most recently, you have been an incredible editor and teacher. Thank you for trying to teach me how to write. I wish you many more enjoyable and productive research-vacations and vacations from research too.

Thank you, Samuel Poore. I never expected to meet another primary investigator with the patience, creativity and optimism like that of Justin's, but you were his perfect match. You were always thoughtful and wonderful to work for. You and Sahil Kapur developed exciting avenues of research that I am happy to have been part of. Sahil, I reflect happily on our late night experiments and your incredible drive.

Ramin Pashaie, thank you for the opportunity work with your excellent lab members and the amazing optical systems you develop. You have played a considerable role in shaping my research path. When writing research grants, your ideas leapt off the page—if only I could have better captured them. I hope we can find collaborations in the future. Thank you, Ryan Baumgartner for the opportunity to work with you, for your drive, and for putting together a great piece of equipment.

Kevin Eliceiri, you provided direction when my research path wavered, built collaborations essential to this work, and provided an environment for innovative work. Thank you to all of your lab members and especially Joseph Szulczewski and Pam Young.

Thank you to Dan Moran for introducing me to neural engineering and to Justin Williams. Discussions with you motivated chapter 3.

Thank you to lab all members current and past. Joeseph Hippensteel, you taught me in a summer what would have taken me multiple years on my own. On your last night before med school in the summer of 2008, you gave me a mandate to get *in vivo* micro-ECoG testing going. As a character, you are a peer and a role model. Sanitta Thongpang, you increased the standards for quality and productivity among grad students in our lab through example. You showed us what was possible. Further, you made this work possible. I am grateful to have learned how to go about research from you. Sarah Brodnick, no single person did more than you to make this work possible. You always went beyond expectations in dedication to the lab. Your efforts, and our discussions on how to proceed experimentally, improved the every ounce of data of every experiment in this document. This document would be much shorter without Amy Schendel's efforts. Thank you for entertaining far-ranging discussions on materials their application to the brain. Thank you Jiwan Kim for pioneering micro-ECoG fabrication in our lab. Thank you, Steven Skroch; your ideas seeded several productive routes of research found in this document.

Thank you to my committee. Professor Meyerand, I appreciated your constructive feedback and encouragement. Thank you, Professor Tompkins. Your digital signal processing course was the most essential class I have taken with respect to this work. I use what I learned from you nearly every day. Thank you, Dr. Sillay. Your questions helped improve the formulation of these ideas. Thank you, Professor Van Veen. I appreciated the opportunity to learn from you during weekly meetings.

Importantly, I would like to acknowledge American taxpayers. Their funding of science and engineering grows our society. I would like to thank the National Institute of Biomedical Imaging and Bioengineering (T90 DK070079, 1R01EB009103-01). This work was sponsored by the Defense Advanced Research Projects Agency (DARPA) MTO under the auspices of Dr. Jack Judy through the Space and Naval Warfare Systems Center, Pacific grant/contract no N66001-12-C-4025.

Table of Contents

Introduction and Overview

Improving neural interfaces and the understanding of the signals they record are ongoing engineering pursuits with potential clinical and basic research applications. Neural interfaces can be used to implement sensorimotor neuroprostheses, to map epileptic neural activity, and to study systems neuroscience more generally in animal models. The technological approaches can be tailored to interfaces at various levels of the central and peripheral nervous systems, from individual neurons to the superimposed activity of neural populations. Further, indirect measures that are causally linked to neural activity (e.g. blood oxygenation) can be targeted, often with the added benefit of reduced invasiveness.

There is a fundamental tradeoff between the invasiveness of a neural interface and the quality of the signal it records [1]. At one end of the spectrum, microwire arrays record information rich action potentials (spikes) within the cortex, and at the other end of the spectrum, electroencephalography (EEG) electrode caps record information poor, low frequency potentials from the surface of the scalp. Between intracortical and scalp recordings, lies electrocorticography (ECoG) and its microfabricated counterpart, micro-ECoG. ECoG and micro-ECoG utilize flat grids of electrodes that rest on surface of the brain, above or below the dura mater. They are as close to the brain as possible without penetrating into the cortex. Residing in this middle ground, micro-ECoG signals lack the spikes that give intracortical extracellular recordings definition. Lacking spikes is not a disadvantage in the long run for chronically implanted devices, because recordings from penetrating intracortical arrays are known to degrade over a period of months through a process of gliosis until spikes can no longer be recorded [2]. Thus, implanting arrays on the surface of the brain strikes a balance between invasiveness and signal quality, but quantifying the quality of the micro-ECoG signal by relating it intracortical signals remains an ongoing area of research.

Relating less invasive signals to more grounded intracortical signals is a theme that applies beyond the electrophysiological study of the cortex. Hemodynamic and metabolic signals subsequent to neural activity are at the center of two important brain imaging methods: functional magnetic resonance imaging

(fMRI) and positron emission tomography (PET). Quantifiably pinning hemodynamic and metabolic signals to the neural activity that generated them, the study of neurovascular and neurometabolic coupling, provides a physiological basis to use these less invasive neural imaging techniques.

Neurovascular coupling, neurometabolic coupling, and the linkage between spikes and micro-ECoG area causal by nature, so bidirectional neural interfaces that actively modulate neural activity (i.e. the input) in addition to passively recording and imaging neural signals (i.e. the outputs) are well suited to the study of these mechanisms. Optogenetics, the use of light sensitive ion channels and pumps to modulate neural activity, is a new technology for actively interrogating a genetically targeted subset of neurons with high temporal resolution due to the rapid kinetics of the ion channels employed [3–5]. Due to the ease of patterning light with modern optics, optogenetics also has high spatial resolution. Given the MRI compatibility of optical fibers, optogenetics was readily applied in conjunction with fMRI [6,7]. Optogenetics was also incorporated with fluorodeoxyglucose (FDG) PET [8]. These whole brain imaging methods resolve voxels at the millimeter scale. Optical imaging methods integrating optogenetics could be used to investigate hemodynamic and metabolic signals at the micrometer scale, and micro-ECoG arrays could be customized to facilitate optogenetic photostimulation of the cortex. Combining optogenetics with imaging and recording methods could create bidirectional technology platforms to study neurovascular coupling, neurometabolic coupling, and the micro-ECoG signal [9].

This dissertation begins with two review chapters on topics that are most relevant to the four chapters of original research that follow. Chapter 1 is a review of micro-electrocorticography (micro-ECoG) signals and how they relate to ECoG signals and intracortical activity. This chapter provides a foundation for chapter 2. The third chapter reviews the use of optogenetics to study neurovascular coupling. This chapter provides a brief introduction to optogenetics, a method used in chapters 4, 5 and 6 of this dissertation, and specifically addresses its recent application to studying hemodynamics in the brain. This chapter also includes a review of prior approaches using optogenetics to study neurometabolic coupling, only a few examples exist and they were integrated into this chapter under the framework

neurovascular coupling. Chapter 2 gives an extended background to support the research presented in chapter 6.

The four original research chapters, 3-6, correspond to submitted or published manuscripts (see table 1), and retain the structure of a journal article. The introduction for each chapter was retained as a more chapter specific supplement to the reviews in chapters 1 and 2. The topics of chapters 3-6 chronologically reflect a research process that began with electrophysiological investigations into micro-ECoG (chapter 3), continued with the methodological addition of optogenetics to probe both the central (chapter 4) and peripheral (chapter 5) nervous systems, and finished with a broader investigation of neurovascular and neurometabolic coupling in the cortex (chapter 6). The evolution of the methods employed in these experiments, reflected both the major movements within the field and the addition of collaborators who brought new technologies and capabilities. The overarching theme of these four chapters was the application of neural interfaces and imaging systems to gain insight into the intracortical underpinnings of signals recorded from the surface of the brain.

Table 1. Correspondence between dissertation chapters and publications.

Chapter 3	(Submitted) "The relationship between micro-ECoG and intracortical recordings"
Chapter 4	(Published) Richner T J, Thongpang S, Brodnick S K, Schendel A A, Falk R W, Krugner-Higby L A, Pashaie R and Williams J C 2014 Optogenetic micro-electrocorticography for modulating and localizing cerebral cortex activity *J. Neural Eng.* **11** 016010
Chapter 5	(Submitted) Richner T J, Brodnick S K, Kapur S, Schendel A A, Krugner-Higby L A, Williams J C and Poore S O 2014 Transcutaneous optogenetic mapping of sensory cortex *Journal of Neural Engineering*
Chapter 6	(In review) Richner T J, Baumgartner R, Brodnick S K, Eliceiri K W and Williams J C 2014 Optogenetic mapping of neurovascular and neurometabolic coupling *Journal of Cerebral Blood Flow & Metabolism*

Chapter 1. The micro-electrocorticography signal

1.1 Overview

Micro-ECoG arrays reside in a spatial middle ground between clinical ECoG grids and intracortical microarrays. Consequently, micro-ECoG shares a subset of ECoG and intracortical signal characteristics. Similar to ECoG, micro-ECoG provides a two-dimensional view of the potentials on the surface of the cortex with greater resolution due to electrode densities approaching those of intracortical microarrays.

Unlike intracortical recordings, micro-ECoG signals lack action potentials (spikes). Spikes provide temporal definition to extracellular intracortical recordings, and, in doing so, they give confidence to the researcher. Spikes have a high signal to noise ratio, a well understood origin in voltage gated ion channels, and they are known to originate within a short distance to the recording site. Upon immediate inspection of micro-ECoG signals, these reassurances are missing. While spikes are digital, micro-ECoG is analog. The signal to noise ratio is hard to define; rather, the difference between micro-ECoG signal and noise is not readily apparent. Mechanistically, the micro-ECoG signal is more of an epiphenomenon of cells acting in concert rather than the output of a single cell, and the spatial origin of the micro-ECoG signal is a superposition of spatially distributed sources, similar to ECoG and EEG.

1.2 micro and macro ECoG

Modern micro-ECoG has it historical origins neurosurgical ECoG. Rather than a technology translated from research lab to clinic, micro-ECoG is a technology taken out of the operating room and miniaturized in the research laboratory. Some of these miniaturized arrays are now making their way back into the clinic [10,11]. ECoG's primary developer was Wilder Penfield who used discretely wired electrodes individually positioned on the cortex to map the cortex and localize epileptic activity [12,13]. Besides mapping the sensory and motor homunculi, he proved that epilepsy is not a disease of the spirit but an electrical disease of the brain. ECoG is still widely applied to map epileptic neural activity, and grids of platinum electrode sites embedded in silicone have replaced discretely placed electrodes. The

large site area and centimeter spacing between sites of clinical grids suffice to record the millivolt signals generated by epileptic tissue.

Beyond mapping epileptic foci, ECoG signals have been used to implement brain computer interfaces (BCIs) and study the cortex more generally [14–18]. When clinically indicated, ECoG grids are implanted in patients with epilepsy for sometimes as long as two weeks to map epileptic regions. This period provides the opportunity for researchers to tap into the ECoG signals to do BCI [14–18], motor [19,20], auditory [21–23], and speech [24–26] research. Progress in these research areas using the existing and rather limited ECoG arrays inspired engineers to develop micro-ECoG arrays as the next step in BCIs and cortical electrophysiology.

Micro-ECoG array technology is developing along two routes: miniaturized clinical grids and microfabricated arrays. Miniaturized clinical grids are made by hand using the same techniques and materials as standard grids so that they can be more rapidly approved for use in human beings [10,11]. Microfabricated arrays use a wider array of processes (usually photolithography) and materials [27–32]. Usually a combination of insulative polymers sandwich metal conductive layers. The processes are highly repeatable and enable smaller features to be constructed, so electrodes with very high site density (sites/area) can be fabricated. Integrated amplification and multiplexing is pushing the site density orders of magnitude higher [33]. However, increased site density does not necessarily lead to proportionately more information extracted from the brain since neighboring sites are increasingly correlated as the site-to-site distance decreases. This will be explored in greater detail later in sections synthesizing electrode design with the biophysics of micro-ECoG signal generation.

1.3 Signal Characteristics of ECoG

Toward developing a complete conceptualization of the micro-ECoG signal, observed characteristics, intuition and experimental results can be drawn from (macro) ECoG to provide a starting point. Particular signal characteristics have been given extra attention during the development of ECoG as a field of study. The gamma band, broadband, cross-frequency coupling, and event related

desynchronization are major themes in the literature. Each of these gained attention for their utility and their ability to be modulated by experimental conditions. Studying the mechanisms that generate these signals is of major interest as it provides a neurophysiological basis to the research.

The gamma band, signals above 30 Hz, became a major signal of interest to the ECoG community following pioneering work by Nathan Crone [34]. Changes in lower frequencies were more often studied prior to this [35,36], and Crone introduced his work in the gamma band alongside his own work in alpha and beta event-related desynchronization [37]. Gamma band power increases during motor movements, while lower frequencies decrease [34]. When mapped onto the cortex, changes in gamma power localize to much smaller areas than changes in low frequencies [34], increasing spatial resolution, the ability to separate two areas. Subsequently, the gamma band was correlated to word production [38], auditory perception [39], letter perception [40], and motor movements [34,41–43]. Correlative and more recently causative studies have grounded gamma frequency signals in neurophysiological mechanisms. Population spiking rate correlates with gamma power [44]. The blood oxygen level dependent (BOLD) signal also follows the population spiking rate and gamma power [45–48], suggesting that gamma correlates with regional increases in metabolism due to increased spiking. Optogenetics has been used more recently to interrogate gamma frequency signals in a causative and cell type-specific manner. Voltage clamp experiments in brain slices and *in vivo* show that excitatory postsynaptic potentials (EPSPs) and inhibitory postsynaptic potentials (IPSPs) occur out of phase at gamma frequencies when the cortical circuit is driven with constant (i.e. not pulsed) channelrhodopsin-2 (ChR2) stimulation of the pyramidal cells [49]. Excitatory glutamatergic cells fire during the downward phase of the gamma signal and inhibitory GABAergic cells fire during the upward phase. Brain slice studies may have considerable confounds due to the preparation, but complementary studies *in vivo* with mice expressing ChR2 in inhibitory interneurons support the *in vitro* work. Prolonged optogenetic stimulation of pyramidal neurons [49,50] or parvalbumin inhibitory interneurons [51] leads to increased gamma. These findings that gamma is correlated with population spiking rate and that inhibitory interneurons set up gamma

frequency oscillations are not mutually exclusive, but perhaps part of a bigger picture. One possible unifying hypothesis is that as pyramidal (i.e. excitatory) activity increases, inhibitory interneurons are recruited, providing negative feedback and maintaining balance between excitation and inhibition. Whether the focus is on population spiking rate, or out of phase excitatory and inhibitory neurons, there would be a correlation to gamma.

The amplitude the gamma signal is often observed to be coupled to the phase of low frequency (<10 Hz) oscillation [40,52–56]. Phase-amplitude coupling, alternatively known as cross frequency coupling, occurs when the amplitude of a higher frequency band is modulated by the phase of a lower frequency oscillation [57]. High gamma (>80 Hz) was found to occur preferentially during the downward phase of theta (4-8 Hz) oscillation in ECoG recordings from human subjects [52]. If high gamma correlates to the population spiking rate, then phase-amplitude coupling predicts that spikes should be phase coupled as well. Phase-amplitude coupling is correlated to the population spiking rate [54]. Phase-amplitude coupling has not been reported in micro-ECoG signals, but there are not biophysical reasons to suggest that this signal characteristic is only found in larger arrays.

More recently, broadband shifts in the power spectrum have been pushed forward, often to the exclusion of the gamma band concept [58–61]. Broadband power changes occur over the entire frequency domain and are in contrast to bandlimited peaks in the power spectrum. Kai Miller, the major proponent of this reconceptualization, observed that changes in the "high gamma" band do not seem to have an upper frequency limit except for the noise floor of the recording amplifier [61]. The relationship between power and frequency follows a power law with $P(f)=1/f^k$ for some constant k. The power law seems to hold in upper frequencies, and less well in lower frequencies. Miller proposes that alpha and beta oscillations mask broadband effects at low frequencies [59,61]. These large slow oscillations increase the variance of the power at the lower frequencies, so that when the Z-score is applied to renormalize the spectrum, broadband changes from 0-20 Hz are not as apparent. Miller uses spectral Eigen vector analysis to separate these low frequency changes from broadband changes [58]. The

difference between gamma band and broadband conceptualization is not only in the nomenclature. Crone initially called increases in upper frequencies event related synchronization of gamma, implying that increased gamma correlates to increased synchronization [34]. Increased broadband, in contrast, indicates more asynchronous activity. Pink and brown noise are examples of processes with 1/f and 1/f^2 power spectra, respectively. ECoG recordings from the brain usually fall somewhere between 1/f^2 and 1/f^4. These scale invariant processes are indicative of random rather than synchronous activity. According to Miller, "...the approximately power-law profile of the broadband component can be understood as the signature of the summation of asynchronously arriving synaptic inputs in the dendrites of pyramidal neurons."[61] Therefore gamma band and broadband conceptualizations are distinct and competing hypotheses.

Prior to major interest in gamma band and broadband signal, more attention was paid to event related desynchronization in lower frequency signals (<20 Hz) [35,36]. Desynchronization is a concept commonly used to explain the transient fluctuations between oscillatory and relatively flat signals observed with ECoG and electroencephalography (EEG) [36]. Attention [62–65], cognitive load [66], working memory tasks [66–69], and motor movements [70–74] are correlated with synchronization/desynchronization. The hypothesized mechanisms are based on synchronized neural activity superimposing constructively and desynchronized neural activity superimposing destructively [36]. Oscillators that are in phase and spatially oriented similarly will add, while out of phase oscillators will cancel. The default, unattending, brain state is thought to have greater synchrony (and larger oscillations) than during attention to a complex task. Besides the vast literature of EEG and ECoG research contingent on this hypothesis (reviewed in ref. [36]), evidence supporting the desynchronization concept came from *in vivo* dual patch clamp experiments in mice that demonstrated that neighboring neurons are more synchronous during strong oscillations [75]. Large oscillations can also be induced pharmacologically.

Drugs with well understood anesthetic mechanisms can be used to experimentally modulate neural activity and the resulting changes in ECoG power spectrum can provide additional insight into the linkage between neurophysiology and signal characteristics. Many of the drugs that have been studied in relation to ECoG are those used for anesthesia or sedation during intracranial surgery. Dexmedetomidine is used during awake craniotomy for cortical mapping in human subjects [76–78]. It agonizes the α-2 adrenergic receptors in the locus coereleus and leads to an inhibitory potassium current, and this inhibition of the locus coereleus operates along NREM sleep promoting pathways to cause sedation [79]. Akin to deep sleep, ECoG signals under dexmedetomidine have large slow oscillations and less high frequency power [80]. How these changes in power spectrum are reflected in cortical neuron spiking have not been directly studied, but we can hypothesize that these large slow oscillations are a result of more phase locked spiking.

1.4 Biophysics & anatomic structure

The biophysics and anatomic organization of the cortex govern the generation of the micro-ECoG signal. The cerebral cortex has a heterogeneous layered organization with disproportionately more cell bodies in some layers and neurites in others. Dendritic currents are thought to play the major role in the generation of local field potentials (LFPs), ECoG and micro-ECoG signals, because dendrites have a relatively large area relative to axons and somas, and dendritic currents occur over long time constants and therefore are more likely to summate [57]. When cations enter the dendrites they leave behind a net negative charge, a sink, that must be rapidly balanced by the movement of charged ions from nearby sources [81,57]. This pairing of sinks with sources constitutes a dipole. The dipole theory of EEG and ECoG signal generation holds that these ions are sourced from dendrites due to their large area and therefore low net resistance. Current dipoles responsible for the EEG and ECoG signals have an assumed orientation perpendicular to the surface due to the disproportionate share of dendrites in the upper layers of the cortex and cell bodies in the lower layers, and dipoles parallel to the cortical surface array are difficult sense due to isopotential lines [82]. The electrostatic forward model (i.e. Maxwell's equations)

tells us how the electric field and the negative gradient of the electric field, the potential, depend on the distance to and the orientation of the dipole or dipoles [82]. Electrostatics guarantees that the resulting potential due to multiple dipoles is the superimposed result of each individual dipole, so a micro-ECoG recording is really a spatially weighted superposition of signal sources within the cortex or even deeper. Within the cortex, dipoles are usually assumed to be oriented vertically, perpendicular to the cortical surface, due to the vertically layered structure of the cortex, and therefore these dipoles are perpendicular to micro-ECoG arrays which are implanted above or below the dura.

The signal quality and therefore the merits of recording micro-ECoG and ECoG from arrays implanted below the dura versus on top of the dura is debated. The dura matter is a fibrous membranous tissue that is about 0.4 mm thick in humans [83]. Signal quality depends on the proximity of electrodes to their source, so undoubtedly subdural recordings have greater signal quality. However, the degree to which subdural recordings are superior to epidural recordings, and whether the added invasiveness of subdural recordings is justified, is where the debate lies. Epidural and subdural recordings using clinical micro-ECoG and ECoG arrays have been directly compared in human beings. There is a marked decrease in signal amplitude in epidural recordings, especially for micro-ECoG arrays [84]. However, the clinical micro-ECoG arrays used in this study were simply cleaved 75 μm microwires embedded in silicone[84]. The relatively small site area accounted for the observed differences according to their finite element model [84]. Optimizing the electrode site area appears to be essential. The degree to which the dura plays a role likely depends on the species. The dura of the mouse may be relatively negligible compared to that of primates. The epidural versus subdural issue can also be approached through modeling.

Electrostatic models help describe how current sources result in cortical potentials and how electrodes should be designed as a result. A 3D realistic finite element model has been made of both the rat and human head [83]. The model showed that cerebral spinal fluid (CSF) between the dura and brain played a more significant role than the dura itself. When a CSF filled separation between the brain and

dura was modeled, human epidural recordings had a longer spatial fall off due to a current dipole than rat epidural recordings. However, when the CSF was compressed, the spatial-potential characteristics of human and rat epidural models were very similar [83], suggesting that the thickness of the CSF gap under the dura, not the thickness of the dura, is the important factor. This prediction remains to be verified experimentally. In addition to tissue properties and geometry, electrode material properties and geometry affect signal quality. Finite element modeling of how electrode site area affects signal sensitivity as a function of distance between the site and source suggests that large sites are more sensitive over longer distances [84,85]. After site area, site-to-site spacing is the other major consideration when designing micro-ECoG arrays.

The optimal spacing between electrode sites depends on the properties of the neural signals and the biophysics involved. Intuitively, if electrode sites are place very close together, they record mostly the same signal and are redundant, with no added information. A precise optimal spacing likely does not exist, but instead there is a tradeoff between site-to-site spacing and site-to-site correlation. The most simplistic way to answer this question is that the Nyquist criterion defines the highest spatial frequency that can be resolved [81], and this should be considered against the minimum distance between neural sources relevant to the experiment. The hindlimb and forelimb sensory cortex regions are a mere 0.5 millimeters apart in the mouse [86]. Careful sensory mapping or new tools such as optogenetics could be used to experimentally test the optimal electrode site spacing.

1.5 Link to intracortical signals

Empirically establishing both correlative and causative links between cortical surface potentials and intracortical signals would build a neurophysiological basis for understanding and applying micro-ECoG. Correlative relationships are established by comparing two simultaneously recorded signals. Potentials recorded at two electrode sites can be compared directly, or a potential recording can be compared to a set of spike times by converting the spike times to a continuous spike rate signal or with more advanced analysis (e.g. complex cross coherence). Causal links can also be calculated from

simultaneously recorded data by testing whether the history of one signal helps predict the future of a second signal beyond the second signal's own history [87]. Alternatively, cause and effect relationships can also be experimentally tested by manipulating one variable while observing the other. Optogenetics (which is introduced in section 2.2) gives us tools for the manipulation of transmembrane currents and therefore spiking activity to test causal electrophysiological relationships. Lacking optogenetic manipulation, recordings of spikes from intracortical electrode arrays can be compared to simultaneously recorded micro-ECoG to test for correlative relationships. There is a considerable literature of comparisons between spikes to LFPs to draw upon.

Phase coupling between spikes and LFPs (spike-field phase coupling) is commonly observed in intracortical recordings [88–96]. Spike-field phase coupling is a ubiquitous phenomenon across cortical regions and experimental paradigms. Visual stimulation [88,94], motor movement [90,91,96], motor planning [93], and memory tasks [92], elicit spike-field phase coupling. The majority of these examples have phase coupling at relatively low frequencies (<35 Hz). Spike-field phase coupling and phase-amplitude coupling occur in tandem, especially with low frequency phase entraining [54,97]. Higher frequency spike-field phase coupling appears to be specific to the neural circuitry of certain brain regions. For example, gamma frequency spike-field phase coupling and phase-amplitude coupling is observed in the hippocampus [98]. The degree to which deeper brain structures entrain the cortex and volume conduction from deeper structures contributes to cortical LFPs [99], complicates the interpretation of physiological interpretation of spike-field phase coupling recorded in the cortex. Brain slice recordings can be used to avoid effects from deeper structures and to dissect the necessity of specific cortical layers to spike-field phase coupling [89]. Careful transections between the layers of the cortex found that layer 5 may serve as a generator of phase-amplitude coupling in the cortex [89]. The pyramidal neurons were phased entrained at 5-10 Hz and the glutamatergic synapses may entrain other cortical areas.

The phase of spike-field coupling may depend on the cortical layer and cell type. Neurons recorded from deeper cortical layers have been reported to fire preferentially during the downward phase

of the LFPs and those recorded from upper layers fired during the upward phase [90]. Large pyramidal neurons are found in layers 4-6 while inhibitory interneurons are found in layers 2-3, so a correspondence between cell type and phase can be hypothesized. Models investigating LFP suggest that different cell types have different relative contributions based on their location, connectivity, and morphology [100]. The original publication introducing current source density (CSD) analysis suggests that cell location, morphology, and, additionally, how the neurons are activated (i.e. depolarized) results in sources and sinks in different layers of the cortex and results in either positive or negative deflections in the cortical surface potentials [101]. Determining the cell type being recorded from extracellular recordings is difficult to do with certainty without additional methods. Optogenetics enables a specific cell type to be stimulated, so either optogenetic stimulation with simultaneous extracellular recordings could be used to assay cell type or even drive activity in a given cell type. For example, optogenetic experiments have shown (as described in second 1.3) an anti-phase relationship of pyramidal and inhibitory interneuron spiking [49,50]. Similar optogenetic and spike-field phase coupling experiments could be directed towards understanding micro-ECoG.

1.6 Conclusion

In conclusion, the micro-ECoG signal is a spatially weighted superposition of signal sources within the brain. The signal characteristics of ECoG, including gamma, event related desynchronization, phase-amplitude coupling, and broadband shifts, provide a basis for understanding micro-ECoG signals, especially when these characteristics are tied to their neurophysiological correlates and biophysical theory. Prior research on the relationship between spikes and LFPs, especially those looking at phase coupling, suggests the hypothesis that spikes are phase coupled to the micro-ECoG signal. Further experimentation could help link micro-ECoG to intracortical signals.

Chapter 2: Optogenetic approaches to neurovascular coupling

2.1 Overview

Optogenetics was introduced less than ten years ago [5] and only in the past four years has it been applied to the study of neurovascular coupling. During that short period the array of methodological approaches combining optogenetics with neurovascular imaging expanded rapidly. Two-photon microscopy, laser special contrast imaging, intrinsic optical signal imaging, infrared phase contrast, and optical coherence tomography completes the current list of optical methods for monitoring hemodynamic changes in response to optogenetic modulation. Optogenetics has also been used in conjunction with functional magnetic resonance imaging (fMRI) to modulate the blood oxygen level dependent (BOLD) signal. Still, there is considerable space for additional methodological development. This chapter reviews methods utilizing optogenetics to investigate neurovascular coupling. It begins with a brief introduction to optogenetics before delving into the review. Neurovascular coupling is a vast topic, so a comprehensive review of neurovascular coupling is beyond the scope of this chapter. Instead, this chapter reviews the advantages and limitations of each method and identifies opportunities for additional development and research.

2.2 Introduction to optogenetics

Optogenetics is the use of light to modulate cells that have been genetically targeted. Most typically, channelrhodopsin-2 (ChR2) is inserted after a transcriptional promoter so that action potentials can be triggered in a specific type of neuron by applying pulses of blue light. ChR2 was isolated from green algae by Nagel et al. in 2003 [4] and later demonstrated in *C. elegans* [102]. Boyden et al. made the jump of expressing ChR2 in mammalian cells [5]. The variety of light sensitive ion channels, transmembrane pumps, and even G-protein coupled receptors have expanded through bioprospecting and genetic engineering. Opsins sensitive to various wavelengths of light that either excite or inhibit neurons over various timescales are now available [3]. These genes can be introduced via various vectors or transgenic animals can be used. Major strengths of optogenetics over other methods include its cell type-

specificity and the ease of delivering the stimulus (light). Delivering light to a sample is essential to optical microscopy, so combinations of optogenetics and optical techniques were a logical approach, but optical methods first require a view of the brain's blood vessels.

2.3 Cranial windowing techniques

Cranial windowing provides optical access to the brain's vessels for *in vivo* microscopy and optogenetic photostimulation. Many versions of the cranial window preparation exist [103–110], but they can be grouped into three versions: full craniotomy with glass window [111], thinned skull window [107,108], and reinforced thinned skull window [110]. The full craniotomy with glass window involves removing a piece of cranium and replacing it with a piece of sterile cover glass [111]. This technique provides the best image quality with only a thin piece of glass between the microscope and brain. The thinned skull window involves thinning an area of cranium down to less than 50 μm thick with a drill or microblade [108]. This technique is repeated as the bone grows back. For the reinforced thinned skull method, rather than periodically rethinning the bone, a drop of cyanoacrylate and a piece of cover glass is placed over the thinned skull [110]. The full craniotomy method is the most flexible experimentally, because it gives the greatest access to the brain. For instance, electrodes can be implanted under the cranial window [112]. However, the full craniotomy method is also the most invasive and it is now known that the disruption of the normal anatomy induces a confounding inflammatory reaction [113]. Drastically conflicting reports on the longevity of dendritic spines [108,109,111,114–116] were resolved by a direct comparison of the full craniotomy and thinned skull windowing methods [113]. The spines were more stable with the thinned skull window, suggesting that the physiology of cortex was better preserved. Therefore the thinned skull or reinforced thinned skull method are preferred when studying hemodynamics in the cortex.

2.4 Hemodynamic target signals

The hemodynamic response to neural activity involves changes in several biological variables; each provides a target signal for imaging approaches. Changes in neural activity lead to changes in blood

vessel structure, blood flow, and blood oxygenation. The physical structure of vessels changes primarily through dilation. Arterial vessels are surrounded by smooth muscle that can rapidly constrict or dilate. Veins lack smooth muscle and may be conceptualized as balloon. They distend when filled by increased flow and pressure. Structural changes in the vessels can be seen by injecting fluorescent dye intravenously or by imaging endogenous features of the vessels such as differences in refractive index. Changes in vessel diameter affect the fluidic resistance and therefore the blood flow. Both blood flow rate (volume/time) and average blood velocity (distance/time) increase as part of the hemodynamic response. The physiological purpose of vessel dilation and increased blood flow is to deliver more oxygen to metabolically active tissues, so blood oxygenation changes as well. Gases exchange in the capillary beds, so blood oxygen changes occur primarily in the veins. Deoxygenated blood differs from oxygenated blood in two ways from an imaging perspective: deoxygenated blood more readily absorbs red light, and deoxygenated blood is paramagnetic. The former is the key to pulse oximetry and intrinsic optical imaging, and the latter is key to fMRI [117]. Imaging methods have been developed to target each of these hemodynamic signals.

2.5 Optical imaging methods

Optical imaging methods that have been used in conjunction with optogenetics to study neurovascular coupling *in vivo* include 2-photon imaging, laser speckle contrast imaging (LSCI), intrinsic optical signal (IOS) imaging, and optical coherence tomography (OCT).

2.5.1 2-photon imaging

2-photon microscopy is widely applied to image blood vessels and blood flow *in vivo*. 2-photon microscopy is a non-linear imaging method in which a femto pulsed laser excites a fluorophore with two long wavelength photons and a shorter wavelength photon is emitted. The long wavelength of the excitation light helps avoid absorption by the tissue, enabling imaging several hundred micrometers into the tissue [118]. The focus of the laser rasters across the field of view using galvanometer mirrors to produce a fluorescence intensity image. Acquisition of a single image can take several seconds, so to

resolve the movement of particles (i.e. blood cells), small regions can be scanned [107], or the laser can follow a specified path to make line scans across multiple vessels at higher frame rates [110]. Injected dyes are most often imaged with 2-photon microscopy to study hemodynamics. Fluorophore conjugated dextran, a high molecular weight sugar, brightly labels all vessels when injected intravenously [119,120]. Blood cells appear as shadows against the bright background [119], especially when fluorophores that emit light of wavelengths that are readily absorbed by hemoglobin are chosen.

2-photon excitation could be used as a non-linear method to excite specific neurons within a 3 dimensional volume; several attempts have been made to do this. However, this approach is technically difficult, because the photonic efficiency of excitation is low and raster scanning is too slow to excite an entire cell. Initial approaches targeted cells in culture [121–124] and in brain slices [123,125,126]. However, the study of hemodynamics generally necessitates an intact brain. *In vivo* two-photon stimulation was finally achieved with the C1V1 opsin [124,9], a red-shifted engineered opsin with slow closing kinetics. Simultaneous 2-photon optogenetic modulation of neural activity and 2-photon vascular imaging remains an open opportunity. The major hurdle is to activate enough neurons simultaneously to cause a measurable hemodynamic change. Until then, single photon optogenetic simulation and 2-photon vascular imaging is the alternative. Single photon methods are a viable option as long as images of the most superficial vessels will suffice.

2.5.2 Laser speckle contrast imaging

LSCI begins by reflecting coherent light from a laser off of a sample. The reflected light interferes to produce a random pattern of speckles. Subtle phase changes in the speckles are generated when particles such as red blood cells move through the sample. The speckle patterns are then processed based on theoretical principles to create pseudocolored blood flow images. The major advantages of this approach include a wide field of view, no requirement of a fluorophore, and relatively low hardware costs. The major disadvantage is that as a single photon method, it images surface vessels only. LSCI

drew on prior single frame speckle imaging methods [127] and it is gaining popularity following its demonstration as a method to image cerebral blood flow in 2001 [128].

Two approaches have been used to integrate LSCI and optogenetics. The Thakor group demonstrated optogenetic modulation of LSCI [129–131] and built a head mounted miniaturized system for freely moving rats [132]. The Murphy group developed a standard upright microscope implementation of LSCI and optogenetics [133], used the system to study the necessity of glutamatergic signaling in neurovascular coupling [134], and most recently applied their system to study stroke [135].

2.5.3 Intrinsic optical signal imaging

The premise upon which IOS is based it that there is a relationship between changes in the optical properties of the brain, most typically the absorbance spectrum, and the function of the brain [136,137]. Among the many tissue properties and molecules that generate intrinsic signals, hemoglobin is most often used to study neurovascular coupling. Oxygenated and deoxygenated hemoglobin have different absorption spectrums, especially for red light. They absorb infrared light roughly equally, so ratiometric images of red to infrared reflectance provide information about the percentage of hemoglobin that is oxygenated.

Ayling et al. combined IOS and optogenetics [138]. They imaged the cortex with 635 nm light, a wavelength with a large absorbance difference for (de)oxygenated hemoglobin, as they applied both optogenetic and electrical stimuli to the brain. Subsequent studies by other groups added simultaneous multiunit activity recordings [139], LSCI [134], and visual stimulation [140] to IOS and optogenetics. Given the ease of applying red and infrared light with LEDs, and imaging the reflected light, IOS is particularly amenable to combinations with other imaging approaches.

2.5.4 OCT

Optical coherence tomography is an interferometry method for imaging 3 dimensional volumes of tissue with micrometer resolution. It was first demonstrated by the Fujimoto group in 1991 [141]. A coherent beam of light, usually from an infrared laser, is split by a mirror to send a portion of the light to

the sample and the remaining light to a reference arm [141,142]. This light recombines to produce an interference pattern and is sent to the detector. Reflections from the tissue occur at boundaries between tissues with different refractive indexes (e.g. at blood vessel walls and within blood). The tissue can be probed at various depths by changing the position of the reference arm rather than physically moving the relative position of the objective lens and the sample [141,142]. The beam is then rastered across the tissue to capture 3D data. The data are then processed to produce an image. The above describes time-domain OCT. Spectral domain OCT (SD-OCT) does away with mechanically sweeping the reference arm to resolve depth by applying a coherent light source with a very wide bandwidth and then using inverse Fourier transformations to measure the power spectral density to resolve depth [143,144]. This allows multiple depths to be measured simultaneously. Blood velocity can be measured with SD-OCT by analyzing the changes in phase information for the Doppler effect [145].

SD-OCT has major potential as an imaging modality to monitor vessel structure and blood flow in response to optogenetic modulation. Currently, the use of OCT in conjunction with optogenetics is limited to a study with transfected HEK cells in culture [146]. However, OCT has the potential to become a major method for studying neurovascular coupling.

2.6 fMRI

fMRI infers neural activity from changes in blood oxygenation and relative blood volumes [117,147–149]. Given the wide use of fMRI to study systems neuroscience, there is great interest to provide hard evidence of its neurophysiological basis. Lee et al. were the first in to combine optogenetics with fMRI [6]. Lee transfected rats with ChR2 and used an optical fiber to stimulate the cortex or thalamus while imaging the BOLD signal. She found positively correlated opotogenetic modulation of the BOLD signal both at the site of photostimulation and at the post synaptic region, so this approach can be used to study connectivity in a causal manner. Observing network activity, and not just signal at the site of stimulation, also helped build confidence that the putative signal was not due to a confounding mechanism such as heating. A parameter window of photostimulus irradiance (mW/mm^2) was identified

where photostimulation caused an optogenetic effect and not a major heating effect. A subsequent study conducted entirely in naïve rats showed that heating due to the photostimulus laser positively modulated the BOLD signal in a dose dependent manner, even at low photostimulus amplitude [150]. The results of these experiments complicated the interpretation of other optogenetic fMRI work. Experiments designed with sufficient statistical power that uses a naïve or wild type control group would be the best way to mitigate this problem. There is no reason to expect that thermal confounds are confined to fMRI, so all optical imaging studies need to consider their photostimulation parameters as well.

2.7 Photostimulation

New methods to deliver photostimulation light to the brain open the door for advanced spatial investigation of neurovascular coupling. The fiber coupled laser is the most common tool for delivering light for *in vivo* optogenetic studies [151]. It provides light to one location and therefore pairs well with subjects that have been transfected in a specific brain region. Transgenic animals with wide spread expression of optogenetic genes throughout brain require precise spatial control to avoid off target activation. Complex waveguides that penetrate into the cortex are a viable route for most optogenetic experiments [152], but they would cause too much damage to the vasculature to be used for neurovascular coupling studies. Controlling light spatially and temporally is achievable through an array of optical technologies beyond waveguides.

One of the first approaches to automating spatial light control was to steer a collimated light source with galvanometer mirrors [138]. Ayling et al. used this approach with a blue laser in a Thy1-ChR2 mouse to map motor cortex. They monitored EMG signals while systematically moving a collimated blue laser with a narrow cross section over the cortex [138]. This approach has the advantage of wasting almost none of the laser light, and its implementation is similar to setting up a laser scanning microscope. However, as a single photon method, it can only target surface structures, and it can only target one location at a time, though multiple targets can be stimulated in a rapid series.

Preventing or at least minimizing confounding hemodynamic effects due to heating is a major consideration as described in 3.6. Using the photostimulation light efficiently to cause an optogenetic effect is essential, because simply turning up the power of the light source will lead to heating and decreased efficiency as opsins near the source are illuminated beyond saturation levels. Therefore photostimulation approaches in which both the power (mW) and area (mm^2) illuminated can be controlled enable efficient photostimulation. Systems with a spatial light modulator (SLM) device can provide such control.

Optical systems can be built around SLM devices to generate 2D and 3D photostimulation patterns within the brain [9]. Example SLMs include the liquid crystal display (LCD) or digital micromirror device (DMD) technology found in video projectors. A video is essentially a spatiotemporal pattern of light. The pattern is created by directing light through, in the case of an LCD, or reflecting light off, in the case of a DMD, the SLM before focusing onto the sample with a series of optical components. SLM technology was first demonstrated in immobilized *C. elegans* [153] and zebrafish [154], and later it was demonstrated with freely moving optogenetic *C. elegans* worms [155]. The position of the worm was tracked with a camera and the projection pattern was updated in real time to maintain projection onto the same part of the organism as it moved. Systems have also been developed using multiple LCDs to target *C. elegans* with multiple wavelengths of light [156]. There has been progress toward SLM technology for *in vivo* mammalian optogenetics, DMD photostimulation of brain slices was demonstrated [157–159]. The major limitation of DMD photostimulation is that it can only produce 2D patterns of light.

Holographic photostimulation is possible with systems based around an LCD. The LCD is used to modulate the phase of a wavefront so that a desirable interference pattern is produced. Sufficient photodensity can be achieved to do photolysis [160] or glutamate uncaging [161] in brain slices. Holographic stimulation has been combined with optogenetics to stimulate the retina of awake behaving cats, demonstrating a type of bionic vision [162]. Phase-computed holographic stimulation is most

comparable to 2-photon stimulation for its ability to excite optogenetic targets in 3D, but they operate on different scales. 2-photon stimulation is perhaps best for stimulating single or parts of single neurons while holographic stimulation is somewhat less precise, but can target small volumes of cells, and may therefore be more ready for application to neurovascular coupling studies.

2.8 Future directions

Advances in approaches to image hemodynamic signals and deliver photostimulation have the potential to push optogenetic investigations of neurovascular coupling forward. OCT imaging is particularly well paired to the study of neurovascular coupling given its micrometer resolution of blood vessels in 3D and its ability to capture velocity data. There is potential to study the effect of optogenetic modulation with IOS at other wavelengths. Hydrolyzed nicotinamide adenine dinucleotide (NADH) is an enzyme involved in the electron transport chain, fundamental to metabolism, that has endogenous fluorescence [163,164]. Imaging NADH would provide additional information into the metabolic underpinnings of neurovascular coupling [165,166], but dissociating the NADH signal from other IOS signals could be difficult. SLM photostimulation technology could be used to study the dependence of the hemodynamic response on different volumes neural activation. Uniformly activating an area of cortex is difficult to do electrically or pharmacologically with high temporal resolution, but patterned photostimulation in optogenetic animals is feasible. Developing optogenetic and optical methods will enable a reverse engineering of the neurovascular system.

Chapter 3: The relationship between micro-ECoG and intracortical recordings

Abstract

The distance, frequency, and phase relationships between micro-electrocorticography (micro-ECoG) and underlying cortical multi-unit and local field potential (LFP) activity were investigated by implanting rats with devices that recorded both types of activity. Rats were implanted epidurally with a custom micro-ECoG array and a silicon electrode (NeuroNexus) was inserted into the cortex through an opening in the micro-ECoG array. Bilateral implants with a micro-ECoG and silicon electrode in each hemisphere were done in a subset of subjects to address signal relationships across the two cerebral hemispheres. The spectral coherence was analyzed between pairs of electrode sites, and was found to decrease with distance and frequency. Spikes occurred during a preferred phase (usually the trough) and frequency (usually below 20 Hz) of the epidural micro-ECoG signal. The preferred frequency shifted lower with administration of dexmedetomidine, a sedative commonly used for cortical mapping, while the preferred phase was maintained. Some single units became more coherent to the micro-ECoG signal with stimulus drive in a distance dependent manner. This simultaneous comparison of micro-ECoG arrays and penetrating silicon arrays shows the spatial, spectral, and phase relationship of LFPs and spikes. The data from this platform could be used for source localization, predictive spike modeling, optimization of electrode geometry, or to design better brain-computer interface algorithms.

3.1 Introduction

Electrocorticography (ECoG) and microfabricated ECoG (micro-ECoG) have developed into popular tools for implementing brain-computer interfaces (BCIs) and studying cortical neurophysiology, and motivation has increased to relate potentials recorded from the cortical surface to neural activity within the cortex. Micro-ECoG signals lacks the obvious temporal definition that action potentials (spikes) afford intracortical extracellular recordings, but given the biophysical relationship between spikes and local field potentials (LFPs), micro-ECoG signals should contain information about neural activity [57].

Empirically investigating this relationship could help build a basis for understanding and applying micro-ECoG.

Demonstration of ECoG based BCIs in temporarily implanted human patients with epilepsy [14,167] spurred development of microfabricated arrays for long term interface applications. A range of micro-ECoG devices were developed by combining different fabrication processes and materials [27,32,168–170]. These arrays perform over an extended period [32,171] and are useful for BCI applications. Micro-ECoG strikes a balance between surgical invasiveness and long-term signal quality for BCI application [1]. Electrodes that penetrate into the cortex are successful in patients with motor neuron disease or deep brain stroke [172], but the invasiveness of the device limits wider adoption. The close proximity between intracortical electrode sites and neurons produces richer signals initially, but spike detection falls off precipitously over a course of months due to both biological and device-related failure mechanisms [2,173–175]. Given that intracortical electrodes only enjoy a temporary signal quality advantage, surface arrays may be a viable alternative, especially if micro-ECoG signals can be understood in context with intracortical activity.

The biophysics, anatomic organization, and circuitry of the cortex inform hypotheses on the relationship between intracortical activity and micro-ECoG signals. Residing on the surface of the brain, micro-ECoG recordings sites are closest to layer 1 dendrites. Dendritic currents dominate lower frequency (<300 Hz) electrophysiological signals due to the relatively large surface area of dendrites in comparison to axons, and the slower kinetics of dendritic depolarizations relative to action potentials. A majority of apical dendrites found in layer 1 are from layer 5 pyramidal neurons. This vertical structure, a nonhomogeneous distribution of dendrites, somas and axons, sets up ionic sources and sinks constituting current dipoles oriented perpendicular to the cortex. When micro-ECoG arrays measure potentials over this volume conductor, the amplitude of the signal depends on the dipole to electrode site distance. Given multiple spatially distributed signal sources, the micro-ECoG signal can be thought of as a spatially weighted superposition of potentials. Out of phase generators cancel, while synchronized activity creates

larger potentials. Therefore, we hypothesize a phasic relationship between micro-ECoG signals and spikes recorded under the array. This hypothesis is further supported by cortical slice patch clamp recordings that found that excitatory post synaptic potentials (EPSPs) and inhibitory post synaptic potentials (IPSPs) occur out of phase to generate LFPs [49]. Glutamatergic neurons drive the EPSPs and therefore spike preferentially at a certain phase of the LFPs. A second hypothesis, which is nonexclusive and complimentary to the first given the observation of phase-amplitude coupling, ties broadband ECoG power to the population spiking rate of the cortex [61,176,177]. The signal power to spiking rate hypothesis continues to be supported by both models and experiments [178,179]. In this paper we focus on spike-phase coupling.

Spikes and LFPs are known to be related based on observations of simultaneously recorded signals, and robust analysis methods exist for quantification. Spiking probability varies with the phase of low frequency LFPs [88,91,94], and applied fields can even bias spike timing under experimental conditions [180]. The strength of this can be quantified with the complex cross-coherence [181], which has a magnitude and phase angle across the frequency domain. The complex cross-coherence can vary with time and be dependent on behavioral state [92,182] and learning [183]. The magnitude of the complex cross-coherence, commonly called just the coherence, between two signals can be due to both passive (volume conductor) and active (excitable medium) tissue properties. The application of a stimulus [184] or pharmaceuticals [185] can be used to investigate the active component. Alternatively, the relationship between spikes and potentials in response to a rich stimulus can be approached from the perspective of information theory [186,187]. These prior studies of spike-phase coupling used intracortical electrodes.

The current study investigated spike-phase coupling between single units recorded within the cortex to micro-ECoG signals recorded epidurally in rats. We present data that was recorded from micro-ECoG and penetrating silicon arrays simultaneously.

3.2 Methods

3.2.1 Electrode technology

Custom micro-ECoG arrays were fabricated on polyimide using a biocompatible process [32]. Each array had 16 platinum sites 200 µm in diameter that were spaced 750 µm apart (figure 3.1 a). Electrode impedances at 1 kHz were approximately 30 kΩ. The arrays were fabricated with holes to allow a penetrating electrode to be inserted through the device. Single shank silicon electrodes (NeuroNexus, Ann Arbor, MI) were chosen with 16 iridium sites 23 µm in diameter spaced 100 µm apart to span layers of the rat cortex. Silicon electrodes with and without a flexible tether (chronic and acute-chronic NeuroNexus packages) were used with similar success. However, electrodes without a flexible tether could be inserted stereotaxically.

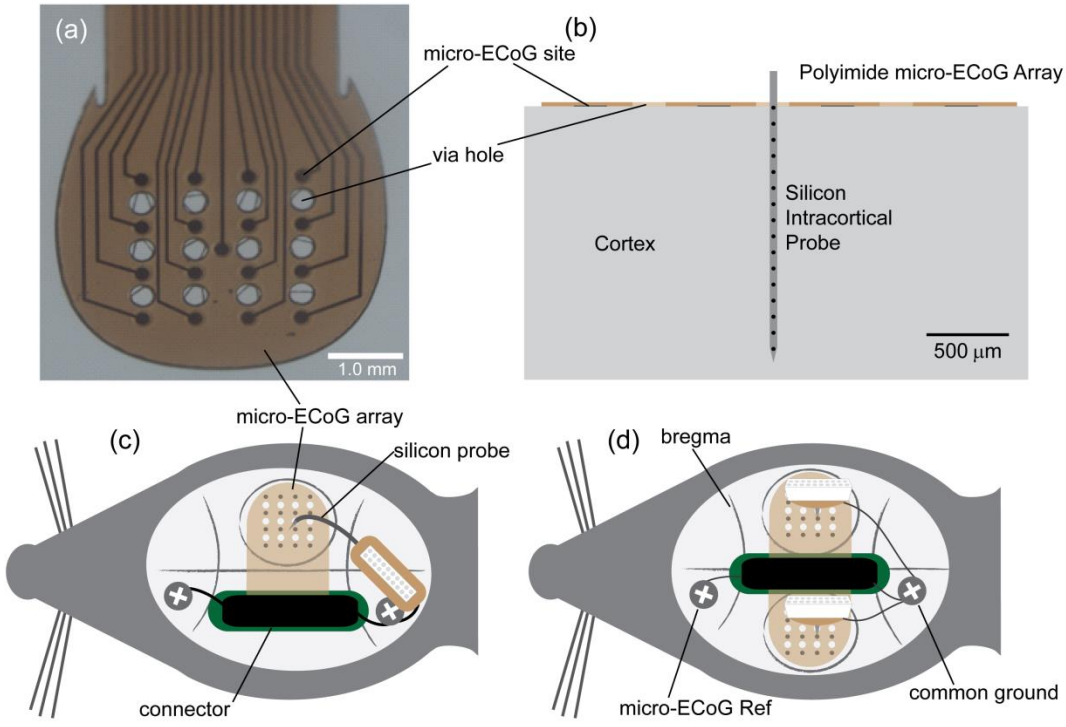

Figure 3.1. Electrode array implantation platform. Silicon intracortical electrodes were implanted through micro-ECoG arrays so that both signal types could be recorded simultaneously. (a) A custom micro-ECoG array was fabricated with via holes to allow a penetrating probe to be inserted into the cortex. (b) A cross-sectional schematic drawn to scale of a silicon intracortical electrode inserted into the cortex through a hole in the micro-ECoG. Rats were either implanted unilaterally (c) with a micro-ECoG array and an intracortical probe, or bilaterally (d) with a micro-ECoG array and intracortical probe over each hemisphere.

3.2.2 Surgical implantation

Seven 250-350g male Sprague Dawley rats were used in this study. All procedures were approved by the Institutional Animal Care and Use Committee at the University of Wisconsin Madison. Three subjects were implanted unilaterally with a micro-ECoG and a silicon array (figure 3.1c), and five subjects were implanted bilaterally with a micro-ECoG arrays and a silicon array in each hemisphere (figure 3.1d). Dexamethasone (1.0 mg/kg SC) and glycopyrolate (0.02 mg/kg SC) were given before the implantation procedure. Surgical anesthesia consisted of isoflurane at 1.5-2.5% after induction at 5% and buprenorphine (0.05 mg/kg SC) for analgesia. Unilateral or bilateral craniotomies were made using sterile surgical technique. A 16 site micro-ECoG was placed epidurally in each craniotomy. The dura within a via hole of the micro-ECoG array was pricked with a bent needle tip, and single-shank 16-site chronic or acute-chronic NeuroNexus probes were inserted by hand or stereotaxically, respectively. The uppermost penetrating electrode site was implanted to a depth even with the micro-ECoG (figure 3.1b). Three stainless steel screws (size 0-80) were implanted in the skull with a #56 drill bit for ground and reference connections and for mechanical support. The craniotomies (5mm x 5mm) were made with a high speed surgical drill using spherical burrs (Dremel #106 & #107) over the parietal region (bregma -5mm, 4mm lateral). UV-curing dental acrylic (Fusio by Pentron Clinical Technologies, Wallingford, CT) was used to anchor the implants to the skull, and a purse string suture (3-0 vicryl) was used to close the surgical wound. Oxygen saturation, heart rate, and temperature were recorded throughout the procedure. Animals were monitored post-surgically and administered a second dose of buprenorphine 12 hours later. Ampicillin (100 mg/kg SC) was administered twice a day for 1 week following the procedure, and triple antibiotic ointment was applied to the skin edges until healed.

3.2.3 Data acquisition, stimulus, sedation

Signals were sampled simultaneously at 3 or 24 kHz from the micro-ECoG and intracortical arrays using a Tucker-Davis Technologies (Alachua, FL) RZ-2 amplifier system. Recorded data was not digitally filtered initially to avoid phase delays. Recordings were made with and without sedation

(dexmedetomidine, 50-100 µg/kg SC). Spontaneous as well as visual evoked activity was record. The visual stimulus was a 25 ms flash of white light every 4-15 seconds in a dark room. The visual experiment was done with sedation (dexmedetomidine, 50-100 µg/kg SC).

3.2.4 Data analysis

3.2.4.1 Spike sorting

Spikes were extracted in a four step process. First, a band-pass filter from 500 Hz to 3 kHz was applied. Second, the common average reference was applied [188]. Next, the thresholds were automatically set at $5.5 * \text{median}\left(\frac{|x|}{0.6745}\right)$ in accordance with Quiroga 2004, where $|x|$ is the absolute value of the filtered signal [189]. Last, at each threshold crossing, the spike waveform was extracted from a signal band-pass filtered from 300 Hz to 5 kHz to retain more low frequency spike shape information. The spikes were presorted for outliers using principle component analysis (PCA) and KlustaKwik [190]. The spikes were then upsampled using cubic spline interpolation, aligned at the peak, and then downsampled before sorting using PCA and KlustaKwik in a semi-supervised fashion.

3.2.4.2 Spike-phase assignment

The Hilbert transform was used to associate spike times with a phase of the micro-ECoG signal. The micro-ECoG signal was tightly bandpass filtered with an 8^{th} order Chebyshev type 1 filter with a bandwidth of 1 Hz. The Hilbert transform yielded an analytic signal, and the instantaneous phase was found.

3.2.4.3 Spectral coherence

The complex cross-coherence between spikes and LFPs or between LFPs and LFPs was found using the Chronux 2.0 library for Matlab [181]. A time-bandwidth product of 3, 5 tapers, and a window of 1.0 seconds were used for most figures. The evoked cohereogram in figure 3.4 was calculated with a 0.125 second window and a step of 0.0125 seconds to better temporally resolve higher frequencies.

3.3 Results

Initial observations in a dexmedetomidine sedated rat indicated that spikes occurred during a preferred phase of low frequency micro-ECoG oscillations (figure 3.2a). Following this observation, we tested methods for quantifying spike-phase coupling, expanded the study to include more subjects, and applied sedation and stimulation as tools to interrogate spike-phase coupling.

3.3.1 Spikes couple to micro-ECoG phase

The relationship between spiking probability and the micro-ECoG signal was often apparent, even in unfiltered data. Figure 3.2(a) shows a micro-ECoG recording from a site near the silicon probe and an intracortical recording 1.0 mm into the cortex. The intracortical signal has both spikes and LFPs, and the spikes tend to occur in the troughs of the low frequency LFPs. The micro-ECoG recording shares much of the low frequency signal with the intracortical recording, and therefore the spikes tend to occur during the troughs of low frequency micro-ECoG oscillations as well.

We analyzed spike-phase coupling using two methods: phase-frequency-spiking probability histograms (figure 3.2b) and complex cross-coherence (figure 3.2c). These two methods were complimentary. The probability histograms provided a good visualization of spike-phase coupling, but due to the high dimensionality of the resulting figure, this method cannot be easily used to generate summary diagrams across multiple neurons and subjects. Complex cross-coherence, in comparison, yields readily summarized results with a magnitude and phase at each frequency.

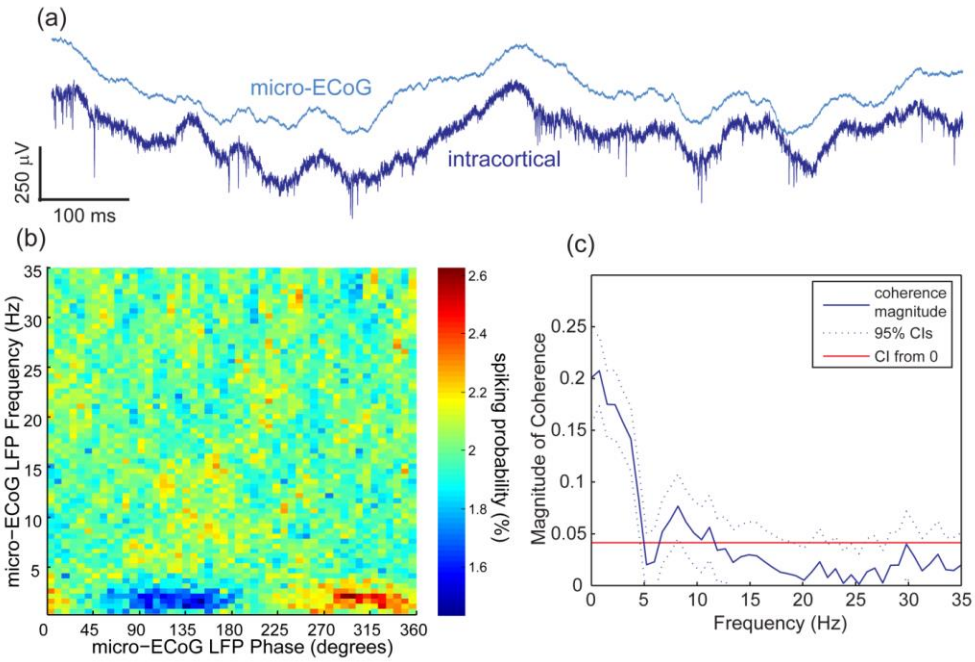

Figure 3.2. Comparison of spike-phase coupling analysis methods. (a) Example of unfiltered data from a micro-ECoG channel and an intracortical channel recorded simultaneously. Spikes were evident in the intracortical signal, and these spikes appeared to occur preferentially during the low frequency troughs of both the intracortical and micro-ECoG signal. In (b) and (c) the same data plotted in (a) was analyzed quantitatively. (b) The micro-ECoG signal was broken down into its frequency components using very high band-pass filters (bandwidth = 1 Hz). Each spike occurrence was assigned an instantaneous frequency, such that phase distribution could be plotted at each frequency. In this example, the single-unit preferred a micro-ECoG frequency of 2.5 Hz and a phase near 300 degrees. (c) The coherence magnitude is greatest around 2.5 Hz, similar to (b).

Extending complex cross-coherence analysis over all of the neurons recorded in multiple subjects, we found that spike to micro-ECoG coherence had a maximum across frequencies of less than 0.3 (figure 3.4a). For reference, the data in figure 3.2a had a maximum coherence of 0.21. The data were analyzed over 200 seconds with 1 second windows, so we used jackknife resampling to find neurons that were significant at α=0.05 level. Only these neurons were included for the phase and frequency summary histograms. The phase at maximum coherence (hereafter called the preferred phase) was uniformly distributed (figure 3.4b), and frequency at maximum coherence (hereafter called the preferred frequency) was usually less than 20 Hz with some exceptions (figure 3.4c). To gain further insight into how spike-phase coupling depended on brain state, we investigated how complex cross-coherence changed as an effect of sedation and stimulation.

3.3.2 Sedation decreases frequency, focuses phase coupling

We investigated the effect of dexmedetomidine, an alpha-2 adrenergic receptor agonist, on spike-phase coupling between sorted units and micro-ECoG recordings. We collected data in awake and sedated subjects on the same day so that the same neurons could be identified in both conditions for pairwise analysis. Figure 3.3 shows a typical example of the phase-coupling relationship between a neuron and a micro-ECoG recording before and after sedation. In this case, the preferred frequency decreased, the strength of the coupling increased, and the preferred phase did not change. We extended this pairwise analysis over multiple subjects to see more general trends.

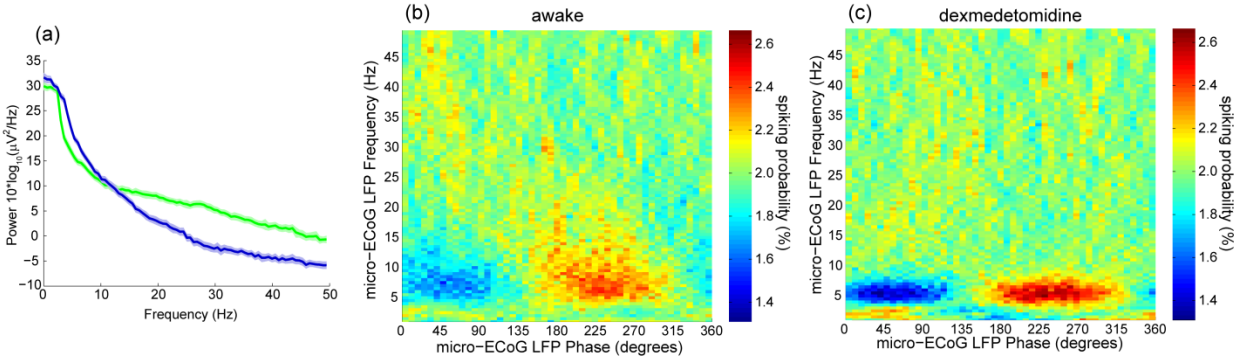

Figure 3.3. Dexmedetomidine effects on the micro-ECoG power spectrum and spike-phase coupling. (a) The power spectral density of the micro-ECoG recording decreased in power above 15 Hz and increased at slightly lower frequencies in response to sedation. In (b) and (c) the same sorted single-unit was compared to the same micro-ECoG channel in (a) under no treatment (b) or after administering dexmedetomidine (c). The spike-phase relationship shifted to lower frequencies and became stronger with dexmedetomidine.

Dexmedetomidine had pronounced effects on the micro-ECoG power spectrum, spiking patterns, and spike-phase coupling. The power spectral density of the micro-ECoG signal shifted towards lower frequencies under dexmedetomidine (figure 3.3c), and neurons recorded across multiple sites fired in temporal clusters under sedation. Analyzing across animals, sedation biased spike-phase coupling towards increased coherence (figure 3.4g). The preferred phase histogram became bimodal (figure 3.4e) and the preferred frequency shifted markedly to low frequencies (figure 3.4i). Similar but smaller amplitude trends were observed in contralateral hemisphere comparisons (figure 3.5). While these analyses used a single micro-ECoG channel near the silicon probe, more insight was gained by looking across channels and distance.

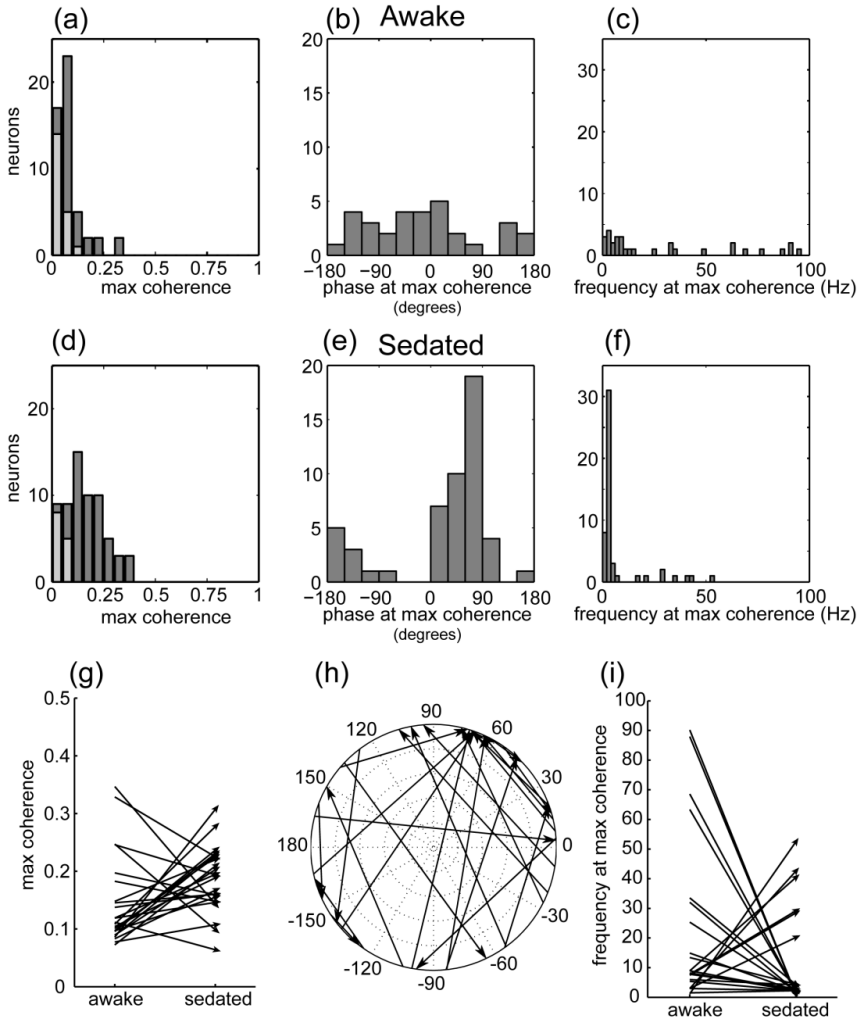

Figure 3.4. Ipsilateral changes in complex cross coherence following administration of dexmedetomidine. Data from 5 rats is summarized. The complex coherence was calculated between every sorted neuron and one micro-ECoG channel nearest the silicon probe. 200 seconds of data were recorded in each condition, segmented into one second windows and then averaged across segments. Awake (a-c) and dexmedetomidine sedated (d-f) recordings were analyzed. (a,d) The maximum coherence value across frequency for each neuron is plotted. Neurons with significant coherence as determined by jackknife resampling (α=0.05) are colored dark gray and were include in phase and frequency plots. (b,e) The phase difference of the complex coherence at the maximum coherence value across frequency is plotted. (c,f) The frequency of the maximum coherence is plotted. (g-i) Direct change graphs from awake to sedated for coherence (g), phase difference at maximum coherence (h), and frequency at maximum coherence (i). Only neurons with significant coherence under both conditions were plotted in (g-i). These data are from ipsilateral micro-ECoG and intracortical electrodes. Contralateral comparisons can be found in figure 3.5.

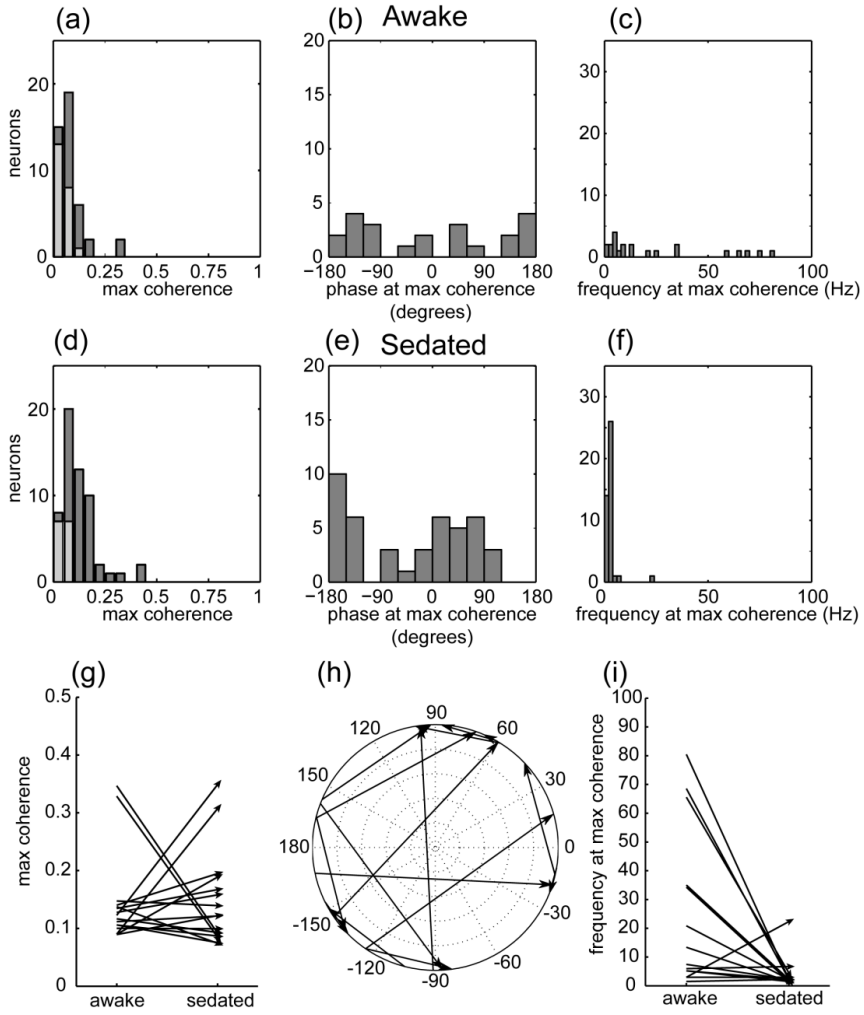

Figure 3.5. Contralateral changes in complex cross coherence for contralateral micro-ECoG and intracortical arrays following administration of dexmedetomidine. Data from 5 rats (those with contralateral arrays) is summarized. The complex coherence was calculated between every sorted neuron and one micro-ECoG channel nearest the silicon probe. 200 seconds of data were recorded in each condition, segmented into one second windows and then averaged across segments. Awake (a-c) and dexmedetomidine sedated (d-f) recordings were analyzed. (a,d) The maximum coherence value across frequency for each neuron is plotted. Neurons with significant coherence as determined by jackknife resampling (α=0.05) are colored dark gray and were included in phase and frequency plots. (b,e) The phase difference of the complex coherence at the maximum coherence value across frequency is plotted. (c,f) The frequency of the maximum coherence is plotted. (g-i) Direct change graphs from awake to sedated for coherence (g), phase difference at maximum coherence (h), and frequency at maximum coherence (i). Only neurons with significant coherence under both conditions were plotted in (g-i). These data are from contralateral micro-ECoG and intracortical electrodes. Ipsilateral comparisons can be found in figure 3.4.

3.3.3 Spatial dependence

We analyzed the spike-micro-ECoG coherence based on the distance between recording sites and compared this to the coherence between intracortical LFPs and micro-ECoG. Intuitively, one might expect that signals from sites that are close together have the greatest coherence in both cases, but our results were contrary to this expectation. Coherence between intracortical LFPS and micro-ECoG did have the stereotypical relationship with decreased coherence as distance and frequency increase (figure 3.6b), but the coherence between spikes and micro-ECoG recordings was greatest at a distance of 1.5 to 2.25 mm (figure 3.6a). Reanalyzing figure 5a with cortical depth along the silicon probe rather than the Euclidean distance between sites (figure 3.7) revealed that coherence was greatest with neurons 1.0 to 1.5 mms deep within the cortex (approximately cortical layers 4-6).

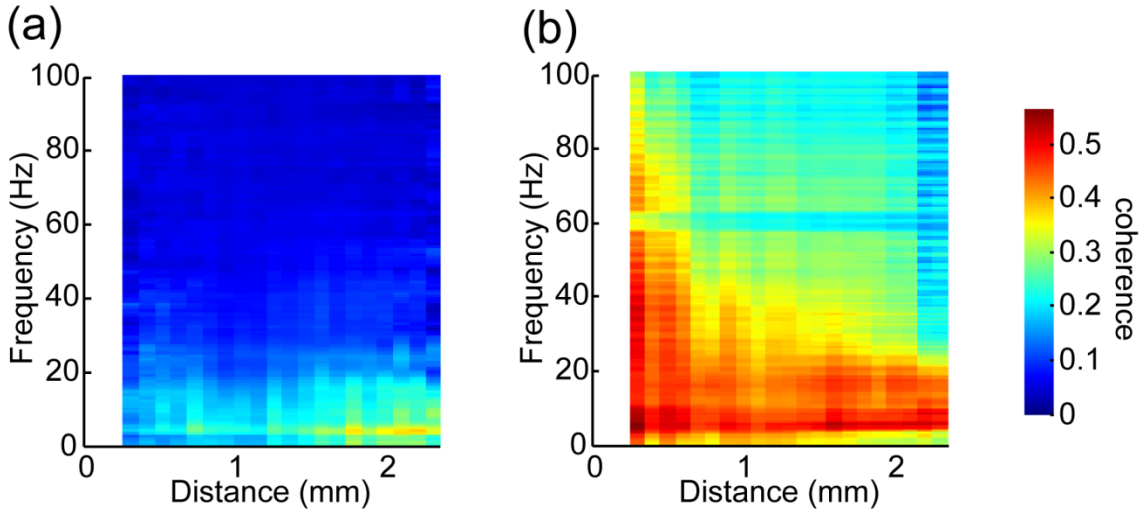

Figure 3.6. Coherence plotted as a function of distance between electrode sites for (a) the coherence between spikes and micro-ECoG recordings and (b) the coherence between intracortical LFPs and micro-ECoG recordings. The linear distance between electrodes was estimated based on electrode geometry. Coherence from electrode pairs with the same spatial separation was averaged. Representative data from one animal is plotted. Pooling data from awake and sedated data from the same rat over multiple recordings sessions was required to produce this figure. Coherence between LFPs and micro-ECoG recordings decreased as frequency and distance increased, but coherence between spikes and micro-ECoG recordings was greatest 1.5-2.25 mm. The data in (a) are replotted in figure 3.7 with cortical depth rather than site to site distance on the horizontal axis.

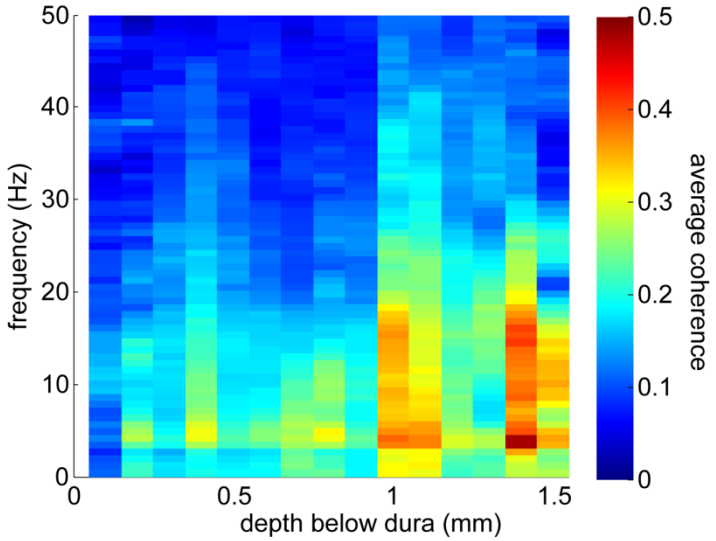

Figure 3.7. Coherence between spikes and micro-ECoG recordings plotted as a function of the depth below the cortex where the spikes were recorded. This is an alternative representation of the same data used to make figure 3.6a.

3.3.5 Stimulus driven coherence

The magnitude of the coherence between spikes and micro-ECoG recordings varies through time and can be driven by external stimuli. Visual stimulation transiently increased the coherence between micro-ECoG signals and a subset of spiking neurons. Figure 3.8 shows an example where the coherence was relatively low (<0.1) basally, but a flash of light evoked coherence between this neuron and the micro-ECoG signals in a spatially defined way.

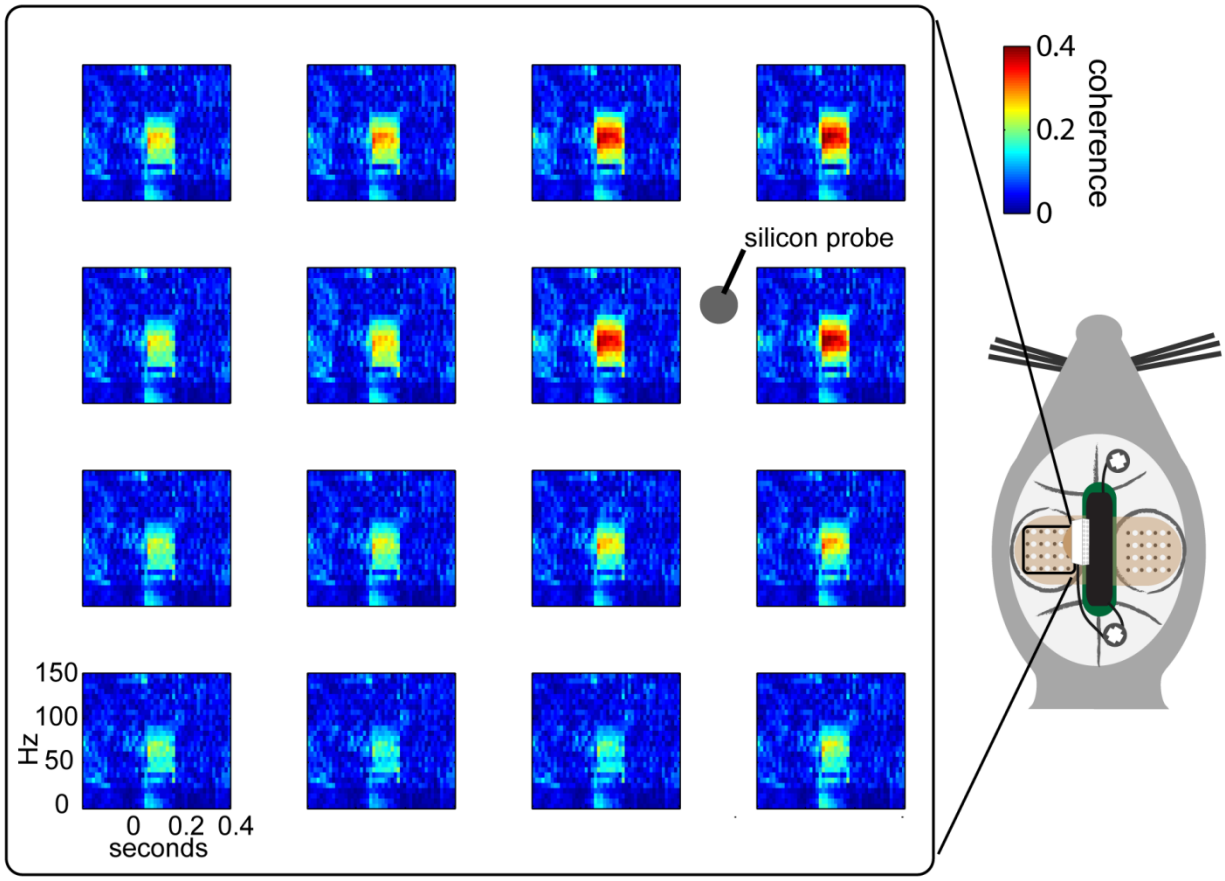

Figure 3.8. Spatially mapped evoked cohereograms in response to flashes of light (at t=0). These are representative data from a sorted neuron 1.0 mm below the surface of the cortex. Fifty trials were averaged. Without stimuli, this neuron had relatively low coherence (<0.1) with the micro-ECoG signals.

3.4 Discussion

Signals recorded from the surface of the brain are related to underlying intracortical neural activity, and spike-phase coupling is a theme of this relationship. Intracortical signals, both LFPs and spikes, are coherent with micro-ECoG recordings, but this coherence relationship differs spatially for LFPs and spikes (figure 3.6). More closely spaced electrode sites have greater LFP to micro-ECoG coherence, but the same was not true for spike to micro-ECoG coherence. The heterogeneously layered anatomical organization of the cortex and its circuitry resulted in spikes recorded from deeper cortical layers having the strongest phase coupling to micro-ECoG recordings. This finding is consistent with the conclusion that pyramidal neurons, whose cell bodies are found in layers 4-6 and apical dendrites are found in layer 1, are uniquely positioned anatomically, and as part of the cortical circuit such that their spikes have the

greatest phase coupling to micro-ECoG recordings. Observing this relationship under different pharmacological conditions gave further insight into how active properties of the cortex lead to spike-phase coupling.

Spike-phase coupling changed in response to administration of dexmedetomidine, while the underlying biophysics governing volume conduction remained unchanged, an experimental manipulation that disassociate properties of active circuits from passive volume conduction (figures 3.3-3.4). Pharmacological manipulation with dexmedetomidine created two brain states to consider. Altering the brain's state through pharmaceuticals is perhaps not as relevant to understanding the normal brain as other brain state modulators such as sleep and attention, but dexmedetomidine, which acts through a sleep-promoting pathway [79], is a commonly used drug during intracranial neurosurgery and electrocorticography [77,78]. Consistent with previous reports that dexmedetomidine shifts the ECoG power spectrum towards lower frequencies in humans [80], we observed decreased high frequency power and increased low frequency power (figure 3.3a). Correspondingly, the relationship between spikes and micro-ECoG recordings changed. Increased low frequency micro-ECoG power corresponded to stronger spike-phase coupling at lower frequencies (figure 3.4). Under sedation, the majority of coherent neurons were phase-coupled at 2-6 hz, and the phase histogram became bimodal rather than evenly distributed. This means that more neurons were firing in phase at a single frequency band, an increase in loosely defined spike synchrony. We conclude that shifts towards low-frequency power of micro-ECoG recordings indicate increased synchrony and spike-phase coupling.

Electrical and optogenetic stimulation could be used to further investigate this relationship with spatially localized, rather than systemically administered, modulation of the cortex. Anodic and cathodic stimulation of the cortex through bone screws biases gamma activity over a period of seconds [178]. Targeting specific layers of the cortex with electrical microstimulation while recording micro-ECoG would be an interesting avenue, and optogenetics could add cell type-specificity to the experiment. Previously, we used optogenetics to test the spatial localization of micro-ECoG [191]. Adding

optogenetic stimulation of the cortex to the current study would have enabled the phase-coupling relationship to be resolved with cell type-specificity, improving our understanding of what generates the micro-ECoG signal. Basic research into the basis of micro-ECoG improves our ability to apply the technology to areas such as BCIs.

Micro-ECoG and intracortical arrays could be utilized together to create more robust chronic BCIs. BCIs based solely on spikes have sudden drops in performance when a neuron is lost. Micro-ECoG signals could be used to augment these recordings so that the BCI fails more gracefully, an important feature of a robust system that is being relied upon by its user. In this scenario, the relationship between spikes and micro-ECoG signals could be leveraged in the case that spiking signals are lost. An approximation of the neuron's spiking probability could be generated from the micro-ECoG signals and temporarily substituted until further BCI training could occur. Further, the frequency of maximum coherence between spikes and micro-ECoG was indicative of the brain's state and could be used to decode attention and sleep.

The future of micro-ECoG depends both on improving array technology and improving our understanding of the signals. Producing arrays with improved materials, greater site density, active amplification, and multiplexing [33] are continuous technological goals. Similarly, investigating the neurophysiological basis of the micro-ECoG is an ongoing pursuit.

Chapter 4: Optogenetic micro-electrocorticography for modulating and localizing cerebral cortex activity

Abstract

Objective. Spatial localization of neural activity from within the brain with electrocorticography (ECoG) and electroencephalography (EEG) remains a challenge in clinical and research settings, and while microfabricated ECoG (micro-ECoG) array technology continues to improve, complimentary methods to simultaneously modulate cortical activity while recording are needed. *Approach.* We developed a neural interface utilizing optogenetics, cranial windowing, and micro-ECoG arrays fabricated on a transparent polymer. This approach enabled us to directly modulate neural activity at known locations around micro-ECoG arrays in mice expressing Channelrhodopsin-2 (ChR2). We applied photostimuli varying in time, space and frequency to the cortical surface, and we targeted multiple depths within the cortex using an optical fiber while recording micro-ECoG signals. *Main Results.* Negative potentials of up to 1.5 mV were evoked by photostimuli applied to the entire cortical window, while focally applied photostimuli evoked spatially localized micro-ECoG potentials. Two simultaneously applied focal stimuli could be separated, depending on the distance between them. Photostimuli applied within the cortex with an optical fiber evoked more complex micro-ECoG potentials with multiple positive and negative peaks whose relative amplitudes depended on the depth of the fiber. *Significance.* Optogenetic ECoG has potential applications in the study of epilepsy, cortical dynamics, and neuroprostheses.

4.1 Introduction

Recording potentials from the surface of the brain, electrocorticography (ECoG), was originally developed to functionally map the cerebral cortex in patients with epilepsy [13]. More recently, brain-computer interfaces (BCIs) have been implemented based on ECoG [14,16]. Both epilepsy and BCI applications of ECoG could benefit from improved interface technology. High density microfabricated ECoG (micro-ECoG) arrays have been developed to record from large cortical areas at high resolution [33,169], and chronically implanted micro-ECoG arrays show promise for BCI applications [192]. While recording devices continue to improve, complementary approaches to simultaneously stimulate cortical activity would be useful for many applications. Such bidirectional cortical interfaces could be used to

study the dynamics of epilepsy, to validate inverse models that relate potentials measured on the surface of the cortex to localized neural activity at known locations, or to create BCIs with sensory feedback.

Electrical microstimulation and transcranial magnetic stimulation (TMS) are potential methods that could be combined with ECoG to implement a bidirectional interface. Microstimulation is used to excite small volumes of neurons [193], but simultaneous recording can be difficult due to potential electrical artifacts. Custom electrical hardware can significantly reduce artifact size [194], but artifacts cannot be completely avoided. Artifacts are also created by TMS, and while TMS has the benefit of being non-invasive, it has relatively low spatial resolution and limited ability to stimulate at multiple locations simultaneously.

Optogenetics is potentially an ideal technology to be combined with micro-ECoG electrode arrays to create a bidirectional neural interface. Optogenetics is an emergent field that offers the ability to excite or inhibit a specific neuron type with light sensitive ion channels or pumps [195–197]. Since optogenetics leverages the inherent properties of modern optical systems, it can be used on a similar spatial resolution as electrode arrays and can modulate multiple locations simultaneously. Researchers have previously combined optogenetic modulation with neural electrode recording technologies, primarily through the integration of optical fibers with silicon or wire intracortical electrodes [50,198–201]. Optically induced recording artifacts are a potential problem [202], and even though the high work function of the noble metals can help prevent the photoelectric effect, the Becquerel effect is still a concern [203]. Carefully designing the device to minimize the amount of light incident on the exposed sites can help prevent this problem. Optical waveguides or LED arrays [204] have been used as light delivery technologies and could be integrated into micro-ECoG electrodes, although high density optical connections are challenging to fabricate, and photostimulation would be limited to a finite set of locations.

Alternatively, cranial windowing, a surgical technique in which the skull is replaced with a small piece of cover glass [205,206], could also be adapted for optogenetic photostimulation and electrode implantation. Cranial windowing is most often used for optical imaging of the cortex [207], but it has

also been used to deliver optogenetic stimulation [138,198,207]. The depth of optical penetration through the cortex is limited [3,138,208], but focused or collimated light, in comparison to light diverging from an optical fiber, could be used to stimulate at greater depths. Cranial windowing could be further adapted for implantation of thin devices such as micro-ECoG arrays.

In this study, we developed an optogenetic micro-ECoG platform by implanting a custom thin-film electrode array under a cranial window in an optogenetic mouse model. Utilizing both LEDs and a fiber-coupled laser, we investigated the spatial, temporal, and spectral properties of the optogenetic micro-ECoG platform. We investigated the spatial separation of multiple optical sources, the evoked waveform of optogenetic stimulation at different depths within the cortex, and the response of the cortex to complex stimuli that vary in space, time, and frequency.

4.2 Methods

Our approach integrates electrode arrays microfabricated on a transparent polymer, windowing techniques adapted from *in vivo* imaging, and optogenetics to create a bidirectional chronic neural interface in mice. We fabricated custom micro-scale ECoG (micro-ECoG) electrode arrays on Parylene C (figure 4.1(b)) using a lift-off photolithography process (figure 4.1(a)). We implanted Parlyene C based arrays under a cranial window (figure 4.1(d)) in Thy1::Channelrhodopsin-2/H134R (ChR2) mice (5 mice chronic implantation, 5 mice acute, 2 wild type mice for control). Blood vessels were clearly visible through the array and cranial window up to 6 weeks after implantation (figure 4.1(e)). The platinum electrode sites and connecting traces occluded only 8.3% of the array's area, so the cortex could be readily modulated by photostimuli applied through the window and array.

4.2.1 Electrode fabrication

Custom micro-ECoG electrodes were fabricated by patterning platinum electrode sites on a transparent insulative substrate polymer, Parylene C. This transparent substrate was chosen so that photostimuli could be applied through the array and onto the cortex. In comparison, polyimide, another material commonly used in flexible electrode arrays, blocks blue light considerably (figure 4.2). Parylene

C is a biocompatible polymer for neural implants [170,209] that has been used as an insulator for microwire electrodes [210,211] and more recently as a substrate for flexible electrode arrays [212]. We fabricated our thin film micro-ECoG arrays with a biocompatible lift-off process including chemical vapor deposition, photolithography, and plasma etching (figure 4.1(a)). First, we deposited a layer of Parylene 15 µm thick on a silicon wafer. Second, we patterned metal layers (10 nm Cr, 200 nm Au, and 20 nm Pt) using photolithography and lift-off to form the electrical connection traces and electrode sites. Alternatively, a transparent metal layers such as indium tin oxide could be used for more transparent arrays [213]. The sites (150 µm in diameter) were arranged in a 4x4 grid with 500 µm site-to-site spacing. Next, we deposited a 10 µm layer of Parylene and etched with oxygen plasma (790, Unaxis) to expose the platinum electrode sites. We spun two 24 µm layers of AZ P4620 photoresist (AZ Electronic Materials) on as a mask during oxygen plasma etching. We chose oxygen plasma over more aggressive etching processes to preserve biocompatibility. Last, we released the arrays from the silicon wafer in a water bath.

Once the arrays were separated from the wafer, we bolstered the connector pad region with a polyimide backing to add the thickness required (200 µm) by the flexible printed circuit connector. We cut these backings out of 175 µm polyimide sheet (Pryalux LF, Dupont) with a cutting plotter (CE5000-40-CRP, Graphtec), and bonded them to the electrode pad area with the adhesive included on the polyimide sheet at 180º C and 235 kPa for 1 hour.

We inserted Parylene electrodes with polyimide connector backings into custom printed circuit boards (PCBs) to finish assembly (figure 4.1(c)). We designed the boards with Eagle (CadSoft) and had the boards fabricated and assembled (Imagineering Inc.) with surface mounted connectors. A flexible printed circuit connector (FH26, Hirose) accepts the electrodes, and the PCB routes the signals to a zero insertion force connector (DF30, Hirose) compatible with Tucker-Davis Technology amplifiers. We chose this mechanical connection scheme due to the difficulty of soldering platinum and to speed the assembly process. Once assembled, we measured the electrical impedance spectrum [214] (PGSTAT

128N, Metrohm) of the arrays in a dish of Saline to ensure typical values (e.g. 50 kOhms @ 1 kHz) at every site prior to implantation.

4.2.2 Cranial window implantation

We obtained Thy1::ChR2/H134R-YFP mice, one of the many optogenetic strains created by Guoping Feng [215,216], from the Jackson Laboratory (stock number 012350) and bred these hemizygous mice to wild type (WT) females to maintain a breeding colony. We chose mice with the H134R point mutation of ChR2 to reduce the intensity of light required to achieve photostimulation, but at the expense of slower channel kinetics [217–219].

In vivo experiments were approved by the Institutional Animal Care and Use Committee at the University of Wisconsin-Madison. The cranial windowing method has been used for many decades [205], and multiple investigators have adapted and improved the approach for specific applications [104,111,207,220–222]. Our approach adds implantation of a flexible array epidurally, underneath the cranial window (figure 4.1(d) and (e)) [112]. Dexamethasone (1 mg/kg SC) was administered on the day prior to surgery and again on the day of surgery to prevent cerebral edema. Buprenorphine (0.05 mg/kg SC) and ampicillin (100 mg/kg SC) were given 30 minutes before surgery, and glycopyrolate (0.02 mg/kg SC) was administered as the procedure began. Sterile implantation surgery was done in isoflurane-anesthetized mice (1.5-2.0% in oxygen).

The mouse was shaved, mounted in a mouse stereotaxic frame (Cunningham Mouse Adapter, Leica), and the surgical site was cleaned. An incision was made over the calvarium to expose the bregma and lambda sutures, and the connective tissue was removed with cotton swabs. UV acrylic (Fusio, Pentron) was applied in front of bregma, behind lamba, and around the periphery of exposed bone. Bone screws were not used due to the limited bone thickness, so the ground/ref wire was coiled and implanted over an area of thinned skull, similar to that used for thinned skull *in vivo* imaging, on the side contralateral to the cranial window. The bone was thin enough, and the area of the coiled wire was sufficient, to provide a low impedance ground connection. A drill (Micromotor Drill, Leica) was used with a burr (#105 & #106

Dremel) to create a craniotomy for the electrode array. The electrode was lowered onto the dura with a stereotaxic electrode positioner. With the electrode in place, a round piece of cover glass 3.0 mm in diameter (Warner Instruments) was placed over the craniotomy, and the cover glass was encircled with small pieces of gel foam. A small piece of drape was used to occlude the window while UV acrylic was applied around the edge of the glass and up to the connector. Once the electrode and connector were stable, the electrode positioner was removed. The ground/reference wire was then placed over the area of thinned bone on the other side of the sagittal suture with a piece of gel foam and covered with UV acrylic. The mouse was then recovered while maintaining supplemental oxygen and heat.

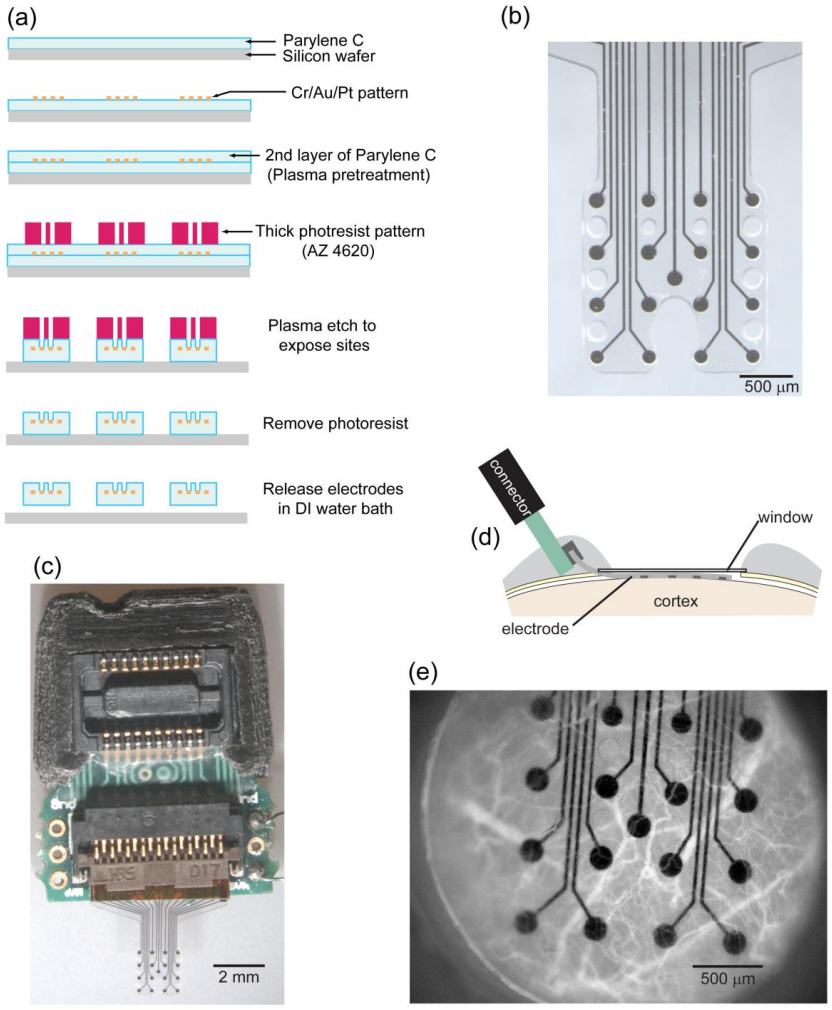

Figure 4.1. Micro-ECoG array fabricated on a transparent substrate and chronically implanted under a cranial window. (a) The photolithography process involved a lift-off method to pattern metal layers onto a Parylene C coated wafer, deposition of an additional layer of Parylene, and then exposure of the electrode sites with plasma etching. (b) A micro-ECoG electrode array with platinum electrode sites patterned on Parylene C. Electrode sites 150 µm in diameter are arranged in a 4x4 grid with 500 µm between sites. (c) The electrode array was assembled with a custom printed circuit board to route traces from the FPC connector to a zero insertion force connector. The array was implanted under a cranial window in mice as illustrated in panel (d). (e) Blood vessels, labeled with rhodamine-B dextran, were visible through the cranial window and electrode for several weeks following implantation.

4.2.3 Chronic neural interface testing with LEDs

Over subsequent weeks, we recorded neural signals from the micro-ECoG array while applying pulses of blue light through the cortical window under sedation. The mice were sedated with ketamine (75 mg/kg SC) and dexmedetomidine (25 µg/kg SC), and supplemented with oxygen and a heating pad. A Tucker-Davis Technologies system (RZ2 & PZ2) was used to sample the signals at 3 kHz and to generate

LED control signals. The voltage pulses were converted to current pulses (0-1000 mA, 0.5-12 ms) with an LED driver (BuckBlock, LED dynamics). Initial experiments (figures 4.3 and 4.6) were done by simply photostimulating the entire cortical window with an LED (465 nm, RGB MC-E, Cree) positioned 20 mm away producing 0 to 0.75 mW/mm^2 (0 to 5.3 mW total applied to the window). Irradiance was found by measuring optical power (PM100D, S130C, Thor Labs) 20 mm from the LED, and the result was divided by the sensor's area. In subsequent experiments (figures 4.7, 4.8 and 4.9), up to 4 LEDs were focused onto the cortical surface through a microscope (MZ16F, Leica) and individually controlled by separate drivers. The optical meter was used again to measure the total power, and the area was measured with the microscope. Each LED could be focused down to a spot 150 µm in diameter at 115x magnification. The stimulus location relative to the electrode sites was recorded manually or with a camera as multiple stimulus locations were tested. Multiple stimuli were applied at each location while recording the micro-ECoG signal. Atipamezole (0.5 mg/kg SC) was given to reverse dexmedetomidine at the end of the recording session. Rectangular light pulses were generally applied, except when testing the spatio-spectral response (figure 4.9) in which a frequency ramped sine wave (from 0.5-200 Hz increasing at 10 cycles/s^2) was used.

Control experiments were conducted to verify the optogenetic origin of the observed signals (figures 4.3(b) and 4.4). Since ChR2/H134R is primarily excited by blue light, we used an RGB LED (RGBW MC-E Star, Cree) to apply either blue or red light to verify that only blue light generates photostimulation. We also implanted and tested wild type mice (n=2) lacking the ChR2 gene.

4.2.4 LASER-coupled fiber experiments

A fiber-coupled LASER system [223] was used to deliver light to known depths below the electrode array and cortical surface (figure 4.10). These experiments were done terminally. The procedure was similar to the cranial window implantation described above through the placement of the electrode array on the dura. The anesthesia was switched from isoflurane, which blocks neural signals, to ketamine (75 mg/kg/hr SC) and dexmedetomidine (25 µg/kg/hr SC) at least 20 minutes before beginning data

acquisition. Buprenorphine was given as before (0.05 mg/kg SC). The craniotomy was left open and an optical fiber (200 µm in diameter, 0.22 NA, flat cleaved and polished, Thorlabs) was inserted into the cortex with a stereotaxic positioner which was equipped with a digital micrometer to precisely measure the depth of the fiber's tip. The fiber was advanced into the cortex 150 µm at a time, and micro-ECoG potentials were recorded in response to several stimuli at each depth. A 100 mW 473 nm LASER (Laserglow, Toronto, Canada) was used to produce photostimuli pulses 3 ms in duration and up to a power of 80 mW/mm^2 at the tip of the fiber. Irradiance was found by measuring optical power (PM100D, S130C, Thor Labs) and then dividing this value by the diameter of the fiber.

4.2.5 Polyimide and Parylene optical transmission

While designing electrode arrays for this study, we considered using Polyimide or Parylene C as the insulative substrate. Polyimide is an amber colored flexible insulator previously used in microelectrode arrays[224–226,168,27,29,169], while Parylene C is colorless polymer commonly used to coat implantable devices. We compared the transmission of blue light through 25 µm samples of each polymer into a 1% agar gel mixed in 0.9% phosphate buffered saline (PBS). The polyimide sample was prepared while fabricating arrays for another study[32]. The samples were laid along the side of a block of agar (7.5 x 40 x 40 mm). We aimed the fiber coupled LASER horizontally through the polymer samples and into the agar. The transmitted light was imaged with a digital color camera and stereoscope (DFC300 FX, MZ16 F, Leica). The images were spatially filtered (low-pass FIR, 0.01 pixels/µm corner frequency, 0.219 pixels/µm spatial sampling rate, order 50) to remove LASER speckles and isointensity contour lines were interpolated at levels relative to the maximum value when no polymer sample was present (supplementary figure 1).

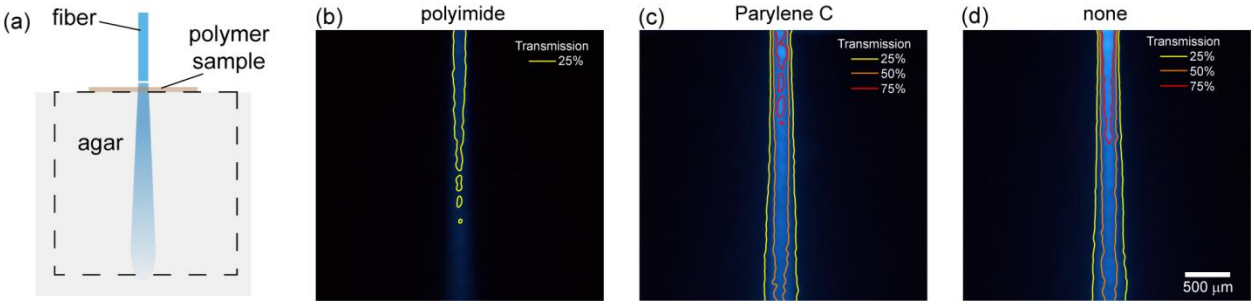

Figure 4.2. Comparison of light transmission through different electrode substrate polymers. (a) A LASER-coupled fiber (200 µm diameter, 0.22 NA, 473 nm) was aimed through 25 µm polymer samples into a 1 % agar gel, which served as an imaging phantom for the brain. The dotted square delineates the image region. Transmission through (b) polyimide was less than that through (c) Parylene C, which was more similar to (d) no sample at all. Relative isointensity lines are drawn for 25%, 50% and 75% of the maximum.

4.2.6 *In vivo* and brain slice imaging

An *in vivo* image of cortical and dural blood vessels under the electrode was taken 6 weeks after implantation (figure 4.1(e)). We used an epifluorescence stereomicroscope (Leica MZ16 F, 546/10 nm excitation, 590 nm long pass) following tail vein injection (0.1 ml, 10 mg/ml) of rhodamine B isothiocyanate dextran (70,000 MW, R9379, Sigma-Aldrich). Rhodamine-B was chosen for minimal spectral overlap with ChR2 excitation. A video of the stimulus location was captured (figure 4.8(a)) by attaching a video camera to the Leica MZ16 F. Frames were captured from the video for the figure.

A fixed brain slice was imaged to locate ChR2-YFP expression. A mouse was transcardially perfused with 15 ml of PBS followed by 15 ml of 4% paraformaldehyde in PBS to fix the brain, and 500 µm thick coronal slices were cut with a vibrating microtome (Campden Instruments). YFP expression of an entire slice 1.5 mm posterior to bregma (figure 4.10(b)) was imaged with epifluorescence microscopy (Leica MZ16 F, 480/40 nm excitation, 510 nm long-pass emission). To achieve better resolution, a 2-photon image was taken of the cortical layers (figure 4.10(c)) with 890 nm excitation (Mai Tai DeepSee, Spectra Physics) and a 10x 0.5 NA Nikon objective lens.

4.2.7 Micro-electrocorticography signal processing

Signals were initially recorded with no digital filtering, and later processed using Matlab. The only filter applied was a 500 Hz low-pass FIR (order 25, applied forwards & backwards to preserve phase) to remove aliasing unless otherwise specified. Multiple trials were averaged to generate event related potentials and remove uncorrelated activity. The duration versus irradiance plot (figure 4.3(d)) was made by recording a set of event related potentials for all combinations of photostimulus durations (0.5, 1.0, 2.0 & 4.0 ms) and irradiances (20, 40, 60, 80 & 100% of 0.75 mW/mm^2), measuring the peak depolarization for a single channel, and then linearly interpolating the data with Matlab's contour function. Linear interpolation was also used to localize and pseudocolor the peak potentials of the space-time varying photostimulus (figure 4.8). For the space-frequency figure (figure 4.9), Chronux 2.1 [181] was used to calculate a spectrogram of each channel with the multi-taper method (3 tapers, time-bandwidth product 5, 1 s moving window, 50 ms step size).

4.3 Results

4.3.1 Optogenetic micro-ECoG potentials

Stimulation of the cortical surface with a blue LED (465 nm, 3 ms, 5.3 mW across the window, 0.75 mW/mm^2) in Thy1-ChR2/H134R +/- mice produced large negative micro-ECoG potentials that were readily distinguishable from background activity (figure 4.3(a)). These negative potentials were consistent with ChR2 stimulation as they persisted for several milliseconds after the light pulse turned off (figure 4.3(b), left), and blue (but not red) light evoked a response that was absent in wild type mice (figures 4.3(b) and 4.4). ChR2 evoked potentials were highly reliable with similar amplitude potentials being produced on each trial, especially at large amplitudes (figure 4.3(a)). When we applied the photostimulus to the entire window, the averaged potentials were spatially uniform, and stimuli longer in duration evoked larger amplitude potentials than brief stimuli (figure 4.3(c)). The amplitude of the potentials depended on both the photostimulus duration and brightness (i.e. irradiance), so we systematically

explored this parameter space for single pulses of light (figure 4.3(d)). Given a desired potential amplitude, parameters for single pulses could be selected from this graph.

Light-induced artifacts were a potential issue for this hybrid approach. While the photoelectric effect was not a major concern as the energy of a blue photon of light is below the work function of the metals used in our arrays, the Becquerel effect (a.k.a. photochemical effect) could create light-induced artifact. The Becquerel effect scales linearly with the site impedance [203], so the relatively low impedance of our micro-ECoG sites (~50 kOhms @ 1 kHz) may help keep the artifact small. We controlled for optically induced artifacts in multiple ways. Wild type mice showed no response to blue photostimuli (figures 4.3(b) and 4.4), while ChR2 expressing mice responded to blue but not red light. We replicated the LED setup with an array in saline. The Becquerel effect was very small at less than 10 μV for a 10 ms pulse (0.75 mW/mm^2, 465 nm) and required hundreds of trials to be resolved (figure 4.5). This light-induced artifact was orders of magnitude smaller than the signals observed in ChR2 mice, and the artifact was tightly time locked to the photostimulus, whereas in ChR2 mice the potentials followed the photostimulus for tens of milliseconds (figure 4.3(b)). The high expression level of ChR2 in the chosen transgentic mice, the extended photocurents afforded by the H134R mutation, and the broad application of light to the entire window helps explain why fairly large optogenetic signals were observed for a fairly low level of irradiance (0.75 mW/mm^2).

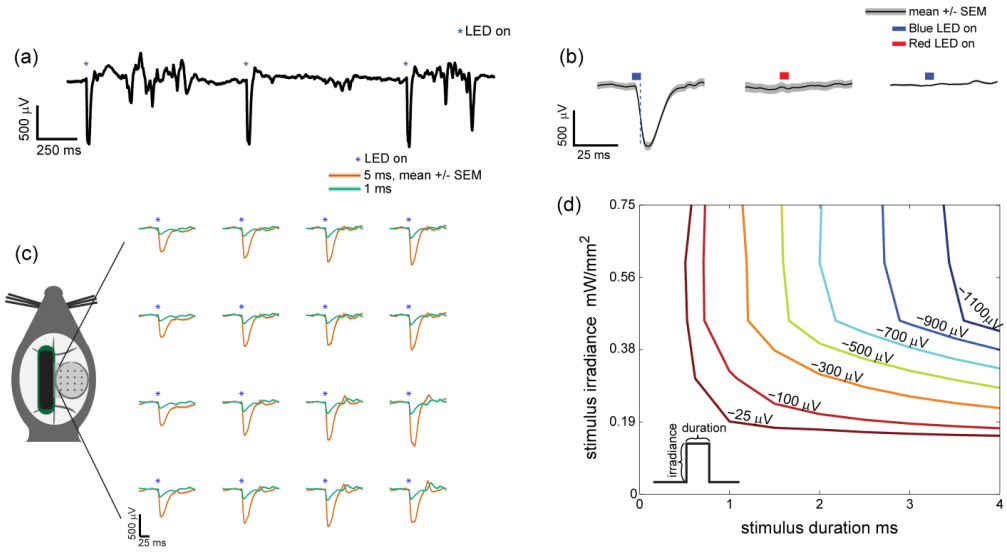

Figure 4.3. Optogenetically evoked micro-ECoG potentials. (a) An unfiltered micro-ECoG signal shows large negative potentials associated with every photostimulus * (465 nm, 3 ms, 0.75 mW/mm^2, 5.3 mW applied to entire window). (b) Wild type mice did not show any response to stimulation with blue light photostimulus - (465 nm, 0.75 mW/mm^2), while ChR2 positive mice were responsive to blue - (465 nm, 0.75 mW/mm^2) but not red - (625 nm, 0.81 mW/mm^2) photostimuli. A single channel is shown with 50 trials averaged for each condition. Control figures with all 16 channels can be found in supplementary figure 4.3. Trial-averaged evoked potentials are mapped according to channel location on the array (1 or 5 ms, 465 nm, 0.75 mW/mm^2, 5.3 mW total across the window). Longer stimuli evoked larger negative potentials. These potentials were spatially uniform with the entire window illuminated. 10 trials were averaged for each condition. (d) The amplitude of optogenetically evoked potential depended on the duration and irradiance (i.e. brightness) of the photostimulus. The stimulus duration and irradiance parameter space was systematically explored to generate a 2D interpolated contour plot.

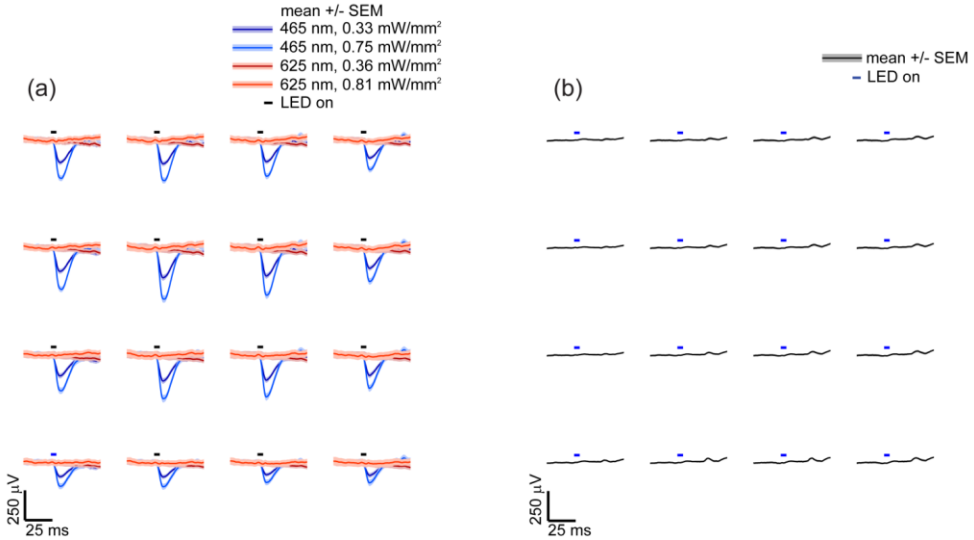

Figure 4.4. Controls for stimulus artifacts. (a) Pulses of blue light (465 nm, 3 ms) evoked negative potentials of several hundred microvolts, but red light (625 nm) did not. Brighter pulses of blue light (0.75 mW/mm2) evoked larger negative potentials compared to less intense (0.33 mW/mm2) stimuli. Red light (625 nm) evoked no response as expected. ChR2 is known not to respond at wavelengths longer than 550 nm. 50 trials were averaged for each condition. (b) Wild type mice lacking ChR2 showed no response to pulses of blue light (465 nm, 3 ms, 0.75 mW/mm2). 50 trials were averaged.

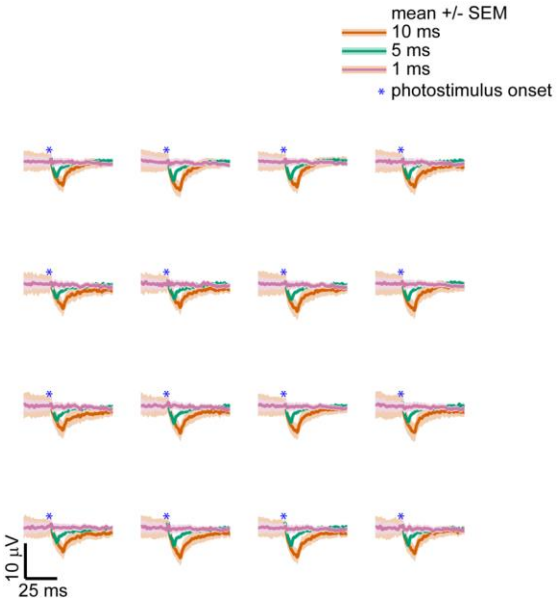

Figure 4.5. Electrode in saline test for the Becquerel effect. An electrode was positioned in normal saline to replicate figure 4.3(c) as closely as possible. A blue LED (465 nm, RGB MC-E, Cree) was positioned 20 mm. The LED was pulsed at maximum irradiance (0.75 mW/mm^2) for 1, 5 or 10 ms. The light-induced artifact was less than 10 microvolts, much smaller than the optogenetic signal observed *in vivo* (see figure 4.3). The small size of the artifact can be attributed to the low optical power used, the relatively low electrode impedance (~50 kΩ @ 1 kHz as compared 1 MΩ for most intracortical electrodes), and the orientation of the electrode relative to the light source. The light hit the Parylene C insulated backside of the electrode sites and traces. 465 nm photons have an energy less than the work function for the metals used in the array, so the photoelectric effect was minimal.

We investigated the ability to resolve two stimuli separated by a short interval by applying pairs of photostimuli. A second pulse 1-12 ms after the first caused an additional negative potential that could be resolved for pulse separations of 4 ms or greater (figure 4.6). At lower stimulus levels, the additional potential evoked by the second pulse was similar to that of the first pulse, but at higher stimulus levels, the additional potential evoked by the second pulse was less than the first (compare rows 1 and 3 of figure 4.6). This describes a saturation effect. Subsequently, we investigated spatial activation and localization of neural activity.

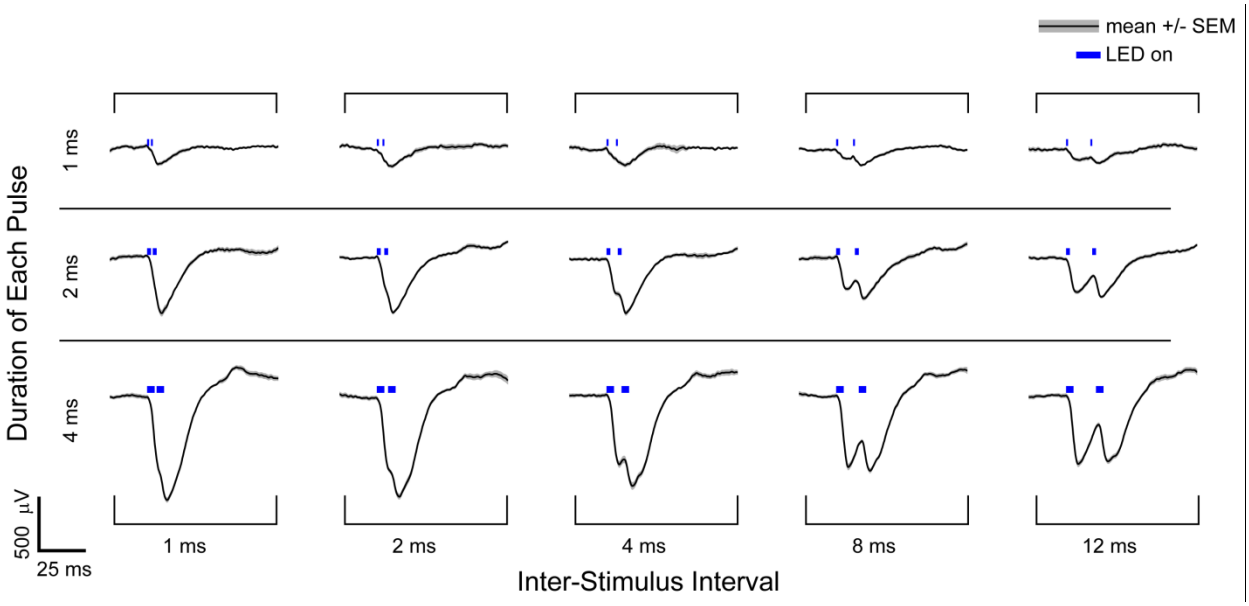

Figure 4.6. Optogenetically evoked micro-ECoG potentials in response to pairs of light pulses. Averaged potentials for a single channel are shown in response to pairs of photostimuli applied at 0.75 mW/mm^2. The duration of each pulse and the inter-stimulus interval was varied. Pairs of brief stimuli (1 ms) caused negative potentials that superimposed linearly, while longer photostimuli (4 ms) did not evoke a linear response as the second peak was not twice as large as the first. Photostimuli spaced by more than 2 ms could be readily distinguished, but photostimuli separated by less than 1 ms appeared as a single event based on the recorded signals. Between 13 and 28 trials were averaged for each condition.

4.3.2 Spatial localization

Focal photostimulation of a small cortical area (200 µm in diameter) was achieved by focusing an LED through a microscope objective (1 mW, 32 mW/mm^2, 465 nm, 20 nm FWHM). This focal stimulation evoked a spatial distribution of potentials with the largest amplitudes nearest the stimulus site (figure 4.7(a)). The spatial distribution of potentials changed with each new stimulus location. We tested the spatial resolution of the interface, the ability to distinguish signal originating at two locations separated by distance. Two LEDs were focused on the cortex and simultaneously applied. These two sources could be distinguished from the micro-ECoG potentials when the stimuli were greater than 1 mm apart (figure 4.7(c)), but the stimuli could not be distinguished when separated by smaller distances (figure 4.3(b)). Multiple sources were separable after averaging stimulus trials (figure 4.7(c)), but more sophisticated localization algorithms could also be applied [227,228].

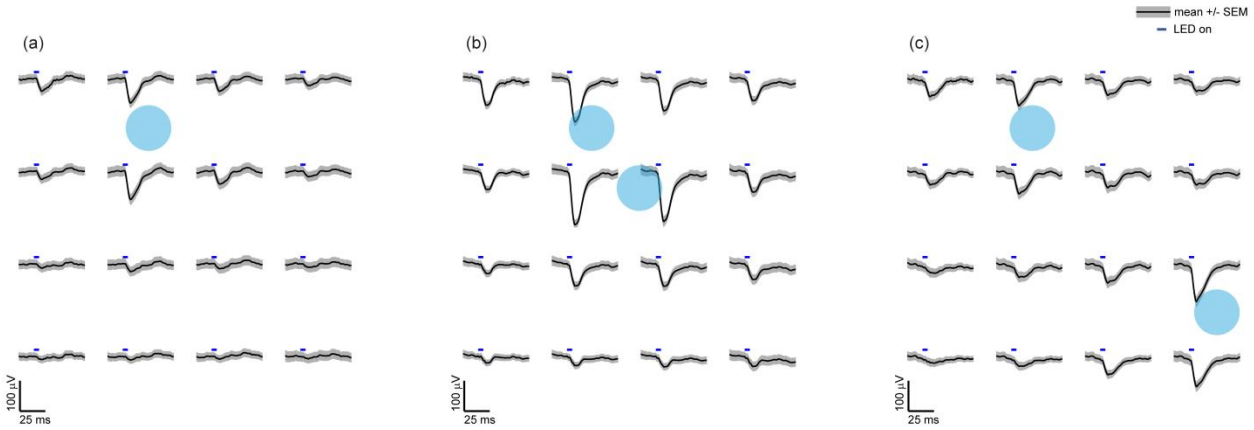

Figure 4.7. Spatially mapped micro-ECoG potentials in response to focally applied optogenetic stimuli. One or two focal photostimuli were applied repeatedly to the cortical surface using an objective lens. The photostimuli were 200 µm in diameter, for 5 ms in duration and 1 mW in power (32 mW/mm^2). (a) The amplitude of the evoked micro-ECoG potentials was greatest nearest the stimulus location. Surrounding electrode sites had similar but smaller amplitude waveforms with minimal phase delay suggesting electrostatic volume conduction. (b,c) Simultaneously applied focal photostimuli evoke spatially separable potentials at distances greater than twice the electrode spacing (c), but at closer electrode spacings the evoked potentials were less separable. 90 trials were averaged for each.

4.3.3 Space-time & frequency characterization

Complex photostimuli, varying both in time and space were applied to the cortex to further assess the cortical response to stimuli at multiple locations and with varied frequency content. To demonstrate stimuli varying in both time and space, we focused a 2x2 array of blue LEDs onto the cortex. The LEDs were sequentially illuminated every 125 ms in a clockwise pattern (figure 4.8(a)). Each stimulus location could be spatially localized with two-dimensional interpolation from the cycle-averaged micro-ECoG recordings (figure 4.8).

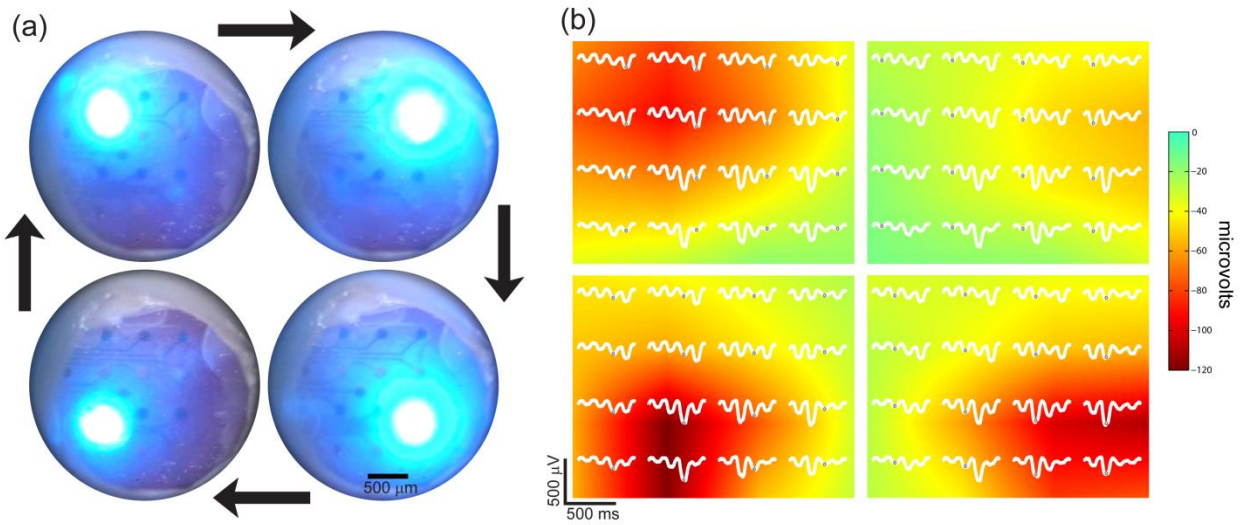

Figure 4.8. Spatiotemporal photostimulation and localization. (a) Photostimuli were applied at four locations in sequence. Four LEDs were focused on the cortex and illuminated in a clockwise sequence at 2 cycles per second. (b) The corresponding cycle averaged micro-ECoG potentials (100 cycles averaged) are plotted in white for each position. The peak potential for each stimulus location is marked o, and these values were pseudocolored using linear interpolation. Spatially localized potentials were observed for each stimulus location. Potentials were bandpass filtered from 5 to 500 Hz.

To test the space-frequency response of the cortex, we applied a frequency-ramped sine wave photostimulus to an area of cortex 400 µm in diameter. Electrode sites nearest the stimulus location recorded a larger signal that decreased as distance and frequency increased (figure 4.9). Stimulation frequencies below 50 Hz generated the largest response, which corresponds to the closing time constant τ_{off} for ChR2/H134R of 20 ms [218]. Deactivation of the ChR2 channel due to prolonged stimulation also accounts for roughly half of the ChR2 conduction decrease over time [218], but a change of many decibels can be seen after 50 Hz. After characterizing surface stimuli varying in time, frequency, and two spatial dimensions across the cortical surface, the third spatial dimension remained. We investigated neural activity below the cortical surface using an acute preparation and an optical fiber.

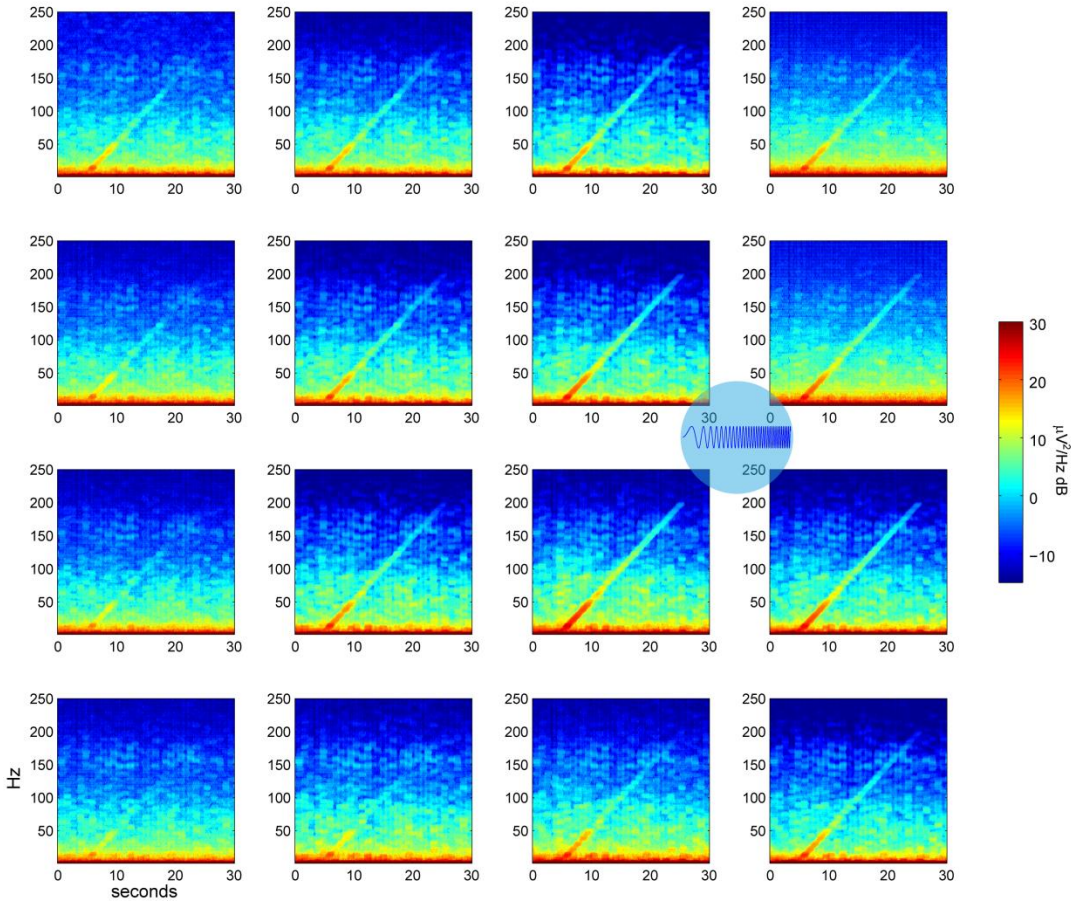

Figure 4.9. The spatio-spectral cortical response. A frequency-ramped photostimulus was applied to an area 500 μm in diameter between the electrode sites . Spectrograms of the signals at each micro-ECoG electrode site show that the cortical response decreases as distance and frequency increase. 5 trials were averaged.

4.3.4. Intracortical fiber stimulation

Photostimuli were applied at multiple depths below the cortical surface by advancing an optical fiber stereotaxically during an acute surgical procedure (figure 4.10(a)). The fiber was coupled to a 473 nm LASER [223]. Photostimulation with the optical fiber caused spatially defined potentials with the largest amplitudes observed nearest to the stimulus, similar to focal stimulation at the surface through the microscope. Multiple negative and positive potential peaks were observed at high stimulation intensities (2.5 mW, 78 mW/mm^2, 3 ms) (figure 4.10(d)), but only the first negative peak remained when the intensity was decreased (0.8 mW, 25.5 mW/mm^2) (figure 4.10(e)). These additional peaks at high stimulus intensities could be due to cortical circuitry with synaptic transmission to and inhibitory

feedback from interneurons, or these multiple peaks could be due to pyramidal neurons in deeper layers responding more slowly. Expression of ChR2/H134R-YFP was found in layers 2/3 and 5 at similar levels (figure 4.10(c)). As we inserted the fiber deeper, the initial negative potential peak decreased in amplitude, but the subsequent positive peaks increased with a maximum amplitude occurring when the fiber tip was positioned 300 μm deep within the cortex. As a control for light induced-artifacts, we found that the addition of isoflurane reduced the size of the potentials, and half an hour following the end of this terminal procedure, no light-induced artifacts were measureable. Further investigation with intracortical electrode arrays and modeling of this phenomenon will be necessary, but the current data could be readily applied to validating epileptic source localization algorithms.

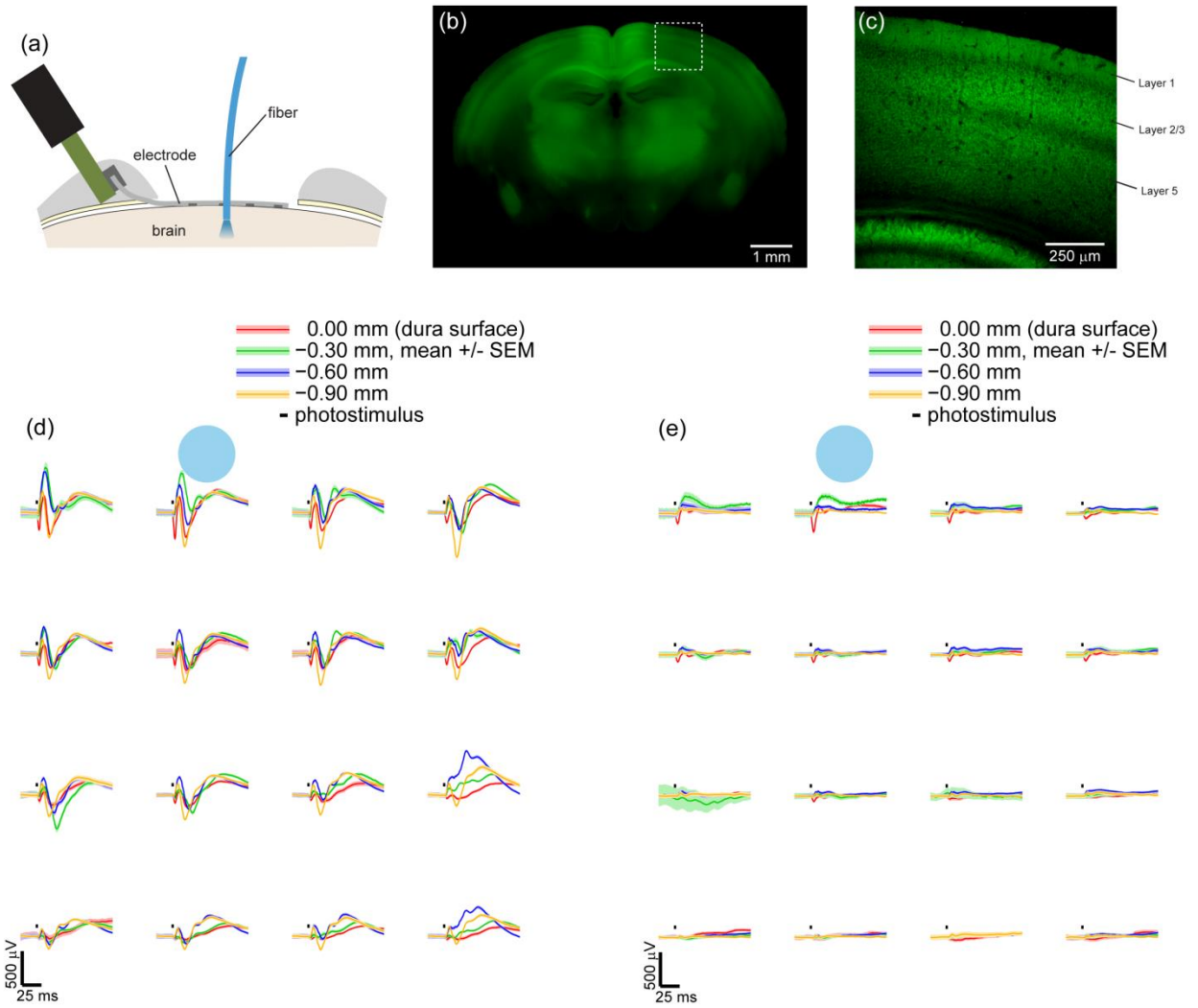

Figure 4.10. Optogenetically evoked micro-ECoG potentials in response to photostimuli applied intracortically with a fiber-coupled LASER or at depths below the cortical surface with a LASER coupled fiber. (a) A cross section diagram of a micro-ECoG electrode array on the dura and a fiber inserted into the cortex. Expression of ChR2/H134R-YFP under the Thy1 promoter in found in a subset of cortical layers. (b) Epifluorescence of an entire coronal slice 1.5 mm posterior to bregma shows expression in the cortex, hippocampus, and thalamus. Greater cortical expression is found medially, but the implanted region (0.5 to 3.5 mm lateral) has more uniform expression. (c) A two-photon image of the outlined region in (b) shows expression in cortical layers 2/3 and 5. Layer 1 also has expression but no cell bodies, suggesting expression in apical dendrites. (d,e) Averaged potentials recorded from the micro-ECoG array in response to photostimuli - (3 ms, 473 nm) applied next to the array at multiple depths within the cortex. Photostimulus power was 2.5 mW (78 mW/mm^2) in (d) and 0.8 mW (25.5 mW/mm^2) in (e). Stronger photostimuli (d) caused potentials with multiple negative and positive peaks, while weaker photostimuli (e) evoked only an initial negative peak. These subsequent peaks followed several milliseconds after the photostimulus ceased. Similar to figure 4.7, the amplitude of the micro-ECoG potentials (d,e) were spatially related to the stimulus location. 50 trials were averaged for each condition in (d) and (e).

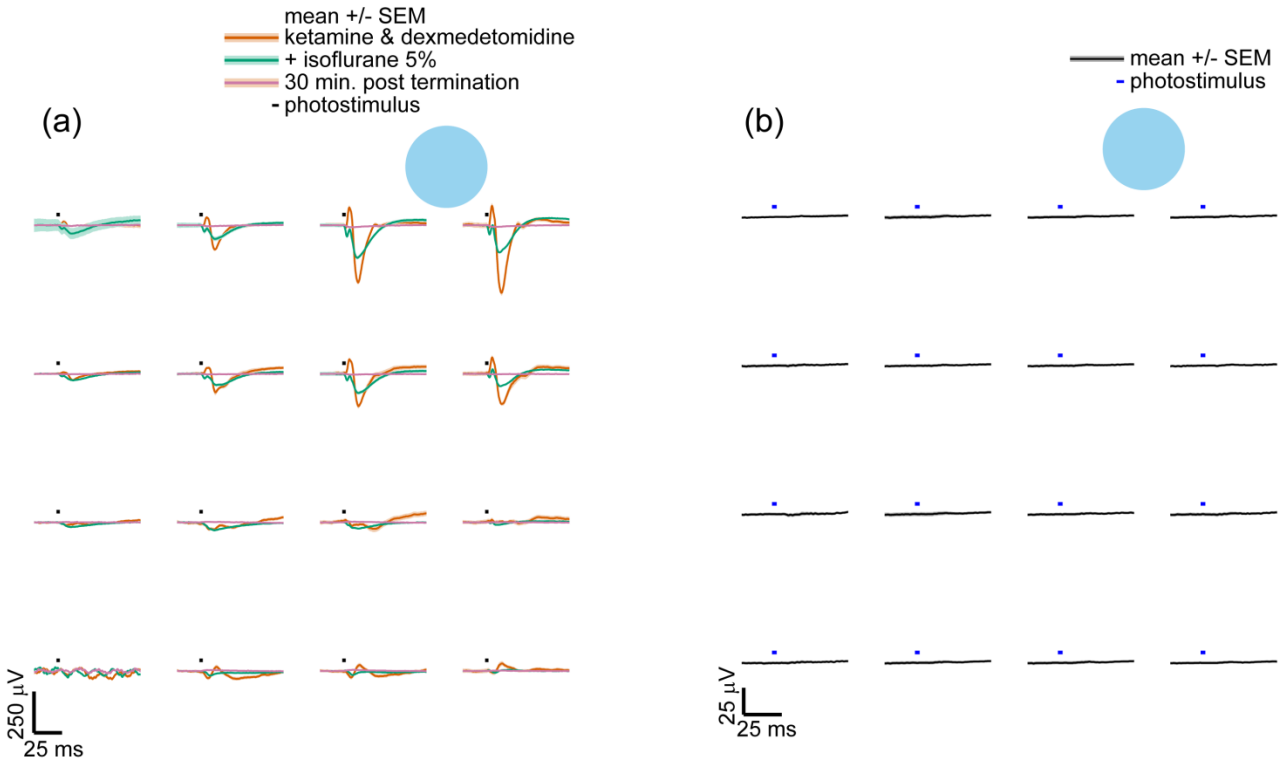

Figure 4.11. Control experiments for the Becquerel effect with fiber-coupled laser photostimulation and micro-ECoG recordings. (a) The optogenetically evoked wave form depended on the anesthetics. Under ketamine and dexmedetomidine, as in figure 4.10, a large waveform is observed in response to photostimulation (3 ms, 78 mW/mm^2, 473 nm) 0.45 mm below the cortical surface in region indicated. The addition of 5% isoflurane changed the shape of the waveform and generally decreased the amplitude of the signal. 30 minutes following the end of this terminal procedure, the signal was flat, with no observable light-induced artifact. 50 trials were applied for each condition. (b) Replicating the experimental setup in a dish of saline, no light-induced artifact was observed with similar stimulus conditions (3 ms, 78 mW/mm^2, 473 nm, 0.45 mm below array). 372 trials were applied for (b). The lack of a measurable artifact with the LASER-coupled fiber setup can be attributed the orientation of the optical fiber relative to the array. The 0.22 NA fiber below the electrode and pointed downward into the tissue, away from the array, so only scattered light could possibly reach the array.

4.5 Discussion

Optogenetics is an effective approach for studying temporal and cell-type specific aspects of micro-ECoG. We found that exciting pyramidal neurons in the upper layers of the cortex causes negative micro-ECoG potentials (figures 4.3 and 4.7). This result was in accordance with Ayling et al. who also reported negative potentials when recording from the cortical surface in Thy1-ChR2 mice with silver wire electrodes [138]. Depolarization of neurons with ChR2 would be expected to create a negative potential as a net flux of cations enters the cells, leaving behind a net negative charge. Interestingly, this negative potential was less apparent when the photostimulus was deeper within the cortex (figure 4.10). This could

be investigated with computer simulations bridging neuron models, optogenetics, and electrostatics [229], but it is an open question whether a model with multiple cell types is required to account for the multiple potential peaks observed in figure 4.10(d). Using this system, optogenetics could be used to determine the contribution of specific cell types to the micro-ECoG signal. Studies in mice expressing ChR2 in interneurons have reported the generation of gamma rhythms [51,230], a frequency band of great importance to the ECoG community for BCI implementation [14] and cortical mapping [34].

Optogenetic micro-ECoG has potential applications for the study of epilepsy and other diseases affecting the electrophysiology of the cortex. Localizing aberrant neural activity from EEG or ECoG recordings remains a challenging inverse problem that requires a priori assumptions to be made about the nature of the solution (see [231] for a review), and direct verification of source localization algorithm performance is difficult, requiring the researcher to cause neural activity at a known time and location [227]. Towards testing a priori assumptions about the solution, it would be desirable to be able to drive multiple and spatially diffuse neural sources. This is difficult to do electrically, but relatively simpler to do optogenetically due to the inherent parallelism of light. Stimulating multiple neural sources simultaneously was readily achievable (figure 4.7) and more complex photostimulation could be induced with more advanced optical hardware (e.g. spatial light modulators). Additional directions relevant to epilepsy research include optogenetically testing the effect of antiepileptic drugs on cortical excitability, studying the effect of activating specific cell types during epileptic episodes, investigating the cortical dynamics of channelopathy mouse models, and developing closed-loop seizure detection and optogenetic stimulation protocols.

As a bidirectional neural interface, optogenetic micro-ECoG could be used in a wide set of applications and experimental approaches. Sensorimotor neuroprostheses are a potential application of our approach, but miniaturization and integration of the optical hardware would be required. Motor signals could be decoded from micro-ECoG, and information from sensors on the prosthesis could be fed back to the sensory cortex optogenetically. Feedback can also be applied more generally in closed-loop

paradigms in which the photostimuli depend on recorded signals in real-time. The amount of activity at a cortical region could be regulated, effectively pacing the cortex, or virtual connections could be formed by cross-connecting recording sites and photostimulation sites. These artificial connections could be used to interact with network connectivity models of the cortex or perhaps to bridge over an infarcted region. Cerebral vascular imaging and other *in vivo* approaches add more line of investigation.

Adding *in vivo* imaging and improving the optical hardware are the next steps for development of this platform. The cranial windowing technique we adapted for this study for the purpose of photostimulation also provided excellent views of cerebral vasculature for multiple weeks (figure 4.1(e)). Neurovascular coupling is an obvious route for investigation. The middle cerebral artery was apparent with epifluorescence imaging, but more advanced imaging techniques such as 2-photon or optical coherence tomography would help resolve deeper vessels. More advanced optical patterning hardware would also be helpful, since we were limited to a small number of LEDs. An optical system with a spatial light modulator would greatly improve spatial photostimulation capabilities. Further development and integration of optical systems will broaden the spectrum of applications for optogenetic micro-ECoG.

Chapter 5: Transcutaneous optogenetic mapping of sensory cortex

Abstract

Objective. Optogenetic sensory stimulation of the limbs can be achieved by applying light through the skin in transgenic animals. We investigated the cortical response to transcutaneous optogenetic stimulation. *Approach.* We implanted micro-electrocorticography (micro-ECoG) arrays in Thy1-Channelrhopsin-2 (ChR2), Thy1-Halorhodopsin (NpHR) and wild type (WT) mice. We compared the cortical response to peripheral optogenetic and electrical stimulation by recording sensory evoked potentials (SEPs). *Main Results.* Transcutaneous optogenetic stimulation evoked fast conducting fibers, resulting in a peak potential reaching the sensory cortex in 15 milliseconds. This cortical potential was contralateral to the stimulus and consistent with A_α or A_β fiber stimulation. Optogenetic and electrical stimulation produced the same cortical maps for the hindlimb and forelimb. Both stimulation modalities produced similar SEP waveforms, whether the stimulus was applied transcutaneously or directly to the nerve after dissection in a terminal preparation, but a stronger stimulus was required transcutaneously. We also found that NpHR can partially block electrical SEPS with yellow light applied through the skin. *Significance.* Transcutaneous optogenetic sensory mapping could be incorporated into sensory research paradigms to enable a cell type-specific approach to investigate sensory coding while remaining noninvasive in the periphery. Noninvasive sensory photostimulation approaches could someday be considered for sensory feedback.

5.1 Introduction

Optogenetic sensory stimulation through the skin holds promise as a temporally precise noninvasive method for modulating genetically targeted subpopulations of nerve fibers. Combining peripheral transcutaneous optogenetic stimulation with simultaneous recordings in the central nervous system could be used to study sensory coding or to implement sensory feedback for neuroprostheses should

optogenetics become translatable. The first study using transcutaneous light as a stimulus was performed in transgenic rats expressing channelrhodopsin-2 (ChR2) under the Thy1.2 promoter. Intriguingly, blue light applied through the skin from a high power LED was sufficient to cause limb movements, and histological evidence suggested that touch fibers where targeted [232]. The second transcutaneous sensory optogenetics study utilized Cre/lox mice to express ChR2 in pain fibers and these mice showed behavioral and immunohistological evidence of a nociceptive response to light stimulation [233]. Both of these initial studies demonstrated signal propagation as high as the dorsal root ganglion, but they did not address the cortical response to peripheral optogenetic stimulation.

Peripheral optogenetics began with investigations of the motor system. Pulses of blue light applied directly to the sciatic nerve with an LED nerve cuff in Thy1-ChR2 mice evoked compound motor unit action potentials as recorded by electromyography (EMG) [234]. This study provides evidence that optogenetic stimulation recruited small fibers that activate fatigue-resistant muscles prior to large fibers, while electrical stimulation generally causes reverse recruitment, leading to rapid fatigue. A modeling study by Arlow et al. reproduced these results and finds that orderly recruitment by ChR2 could be attributed to the shorter distance between nodes of Ranvier in small fibers, which results stimulation of more nodes in a given area of photostimulation. Based on this model they predict that only the optical nerve cuff, and not other light sources (e.g. laser-coupled optical fibers), would cause orderly recruitment, but this conclusion remains to be experimentally verified [235]. The recruitment order would also be important for sensory excitation.

The ability to not only excite, but to also block, sensations would increase the impact and variety of applications for transcutaneous peripheral optogenetics. Inhibition of motor fibers with halorhodopsin (NpHR), a chloride pump excited by yellow light, has been demonstrated in transgenic mice [236]. Sensory investigations utilizing NpHR peripherally would comprise the logical next step and signal important implications for the management of pain and spasticity. Given that the perception of texture

requires three or more sensory receptor types [237] , blocking a single genetically targeted subset of fibers could be used to deconstruct sensory coding.

When modulating the periphery for neuroprosthetic applications, targeting the correct set of nerve fibers is generally important to the application. Isolating motor, pain, and touch fibers requires special effort when electrical stimulation is used. Optogenetics affords the selectivity of genetics. By expressing the opsin under the control of a carefully chosen promoter, a subpopulation of fibers can be selected [238,239], and a multitude of devices can be used to deliver the light [9]. Despite the potential advantages of light-targeted opsins, many hurdles remain before optogenetics could become a translated technology [240,241]. Transcutaneous light delivery, as opposed to implanted waveguides, would reduce the invasiveness of peripheral optogenetic approaches and opens the door for rapid sensory mapping methods.

Micro-electrocorticography arrays are uniquely positioned for neurophysiology studies of the neural cortex and offer multiple advantages. First, they lie on the surface of the brain above or below the dura, and span cortical regions. Second, their design and implantation method can be tailored for *in vivo* imaging [112], electrical stimulation [242], optogenetics [191] and sensory cortex mapping [27,30,32]. In this study we mapped the sensory cortex of Thy1-ChR2 mice with optogenetic and electrical stimulation by fabricating and chronically implanting micro-ECoG electrode arrays to recorded sensory evoked potentials (SEPs). We compared transcutaneous stimulation to direct nerve stimulation for both photo and electrical stimulation. The ability of transcutaneously administered light to activate NpHR and block of SEPs was also tested.

5.2. Methods

5.2.1 Electrode implantation

Mouse-sized micro-ECoG arrays fabricated were fabricated as described previously [191]. Briefly, 16 platinum sites 150 um in diameter were patterned onto Parylene C with photolithography. The sites were arranged in a 4x4 grid with 500 um between sites.

All *in vivo* studies were approved by the University of Wisconsin School of Medicine and Public Health IACUC. Thy1-ChR2/H134R-YPF mice (n=3, Jackson Labs #12350), Thy1-eNpH-YFP mice (n=1, Jackson Labs #12332), and wild type mice (n=4) were implanted unilaterally with a micro-ECoG array. To check peripheral expression levels, paraformaldehyde fixed sciatic nerve specimens were imaged with two-photon microscopy (figure 5.1). The array was implanted epidurally over the left hemisphere (1.0 mm posterior and 1.5 mm lateral to bregma). The surgical methods are described in detail in reference [191]. Some mice were implanted with a cranial window for another optogenetic study of optogenetic micro-ECoG, while other mice were implanted without a cranial window. The mice were allowed to recover at least 3 days prior to sensory mapping sessions.

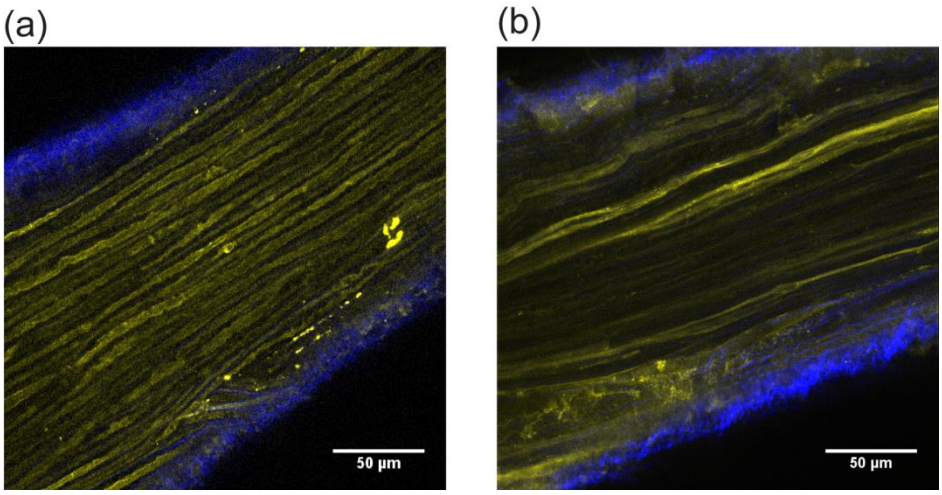

Figure 5.1. Two-photon microscopy of ChR2-YPF and NpHR-YFP in the periphery. A sciatic nerve from a ChR2-YPF mouse (a) and from an NpHR-YFP mouse (b) was imaged after removing and fixing the nerves in 4% paraformaldehyde. YFP was imaged with a 592/100 nm emission filter (pseudocolored yellow) and excited at 1028 nm. The epineurium was imaged using second harmonic generation of collagen by exciting at 890 nm and a 445/40 nm emission filter (pseudocolored blue). A 20x water 1.0 NA Zeiss lens was used. Expression in a subset of axons can be seen in each nerve.

5.2.2 Sensory evoked potentials

Sensory evoked potentials were recorded from the micro-ECoG array while the mice were sedated with ketamine (75 mg kg^{-1} SC) and dexmedetomidine (25 µg kg^{-1} SC). During the procedure, 100% oxygen was administered through a nose cone, and the mice were kept warm on a water-circulating blanket. For transcutaneous stimulation, the skin was shaved to improve light and electrical transmission.

The micro-ECoG signals were sampled at 3 kHz with a high-impedance headstage and electrophysiology system (RZ2, Tucker Davis Technologies). A blue LED (XPE blue, Cree, Durham, NC) was driven with a 1 Amp driver (BuckBoost, LEDdynamics, Randolph, VT) with a control signal from the electrophysiology system for the ChR2 study. Transcutaneous electrical stimuli were applied with electrode pads (2.5 cm diameter, cut to 1 cm diameter, Reliamed, Fort Worth, TX) positioned above and below the limb. A yellow laser (300 mW, 588 nm, LaserGlow, Toronto, Canada) was aimed at the dorsal surface of the forelimb, proximal to the electrode pads to excite NpHR. An isolated electrical stimulator was used to produce biphasic current pulses (2100, A-M Systems, Sequim, WA). Stimulus parameters were defined for each experiment (table 1).

Table 1. Stimulus parameters for each experiment.

Experiment	Figures	Stimulus Locations	Mouse Genotypes	Stimulus parameters
Transcutaneous electrical	5.2, 5.8	forelimb & hindlimb	ChR2+ & Wild Type	1 ms x 0-1.5 mA, biphasic, surface pad electrodes positioned on lateral and medial surface of limb, cathode leading on medial electrode, 2-4 s interstimulus interval
Transcutaneous ChR2	5.3, 5.5, 5.4, 5.8	median & sciatic nerve	ChR2+ & Wild Type	465 nm LED positioned 1mm from skin 5 ms x 0-330 mW, 0-26 mW/mm^2 2-4 s interstimulus interval
Exposed nerve electrical	5.6, 5.9	forelimb & hindlimb	ChR2+ & Wild Type	200 µs x 0-300 µA, biphasic , concentric blunt needle electrode, center cathode leading, 2-4 s interstimulus interval
Exposed nerve ChR2	5.7, 5.9	median & sciatic nerve	ChR2+ & Wild Type	465 nm LED positioned 2 cm above nerve 5 ms x 0-330 mW, 0-78 mW/mm^2 2-4 s interstimulus interval
Transcutaneous NpHR	5.10, 5.11	forelimb	NpHR+ & Wild Type	1 ms x 0-1.0 mA, biphasic, surface pad electrodes positioned on lateral and medial surface of limb, cathode leading on medial electrode, 2-4 s interstimulus interval, 1 second interstimulus interval. 588 nm laser applied 1 mm proximal to electrode pads with a 300 µm diameter 0.3 NA optical fiber positioned 1.5 cm from the limb. 200 mW at the fiber tip, 200 mW, 3 mW/mm^2 at the skin. Cycled 4 s on, 8 s off.

5.2.3 Data processing

The micro-ECoG signals were processed in Matlab. The signals were highpass filtered (3 Hz corner frequency, 1st order Butterworth), lowpass filtered (750 Hz corner frequency 1st order Butterworth. A 60 Hz notch filter (10 Hz bandwidth, 3rd order Butterworth) was applied in data sets containing power line

noise. These digital filters were applied forwards and backwards to the data to remove phase delays. A set of at least 50 stimuli were averaged for each SEP map unless otherwise noted.

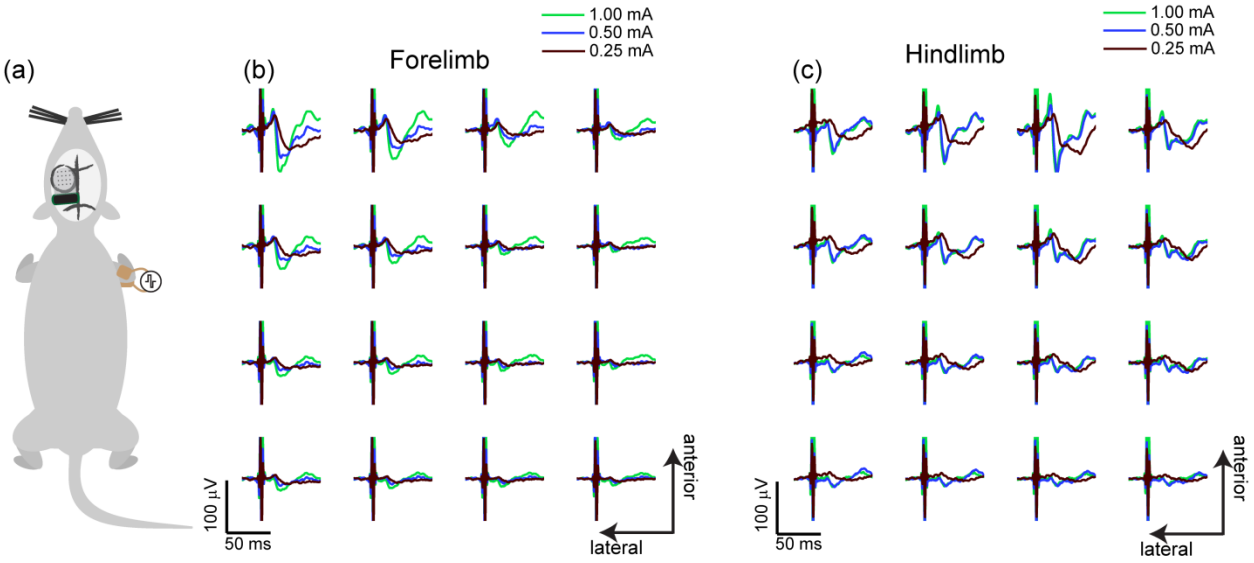

Figure 5.2. Transcutaneous electrical SEPs. The sensory cortex was mapped with the micro-ECoG array while biphasic current pulses (1 ms x 0.25 to 1.0 mA) were applied through surface electrodes to the contralateral forelimb and hind limb as illustrated in (a). Electrical stimulation of the forelimb (b) evoked SEPs that were largest in the anterior-lateral region of the array (i.e. the top left corner), while the hindlimb region was anterior-medial (c). The amplitude of the SEPs depended on the stimulus amplitude.

5.3 Results

5.3.1 Transcutaneous ChR2 SEPs

We began by mapping the sensory cortex of Thy1-ChR2 mice with transcutaneous electrical stimulation of the contralateral forelimb and hindlimb (figure 5.2). The resulting SEPs showed the first peak 15-18 ms following stimulation. This peak required stimulation of the contralateral limb. Ipsilateral stimulation did not recruit this peak (figure 5.4). The forelimb region was lateral to that of the hindlimb as expected by neuroanatomical atlases [86].

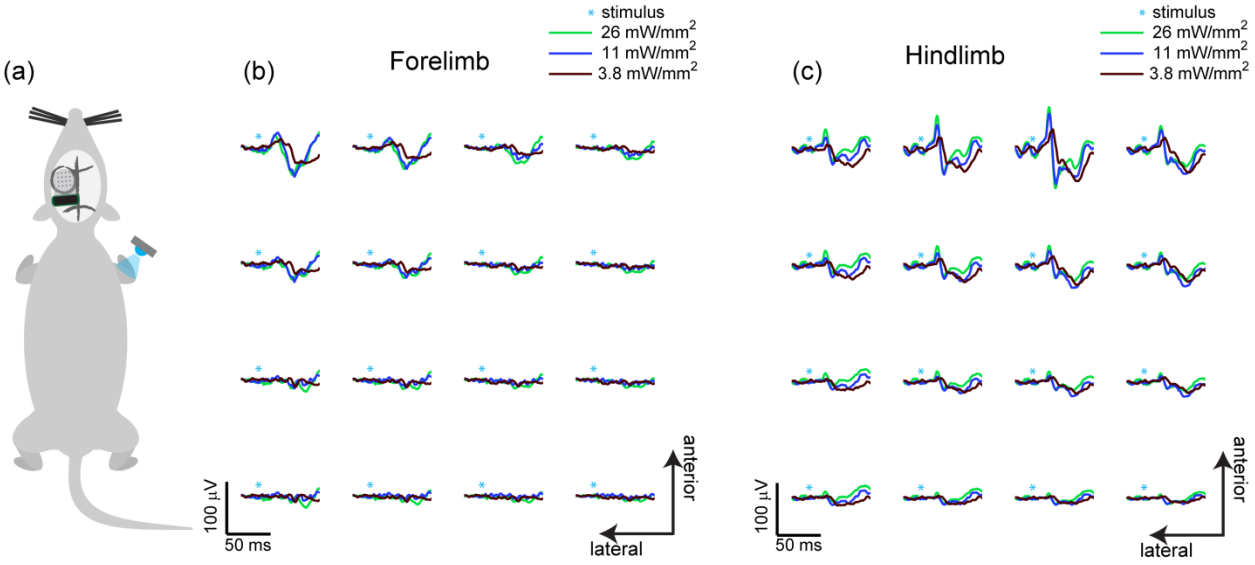

Figure 5.3. Transcutaneous ChR2 SEPs. Blue light (5 ms x 3 to 26 mW/mm^2, 465 nm) was applied to the forelimb and hindlimb in a ChR2 mouse while recording from the contralateral sensory cortex with a micro-ECoG array (a). The resulting forelimb (b) and hindlimb (c) SEPs depended on the intensity of the light pulses applied and they had a similar spatial mapping as with electrical stimulation. The data in figure 5.2 and 5.3 were recorded from the same mouse.

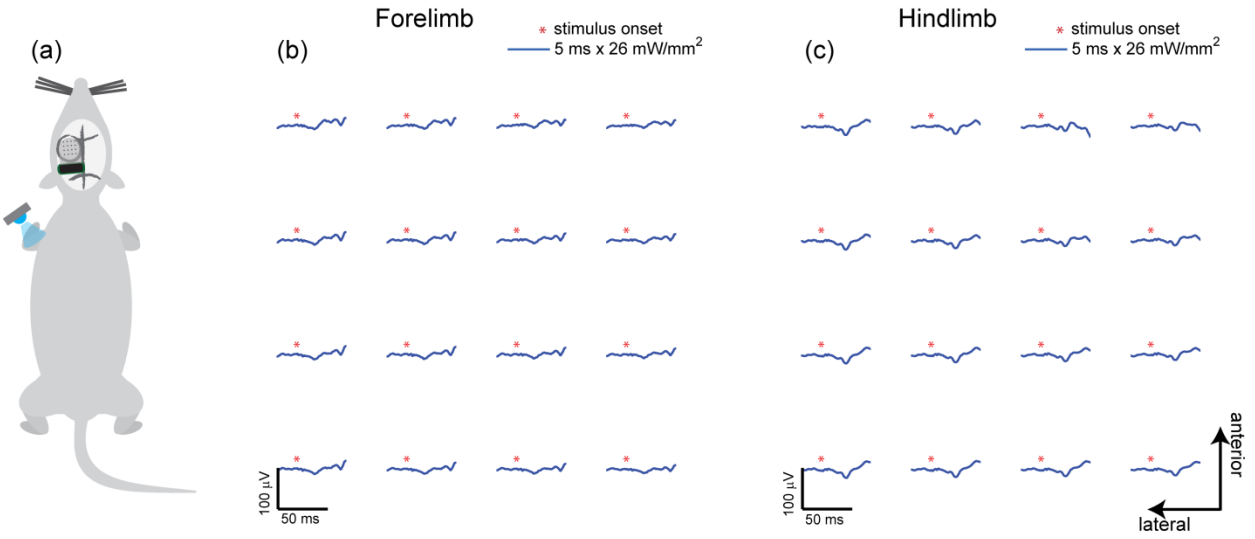

Figure 5.4. SEPs generated by stimulating the ipsilateral limbs of a ChR2+ mouse with a blue LED. The ipsilateral forelimb and hindlimb were stimulated with 5 ms pulses of blue light (465 nm, 26 mW/mm^2, 2-4 s ISI) applied through the skin of the forelimb and hindlimb as illustrated in (a). The resulting SEPs recorded from the micro-ECoG due to forelimb (b) and hindlimb (c) stimulation lack the positive peak at 15 ms that was observed for contralateral stimulation.

The mapping procedure was repeated with the blue LED applied within 1 mm of the skin. The optogenetic SEP waveforms were similar to those evoked by electrical stimulation (figure 5.3). The forelimb and hindlimb localized to the same electrode sites as with electrical stimulation (figure 5.5). The first peak was present and of similar maximum amplitude. It was delayed by a few milliseconds, but this can be attributed to the duration of the blue light pulse (5 ms), compared to the relatively briefer electrical stimulus (1 ms).

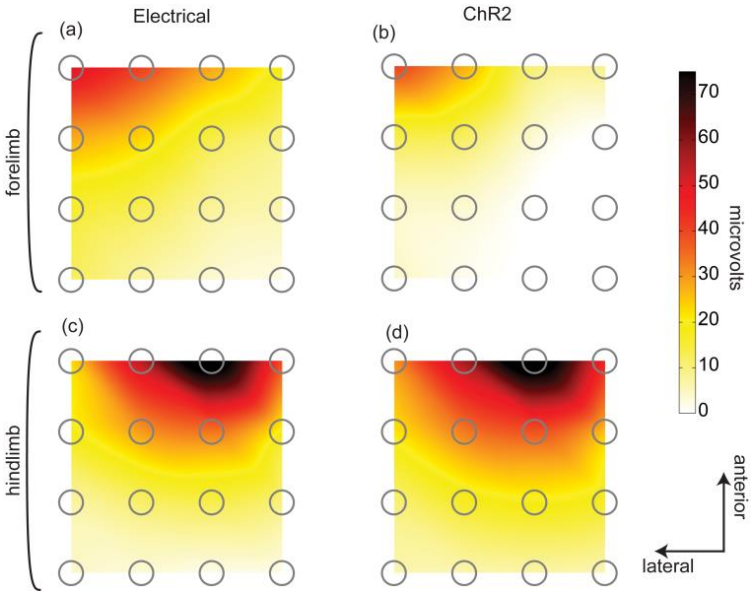

Figure 5.5. Comparison of spatial localization of electrical and optogenetic SEPs. Spatial localization heatmaps were constructed from the data in figures 5.2 and 5.3 by interpolating the peak potential 15-20 ms following stimulation. Both electrical (a) and ChR2 (b) stimulation of the forelimb, generated peak potentials localized to the anterior lateral region of the array. The hindlimb cortical response mapped to a more medial location for both electrical (c) and ChR2 (d) stimulation compared to forelimb stimulation. Electrical stimulation (a & c) matches ChR2 stimulation (b &d).

5.3.2 Direct ChR2 SEPs

On subsequent recording sessions, we anesthetized the mice with ketamine (75 mg kg^{-1} SC), dexmedetomidine (25 µg kg^{-1} SC) and buprenorphine (50 µg kg^{-1} SC), and then surgically dissected to expose the median and sciatic nerves in the forelimb and hindlimb, respectively. This enabled us to direct stimulation these exposed nerves both electrically and optogenetically. A blunt concentric needle electrode was light pressed onto the surface of the nerve with a stereotaxic probe holder. The resulting direct electrical SEPs (figure 5.6) were similar transcutaneous electrical SEPs (figure 5.2). Direct

photostimulation with the blue LED also produced similar SEPs (figure 5.7). Less electrical and optical power were required with direct stimulation of the nerve than transcutaneous stimulation, but the resulting SEPs had qualitatively similar waveforms.

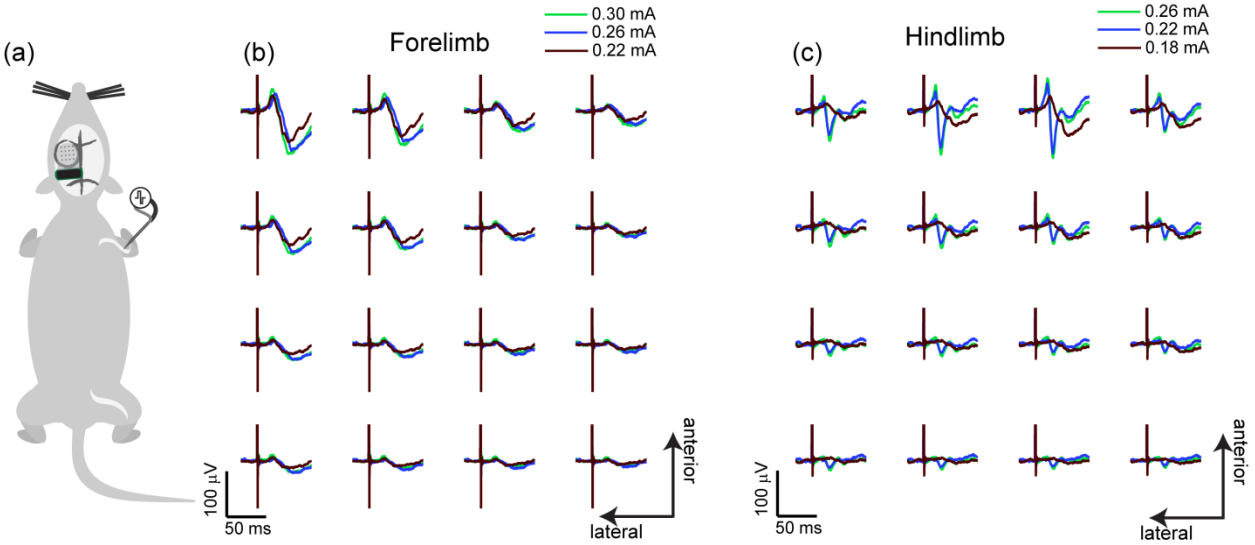

Figure 5.6. SEPs generated by direct electrical stimulation of exposed nerve during terminal recordings. The sensory cortex was remapped by applying electrical stimuli directly to the median and sciatic nerve through a concentric needle electrode (a). Biphasic cathode leading current pulses (200 µs) from the center electrode. The forelimb (b) and hindlimb (c) SEPs were similar to those caused by transcutaneous stimulation.

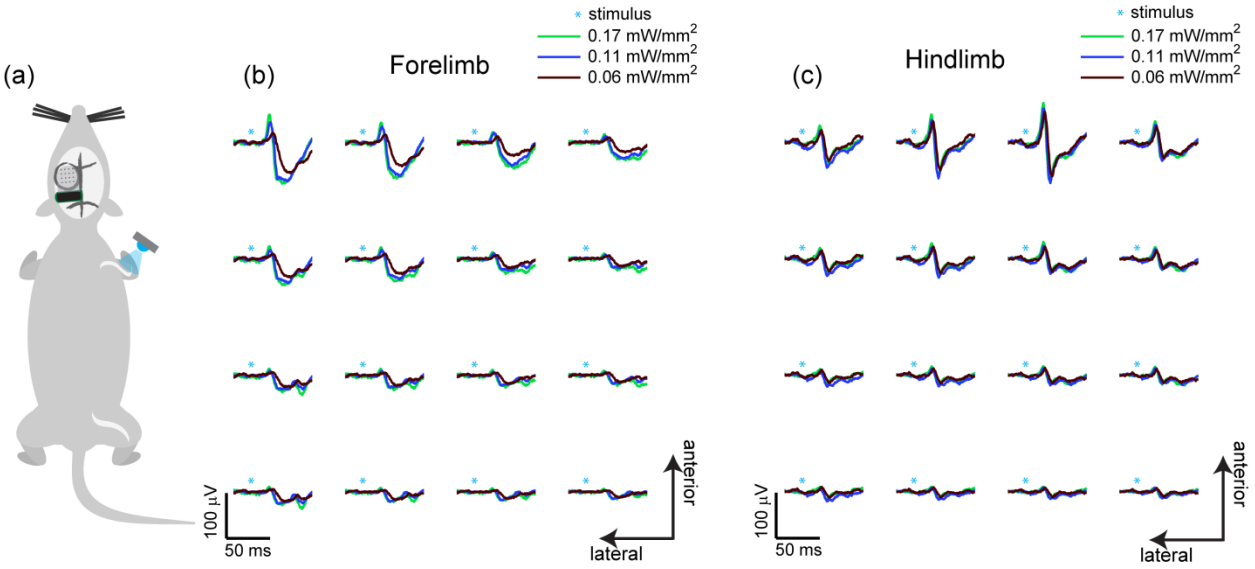

Figure 5.7. SEPs generated by direct ChR2 stimulation of exposed nerve during terminal recordings. Pulses of blue light (5 ms x 0.06 to 0.17 mW/mm^2) directly to the median and sciatic nerve. The resulting forelimb (b) and hindlimb (c) SEPs were similar those evoked transcutaneously, but considerably less light irradiance was required.

For control purposes, we replicated these experiments in wild type mice to determine if applying a blue LED to the periphery induces a sensory signal in the cortex. The cortex could be mapped electrically in wild type mice, but applying a blue LED to the periphery transcutaneously (figure 5.8) or after exposing the nerve (figure 5.9) induced no cortical potentials. This result indicated that the cortical potentials caused by applying blue light to the periphery were optogenetically mediated.

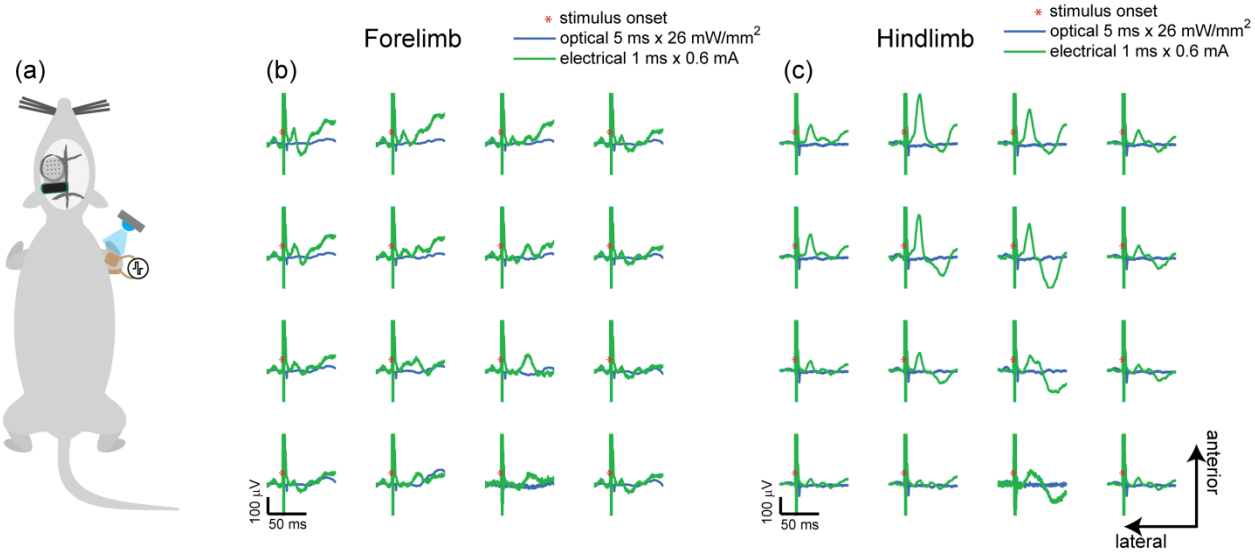

Figure 5.8. Wild type control experiment for transcutaneous blue light stimulation. The protocol used to produce figures 5.2 and 5.3 was repeated in a wild type mouse. SEPs were recorded from a micro-ECoG array implanted over sensory cortex while the contralateral limbs were stimulated as illustrated in (a). Electrical stimuli (1 ms biphasic, 0.6 mA, surface electrode pads, 2-4 s ISI) were used to map the forelimb and hindlimb (green traces in b & c). Stimulation with maximal blue light stimulation parameters (465 nm, 26 mW/mm^2, 2-4 s ISI) did not generate sensory signals (blue traces in b & c) in wild type mice.

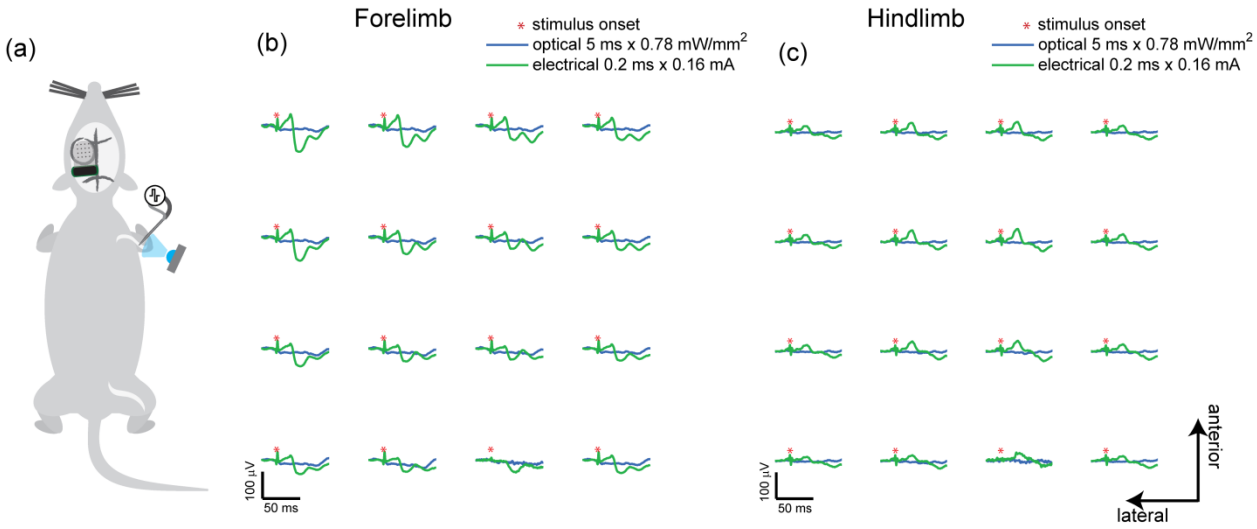

Figure 5.9. Wild type control experiment for exposed nerve blue light stimulation. The protocol used to produce figures 5.6 and 5.7 was repeated in a wild type mouse. The median and sciatic nerve were surgically exposed during a terminal procedure and SEPs were recorded from a micro-ECoG array implanted over sensory cortex while the contralateral limbs were stimulated as illustrated in (a). Electrical stimuli (0.2 ms biphasic, 0.16 mA, concentric blunt needle electrode, 2-4 s ISI) were used to map the forelimb and hindlimb (green traces in b & c). Stimulation with maximal blue light stimulation parameters (465 nm, 0.78 mW/mm^2, 2-4 s ISI) did not generate sensory signals (blue traces in b & c) in wild type mice.

5.3.3 NpHR block of SEPs

We tested whether transcutaneous application of yellow light can be used to block sensory signals in NpHR mice. The forelimbs of NpHR mice were electrically stimulated at 1 Hz to produce SEPs in the contralateral cortex while cycling the yellow laser on and off (4 seconds on, 8 seconds off). The amplitude of the SEPs was smaller when the laser was on, suggesting that signals to the cortex were partially blocked (figure 5.10). Repeating the experiment in a wild type mouse verified that SEPs were identical whether the laser was on or off if the opsin was not expressed (figure 5.11).

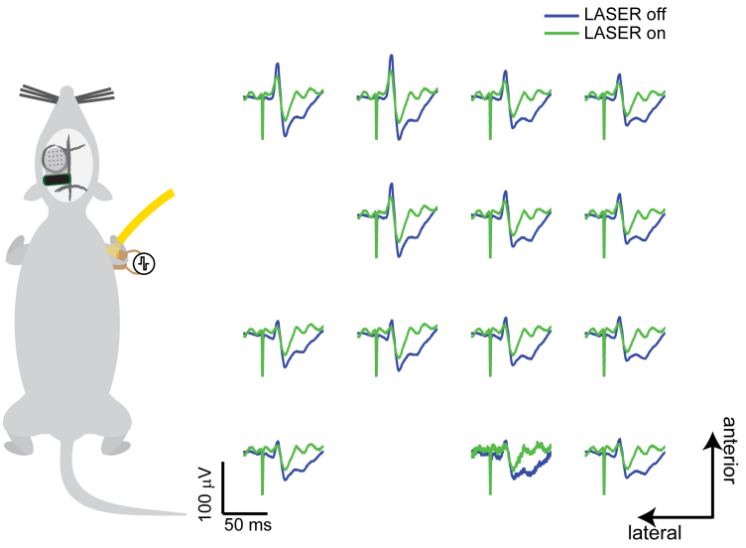

Figure 5.10. Transcutaneous NpHR block of electrical SEPs. The contralateral forelimb was stimulated electrically (1 ms biphasic, 0.20 mA surface electrode pads, 1 s ISI) to generate SEPs while the yellow laser (588 nm, 200 mW, 3 mW/mm^2) was cycled on and off (4 s on, 8 s off). The SEPS were smaller in amplitude when the laser was on.

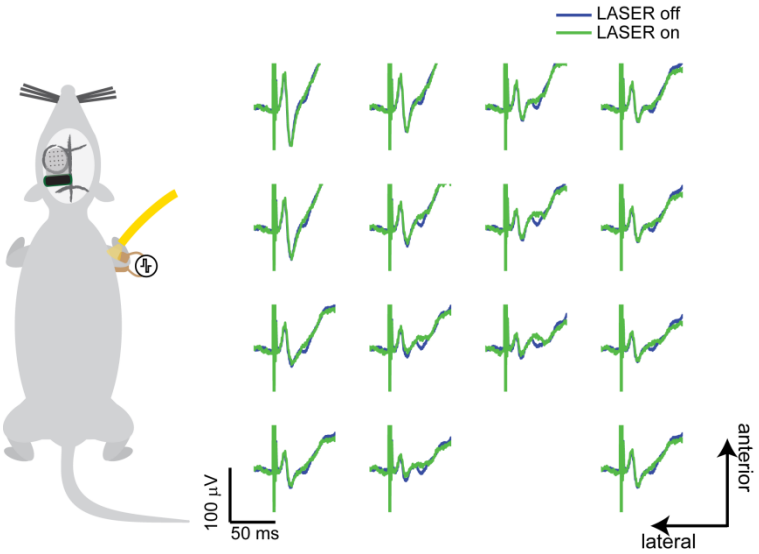

Figure 5.11. Wild type control experiment for transcutaneous application of yellow LASER during electrical SEPs. The protocol used to produce figure 5.10 was repeated in a wild type mouse. The contralateral forelimb was stimulated electrically (1 ms biphasic, 0.20 mA surface electrode pads, 1 s ISI) to generate SEPs while the yellow laser (588 nm, 200 mW, 3 mW/mm^2) was cycled on and off (4 s on, 8 s off). The resulting SEPs are very similar whether the laser was applied.

5.4 Discussion

Transcutaneous application of blue light in ChR2 mice caused cortical sensory signals that were very similar to those evoked by electrical stimulation and more invasive approaches of each method. The short latency of the first SEP peak suggests a rapid propagation velocity, consistent with A_α or A_β fibers. We also demonstrated transcutaneous optogenetic inhibition. Since longer wavelengths generally penetrate tissue further, yellow light has greater potential to reach deeper nerves. However, blocking action potentials optogenetically is generally more difficult than exciting them, because voltage-gated channels help carry out action potentials once initiated. Variable expression levels of NpHR and other factors may explain the lack of a more complete block. This study clears the way for transcutaneous optogenetics to be incorporated into existing electrical sensory stimulation experimental approaches. Other cortical mapping methods such as fMRI could be easily combined with transcutaneous peripheral optogenetic stimulation. Awake-behaving paradigms could also be made amenable by incorporating wireless LED stimulators or other light sources.

Leveraging existing optical hardware could enable the next step in transcutaneous optogenetics. Adding a video projector (i.e. spatial light modulator) to our current setup would enable rapid sensory cortex mapping by targeting specific limbs or portions of limbs in quick succession. An awake-behaving optogenetic subject could be tracked and stimulated using a camera and segmentation software, similar to methods previously reported with C. elegans [155]. Projector technology could also be used to investigate sensory coding. Natural texture discrimination is known to involve spatial and temporal codes of multiple receptor types [237,243]. Multiple sensory fiber types could be optogenetically driven in single digits with spatiotemporal patterns of light to evoke complex sensory precepts, or an individual receptor type could be blocked with NpHR to test its necessity to perception. The cell type specificity of optogenetic sensory stimulation is one of the major benefits of this approach. Cre/lox recombination has been to express ChR2 specifically in pain fibers [233]. Given the numerous Cre [244] and floxed-stop

[245] mice available, and the ease of controlling light with modern optics, considerable cell type-specific exploration remains specific to the peripheral nervous system.

Electrotactile displays [246] and electrical nerve cuffs [247,248] are the most successful and most immediately translatable method for sensory stimulation, but optogenetics may eventually become an additional translatable technology after many hurdles are addressed [240,241]. With nearly 2,000 clinical gene therapy trials to date [249] and with further development of lower risk gene delivery methods, neuroprostheses with optogenetic sensory feedback could be a future approach. Transcutaneous light delivery approaches, as opposed to invasive approaches (e.g. implanted optical fibers), have a lower risk of infection than percutaneous implantation, improving the risk-to-benefit ratio. Still, the feasibility of scaling transcutaneous optogenetic stimulation from rodent models to larger subjects with thicker skin and adipose tissue layers remains an important question as it remains unclear if enough light will penetrate through these thicker tissues to reach the opsin expressing fibers. Long wavelength opsins could improve light penetration, but perhaps optical tissue penetration is not even necessary. ChR2 expression has been reported within superficial layers of the skin and in structures resembling Meisner corpuscles [232]. Superficial opsin expression could enable sensory fibers to be activated preferentially to motor fibers, using tissue absorption to improve the specificity of the approach. The required intensity of light also depends on the expression level of the transgene, a challenge for viral transfection. Intramuscular injection of AAV6 shows promise for the motor system [250], and perhaps intradermal injection would target sensory fibers.

Whether optogenetics can be translated for peripheral applications, the methods described in the current study can be immediately applied to reverse engineering the sensory system with high spatial, temporal, and cell type-specificity.

Chapter 6: Optogenetic assessment of neurovascular and neurometabolic coupling

Abstract

Neurovascular and neurometabolic coupling are essential mechanisms for current whole-brain functional imaging methods. One key technological development to aid in this research has been the integration of optogenetics with fMRI and PET. New insights in brain function can be observed by combining the temporal and spatial functional control of optogenetic stimulation with the large field monitoring capabilities of fMRI and PET. There is great need to understand the hemodynamic and metabolic effects of optogenetic stimulation with high spatial and temporal resolution. We used *in vivo* fluorescence imaging to directly visualize the response of cerebral vasculature and metabolic signals to optogenetic stimulation. Cerebral arteries increased in diameter following photostimulation, while nearby veins showed a smaller response, and the amplitude of the arterial response depended on the area of cortex stimulated. We used a microprojection system to illuminate specific areas of cortex. Reduced nicotinamide adenine dinucleotide (NADH), an endogenous fluorescent enzyme involved in glycolysis and the citric acid cycle, decreased transiently following optogenetic stimulation. We used a transparent substrate microelectrode array to map cortical potentials resulting from optogenetic stimulation to verify optogenetic stimulation of the cortex, and to provide electrophysiologic correlates of the vascular and metabolic studies.

6.1 Introduction

Functional magnetic resonance imaging (fMRI) and positron emission tomography (PET) are powerful techniques for noninvasively imaging the functioning brain. These imaging approaches are based on hemodynamic and metabolic signals subsequent to neural activity. Due to the widespread application of fMRI and PET, studying the causal relationships between neural activity, metabolism, and hemodynamics is of both clinical and experimental interest.

Experimentally testing the underpinnings of fMRI and PET generally involve recording or stimulating neural activity during a scan. The blood-oxygen-level dependent (BOLD) signal has been

found to be temporally correlated with multi-unit activity and local field potentials (LFPs)[251], although direct methods to drive neural activity are needed to address causal relationships. Transcranial magnetic stimulation (TMS) has been used to drive both fMRI[252] and PET[253] signals. While TMS is a useful noninvasive method, it lacks the cell type specificity and spatial localization that is necessary to dissect the causal relationship between activity in distinct neural populations and local changes in vascular dynamics and metabolic activity.

The emerging field of optogenetics offers a variety of tools for activating neurons with high spatiotemporal resolution through a combination of genetic and optical techniques. Optogenetics involves the insertion of light sensitive opsins into the cell membrane to infer optical excitation or inhibition in neural cells[238,9]. The most commonly used techniques involve the use of optically driven cationic channels (e.g. ChR2) to excite activity and ionic pumps (e.g. NpHR and Arch) to inhibit neural activity. Furthermore, cell-type specificity can be achieved through the use of modern genetic techniques to drive expression of opsins in particular cell types via the use of cell-specific promoters. The use of optogenetics in living animal models in conjunction with precision optical delivery methods has created a powerful paradigm for activating distinct neural populations with high spatio-temporal resolution.

Accordingly, approaches combining optogenetics with functional magnetic resonance imaging (fMRI)[6,254,255] and positron emission tomography (PET)[8] are emerging. With the great need for a better understanding of the basis of these new combined imaging methods, particularly as optogenetics is applied to a wider set of neuroscience problems, studying the hemodynamic effects of optogenetic stimulation has become increasingly important. Channelrhodopsin-2 (ChR2) stimulation of pyramidal neurons positively modulates the blood-oxygen-level-dependent (BOLD) signal[6,254,255]. The BOLD signal depends on relative arterial/venous blood volumes, hemoglobin oxygenation and blood flow[256]. Hemoglobin oxygenation and blood flow changes in response to ChR2 stimulation of pyramidal neurons have been described previously[134]. Characterizing the arterial and venous response to neuronal ChR2

stimulation on cerebral artery and venous diameters would help inform applications of biomechanical models of the BOLD response.

In addition to understanding the hemodynamic response to direct neural activation, it is equally important to understand the corresponding metabolic coupling between both neural activity and vascular changes. Exposing genetically targeted neurons to appropriate pulses of light causes rapid depolarization of the cells. Once these targeted neurons are active, they consume a large amount of their adenosine triphosphate (ATP) budget maintaining transmembrane gradients[257]. Nevertheless, the metabolic impact of optogenetically inducing large transmembrane currents and the corresponding homeostatic feedback mechanisms have not been reported. It is known that ATP levels are restored through glycolysis and oxidative phosphorylation. Therefore, positron emission tomography (PET) with 2-deoxy-2-fluoro-D-glucose (FDG) is a suitable method to image metabolic up regulation following Channelrhodopsin-2 (ChR2) stimulation[8]. However, FDG must accumulate over an extended period to form an image, limiting the temporal resolution of this approach. Endogenous fluorescent metabolic co-enzymes, including reduced Nicotinamide adenine dinucleotide (NADH), play key roles in the electron transport chain, providing a direct optical readout of glycolytic and oxidative metabolism. Since the signal is not due to the accumulation or synthesis of NADH, but instead its oxidation to a non-fluorescing form, NAD+, changes in NADH fluorescence intensity occur on much faster time scales. Due to the essential nature of NADH as an electron donor in both glycolysis and oxidative phosphorylation, metabolic transients cannot occur much faster than the rate of NADH to NAD+ conversion, so NADH is an excellent optical imaging target for assaying the rapid metabolic effects of optogenetic stimulation.

A key advantage of optogenetics is its precise spatial activation of nervous tissue through the use of optical focusing or spatial patterning. While the functional organization of the brain and cortex can also enable spatial investigations (e.g. the spatial localization of individual whiskers in rat barrel cortex), optogenetics provides a much more direct route to recruiting activity of different neural volumes through spatial light patterning. Modern optical hardware has enabled the patterning of light at high resolution

through the development of microprojection systems and spatial light modulators such as Digital Micromirror Devices (DMD) and Liquid Crystal Displays (LCD)[258,259]. The use of DMD technology has already been adopted to achieve spatial patterning in a variety of optogenetic applications such as isolation of single neurons and spatial activation of structures in brain slices[155,156,152,159,158].

We describe a novel integrated approach to studying neurovascular and neurometabolic coupling by imaging cerebral blood vessels and NADH fluorescence *in vivo* while applying precise photostimulus patterns through a reinforced thinned-skull window[207] in Thy1-ChR2/H134R mice[216]. We achieved spatiotemporal photostimuli patterning through the development of a custom microprojection and imaging system (figure 6.1). Cerebral arteries increased in diameter following photostimulation, while nearby veins showed a smaller response, and the amplitude of the arterial response depended on the area of cortex stimulated. Excluding major vessels from the photostimulus pattern with a microprojector precluded the possibility of the photostimulus directly acting on vessels or perivascular neurons. Reduced Nicotinamide adenine dinucleotide (NADH), an endogenous fluorescent enzyme involved in glycolysis and the citric acid cycle, decreased transiently following optogenetic stimulation. To verify optogenetic stimulation of the cortex, we also integrated a semi-transparent microelectrode array beneath the cortical imaging window to map optogenetically modulated cortical potentials.

6.2 Materials and Methods

The experimental approach involved imaging cerebral blood vessels and NADH fluorescence *in vivo* while applying photostimulus patterns through a reinforced thinned-skull window[207] in Thy1-ChR2/H134R mice[216]. We tailored the photostimuli spatially and temporally with a custom microprojection and imaging system (figure 6.1).

6.2.1 Microprojection and imaging system

We built a custom optical system to project patterns of blue light for ChR2 excitation of cortical neurons *in vivo*. The microprojection functionality was achieved with a Texas Instruments digital micromirror device (DLP Discovery 4100 Dev. Kit 0.7 XGA, Texas Instruments, Dallas, TX). The DMD

is a light processor consisting of an array of 768 by 1024 bistable micromirrors that can be individually toggled under computer control to create spatiotemporal patterns at 32,552 binary frames per second. The projector's light path (figure 6.1) begins with a high power blue laser (445 nm at 2 watts) which is reflected off of the DMD chip through a Total Internal Reflectance (TIR) prism that can discriminate incoming and outgoing light based on angle. The spatially patterned collimated light reflecting off the DMD chip is sent through a telecentric lens (Xenoplan 1:2, Schneider Optics, Van Nuys, CA) before the coupling of the projection and fluorescence imaging light paths. While a considerable amount of optical power is rejected by the telecentric lens, telecentricity of the projected pattern is highly desirable because it optimizes the uniformity of illumination over the entire field of view and ensures that only light reflected from our intended projection pattern is introduced into the system. The DMD was used to define spatial patterns and to create predefined trains of laser pulses. Rather than pulsing the laser directly, which would potentially destabilize the laser and generate temporal fluctuations in the produced light intensity, we set it to full power during the duration of the pulse train and created the pulses by toggling the DMD to effectively create a pulsed laser signal. We coupled the projection and imaging light paths with a dual channel image combiner (DC2, Photometrics, Tucson, AZ).

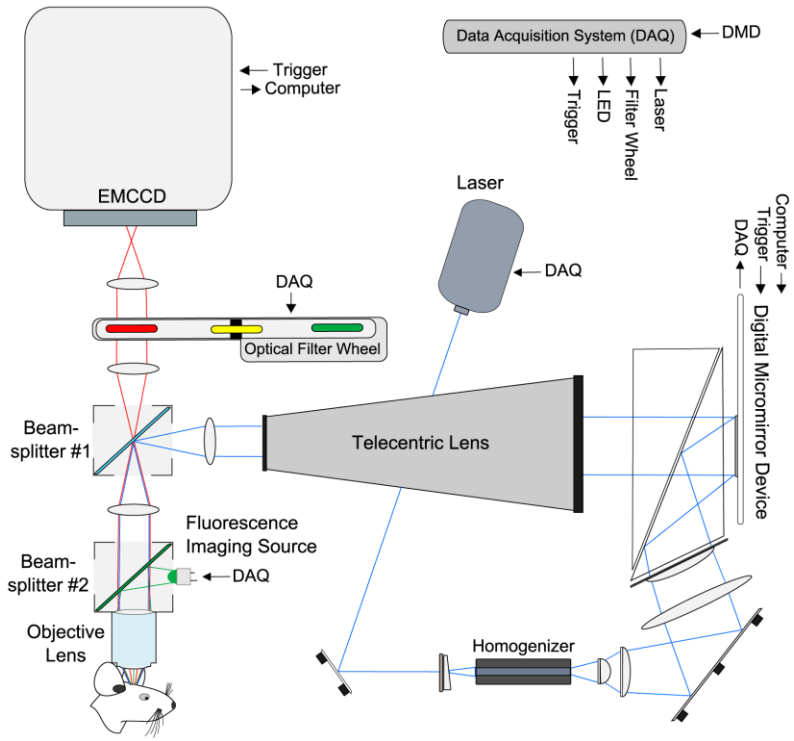

Figure 6.1. Schematic of the microprojection & fluorescence imaging system. A high-powered laser is reflected off a digital micromirror device (DMD) and combined into an epifluorescence light path. This optical system is automated with a data acquisition (DAQ) card, which also receives real-time information from the electrophysiology system's digital signal processor. Figure by Ryan Baumgartner.

We included an epifluorescence light path in our optical system to visualize fluorescently labeled blood vessels and NADH fluorescence intensity. This single photon approach also enabled us to image the photostimuli patterns. We combined the projection and imaging arms of the system with a set of two beamsplitters (figure 6.1). One beamsplitter was the location where we introduced the fluorescence excitation light, while the other beamsplitter introduced the patterned optogenetic stimulation light. We were able to apply the patterned optogenetic stimulation light and fluorescence excitation light to the cortex and pass the emitted light through to the camera by carefully selecting dichroic mirrors and beamsplitters for each experimental setup (Table 1). We used an electron multiplying charge coupled device (EMCCD) camera (Evolve 512, Photometrics, Tucson, AZ), which provides high sensitivity, to help pick up the relatively faint NADH signal.

The control software for the optical device was implemented in Labview. We controlled the LASER and other light sources with a digital acquisition (DAQ) card (NI-USB 6211, National Instruments,

Austin, TX), and the DMD and EMCCD are directly connected to the computer via manufacturer electronics. We also used the DAQ to synchronize the optical system with the electrophysiology system.

6.2.2 Cranial window implantation

All procedures were approved by the institutional animal care and use committee at the University of Wisconsin-Madison. These studies were done in accordance with the NIH's Guide for the Care and Use of Laboratory Animals and in accordance with the ARRIVE (Animal Research: Reporting *In Vivo* Experiments) guidelines.

We implanted five Thy1::ChR2/H134R-YFP mice (Jackson #012350) and five wild type mice (10-20 weeks, males & females) with a reinforced thinned-skull cranial window[207]. One ChR2 and one WT mouse were excluded because the middle cerebral artery was not visible under the cranial window. The remaining group size was sufficient to power the comparison given the large effect size. Researchers were not blind to mouse genotype in this study. Animals were anesthetized with isoflurane (1.5-2.0 % in oxygen) and administered buprenorphine (50 µg/kg subcutaneous (SC)) for analgesia. The calvarium was exposed and a thin titanium plate was fixed to the bone with cyanoacrylate to stabilize the head during surgery and imaging. A clamp held the titanium piece and a 4 mm diameter area of the skull was thinned with a high-speed surgical drill (FM3545, Foredom Electric, Bethel, CT) and spherical burr (#105 & #106 Dremel, Mount Prospect, IL). A 3 mm diameter piece of sterile #1 cover glass (Warner Instruments, Hamden, CT) was glued over the thinned area. Blue light, which could excite ChR2, was removed from the surgical lights with a 550 nm longpass optical filter (FGL550, Thorlabs, Newton, NJ). Mice were given seven days of antibiotic treatment (ampicillin, 100mg/kg BID), and given at least two days of rest before the initial imaging sessions.

We implanted two Thy1::ChR2/H134R-YFP mice with custom micro-electrocorticography (micro-ECoG) electrode arrays under a standard (not thinned) cranial window to map optogenetically evoked cortical electrophysiological potentials[112]. The micro-ECoG arrays[32,112] were implanted on top of the dura matter to localize cortical activity across the surface of the brain. We used photolithography to

define sixteen platinum electrode sites (150 μm diameter) in a 4x4 grid (0.5 mm site-to-site spacing). We selected Parylene-C, a transparent polymer, as the electrically insulative substrate, so that photostimuli could be applied to the cortex, through the window and transparent array. The implantation procedure was similar to the thinned-skull cranial window method described above, except a 3 mm diameter craniotomy was performed, the array was placed, and UV dental acrylic (Fusio, Pentron) was used to secure the electrode connector. The window was occluded while hardening the acrylic to prevent activation of ChR2 from the UV light source.

6.2.3 Imaging and electrophysiology sedation

Mice were sedated with boluses of ketamine (75 mg/kg SC) and dexmedetomidine (25 μg/kg SC) during blood vessel imaging, NADH imaging, and cortical potential mapping sessions. The mice were also given glycopyrrolate (0.02 mg/kg SC) to maintain adequate heart rate and decrease respiratory secretions. The head was held still by stabilizing the piece of titanium that was incorporated during implantation with a clamp. Supplemental oxygen and heat were provided. At the end of the procedure, atipamezole (0.5 mg/kg SC) was given to reverse the dexmedetomidine.

6.2.4 Vascular imaging

Rhodamine B isothiocyanate-dextran (Sigma, 70 kDa) was injected into the tail vein to fluorescently label the cerebral vasculature. The dye was dissolved in saline at 6 mg/ml and sterile filtered into aliquots before freezing. An aliquot was thawed and 0.05-0.10 ml was injected into the tail vein under isoflurane prior to each imaging session. Epifluorescence images of the cortical surface were collected at 7 frames per second through a superfluor 10x air objective (Nikon) with a numerical aperture (NA) of 0.50 and a working distance of 1.2mm. Mirror #1 (refer to figure 6.1) was a dichroic with longpass cutoff at 500 nm. We used a 50%-50% beam splitter for mirror #2, because it needed to pass blue photostimulation light, reflect green fluorescence excitation light, and pass red emitted light. Rhodamine B was excited with green light (550/40 nm, 1 mW total power) from a xenon light source (DG-4, Sutter Instruments, Novato, CA) and a red emission filter 590/20 nm was positioned in front of the camera. The vessels were imaged

during each trial for 10 seconds prior to the photostimulus and 30 seconds following the stimulus. The photostimulus (4.5 mW/mm^2, 445 nm) was applied for 1 second and pulsed at 25 Hz (20 ms on, 20 ms off). Trials were repeated every 1 to 2 minutes, and 7 trials were done for each photostimulus pattern.

6.2.5 NADH imaging

We imaged NADH fluorescence intensity using standard (single photon) excitation. NADH has an excitation peak near 350 nm and an emission peak near 450 nm. We used extremely low levels of UV light to minimize UV damage to the cortex and to avoid excitation of ChR2. 8 μW/mm^2 has been suggested previously as a safe level for prolonged *in vivo* NADH imaging[260]. We used a UV LED (365 nm, Thorlabs, Newton, NJ) and an OD1 neutral density filter (NE10B-A, Thorlabs, Newton, NJ) to reduce the light level to 8 μW/mm^2. We observed no photobleaching of NADH at this level, and the light intensity is orders of magnitude below the level that could excite ChR2 appreciably. Using the EMCCD camera enabled effective imaging of the faint NADH signal.

6.2.6 Cortical potential mapping

Signals were recorded from the cortical surface using a 16-channel micro-ECoG electrode array (see figure 6.8). The array was connected to a high-impedance headstage, which was referenced to a coiled wire implanted over the contralateral cortical hemisphere. Evoked signals were produced by photostimulation of a limited region of cortex (figure 6.8 a & b). The signals were recorded at 3 kHz (RZ2, Tucker Davis Technologies, Alachua, FL), band-pass filtered from 1 to 500 Hz and subsequently averaged across all trials for a specific stimulus location. Localization heatmaps (figure 6.8 c & f) were generated by cubic interpolation of the average evoked response on each channel.

6.2.7 Data analysis

Image data were analyzed with Matlab and FIJI[261]. Images were registered to the nearest 0.01 pixels using the 2D DFT correlation method[262]. To determine vessel diameters, measurement locations were specified on each vessel manually and a band was defined along the axis of the vessel over which the data were spatially averaged. The vessel width was measured as the full width at half-maximum, and

a 3 point median filter and 3 Hz low pass filter were applied similar to Drew et al.[263]. We removed the blood vessels to prevent confounds due to changing vessel diameters for the NADH region of interest (ROI) analysis. We segmented the vessels with the Tubeness plugin[264] and then padded this further by eroding the image by 2 pixels.

6.3 Results

6.3.1 Arterial & venous dilation due to ChR2 stimulation

Branches of the middle cerebral artery (MCA) dilated transiently following photostimulation (20 ms pulsewidth at 25 Hz for 1 second, 4.5 mW/mm^2, 445 nm) of the cortex (figure 6.2), recovering to prestimulus diameters after several seconds. The hemodynamic response was robust, with significant changes occurring in every individual trial. Branches of the MCA dilated more than 30% for the large photostimulus, but nearby veins showed a much smaller and somewhat delayed response.

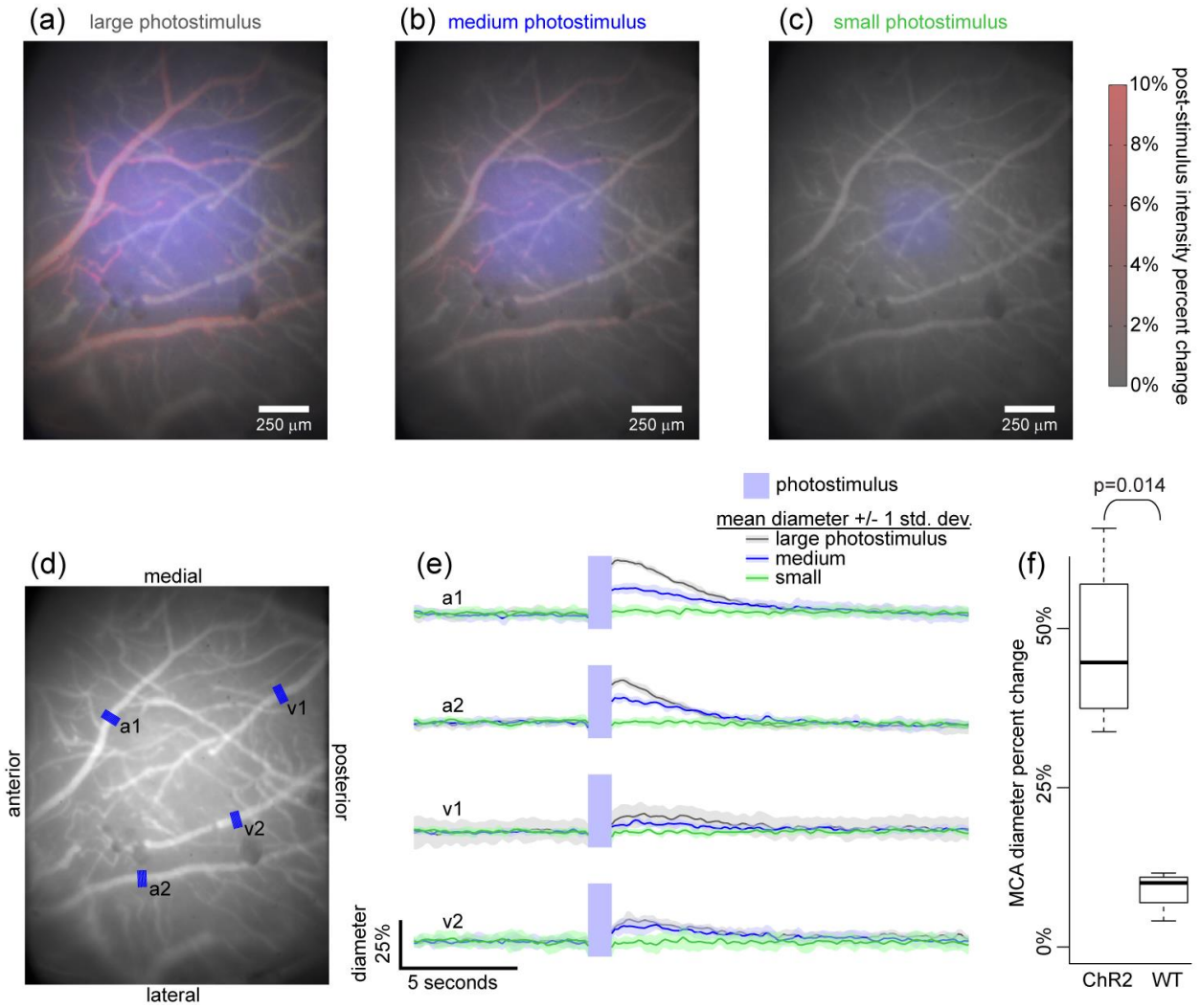

Figure 6.2. Arterial vasodilation depends on area of optogenetic stimulation. Large (860 x 860 μm), medium (570 x 570 μm), and small (320 x 320 μm) photostimulus squares were applied (a-c, overlaid in blue). Each of these photostimulus patterns were applied as a pulse train with the irradiance held constant (20 ms pulsewidth at 25 Hz for 1 second, 4.5 mW/mm2, 445 nm). The average prestimulus image is shown in gray with post stimulus percent change shown in red (a-c). The large (a) and medium (b) photostimuli caused the middle cerebral artery branches to dilate, while the veins showed little response. (d) Based on anatomic reference 49, branches of the middle cerebral artery, which originate lateral and anterior were identified as a1 and a2, while medially originating veins were labeled v1 and v2. (e) Time-series diameter quantification of the middle cerebral artery (MCA) branches (a1 & a2) showed a 30% increase following the large area photostimulus, while the medium area photostimulus caused a 15% diameter increase, and the small area photostimulus caused little to no vasodilation. The venous response (v1 & v2) was much smaller compared to the MCA,. Seven trials of each stimulus area were conducted per animal. (f) The study was replicated in 4 ChR2 positive mice and 4 wild type mice, and the median percent change of the middle branch of the MCA was significantly larger in ChR2 mice than in WT mice at the α=0.05 confidence level (one-tailed signed rank test).

The magnitude of both the arterial and venous response depended on the cortical area excited by optogenetic stimulation. We used the microprojector to create photostimulus patterns of different geometric areas while holding optical power per area (irradiance) constant. Three different photostimulus sizes were investigated, each consisting of a square that progressively increased in width, from 320 microns (small) to 570 microns (medium) and 860 microns (large). The smallest photostimulus area evoked little to no hemodynamic response, while the larger two photostimulus patterns evoked responses proportionate to the cortical area that was stimulated. Since fMRI artifacts have been reported in wild type (WT) rodents at high photostimulus levels[6,254], we replicated our study in both ChR2 expressing (n=4) and WT (n=4) mice (compare figures 6.2 and 6.3). The median arterial response to the large photostimulus was significantly ($p=0.014$, one-tailed signed rank test) larger in ChR2 than WT mice (figure 6.2f), although the response in WT mice was nonzero.

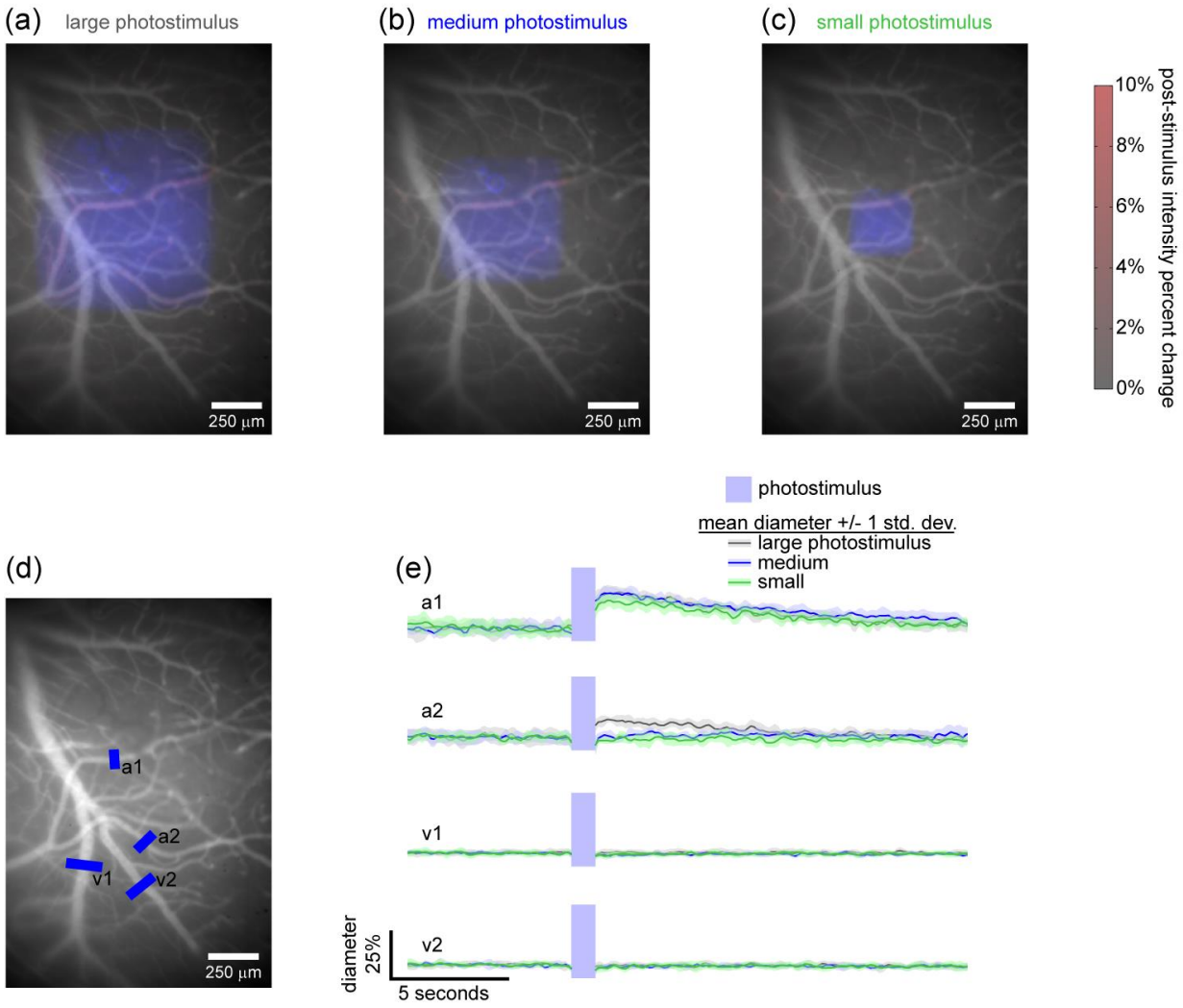

Supplementary figure 6.3. Vascular diameter changes due to photostimulation were minimal in wild type controls (compare to figure 2). Photostimuli of three different size areas were applied (a-c). A small stimulus artifact was observed following photostimulation (e), but the amplitude of this change was always much smaller in wild type mice than ChR2+ mice (see figure 2f).

We used the microprojector (figure 6.1) to investigate whether direct photostimulation of the major cerebral vessels was responsible for the hemodynamic response that was observed. We explored this avenue, because if perivascular nerves express ChR2, then a direct cholinergic mechanism could explain the optogenetic hemodynamic response. We applied a solid photostimulus pattern (figure 6.4a) and a pattern with the major cerebral vessels removed (figure 6.4b). The resulting hemodynamic responses (figure 6.4d) were very similar. If perivascular neurons had been involved, we would have expected a disproportionately smaller hemodynamic response for patterns with vessels omitted. To rule out any

electromagnetic interference (EMI) artifacts or effects due to visual stimulation, a set of control experiments was performed with the DMD turned off, while still activating the laser (figure 6.5). These experiments (figure 6.4 along with figure 6.5) show that neither direct projection onto the measured vessels nor other potential artifacts (EMI, visual stimulation) can account for the observed hemodynamic response. Given that projection onto the vessels has little effect and the significantly larger effect in ChR2 than WT mice, the observed response is most consistent with the explanation that optogenetic drive of pyramidal and postsynaptic cells leads to vasodilation through one or more neurovascular coupling mechanisms.

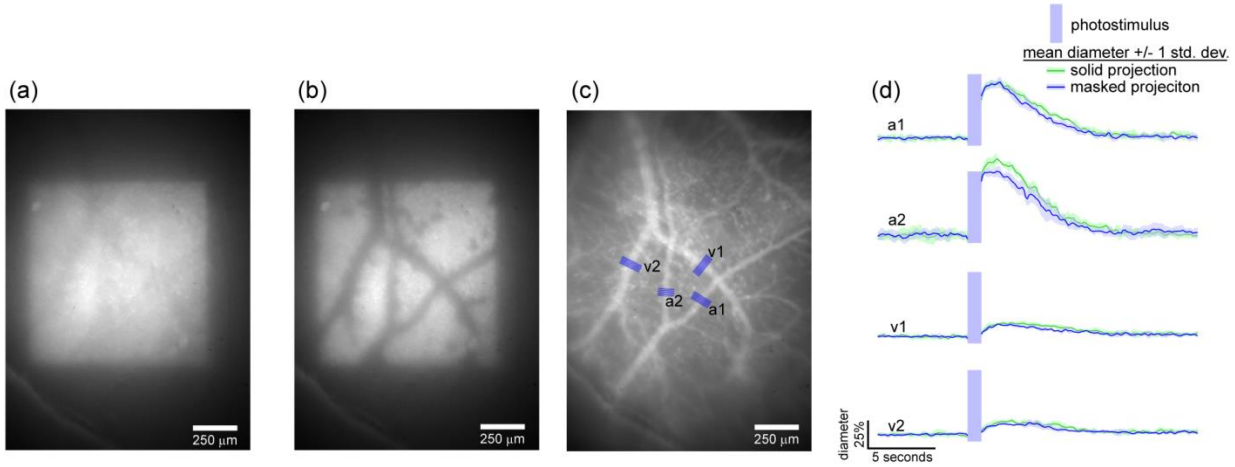

Figure 6.4. Projection avoiding major blood vessels comparison. We projected either a solid square (a) or pattern with the blood vessels omitted (b). The other photostimulation parameters (20 ms pulsewidth at 25 Hz for 1 second, 4.5 mW/mm2, 445 nm) were held constant. The vessels were measure at the sites labeled in (c). The hemodynamic response (d) was similar for the solid and blood vessel avoiding stimulus patterns. This experiment helps test for the effect of directly photostimulating the blood vessels and their associated perivascular nerves.

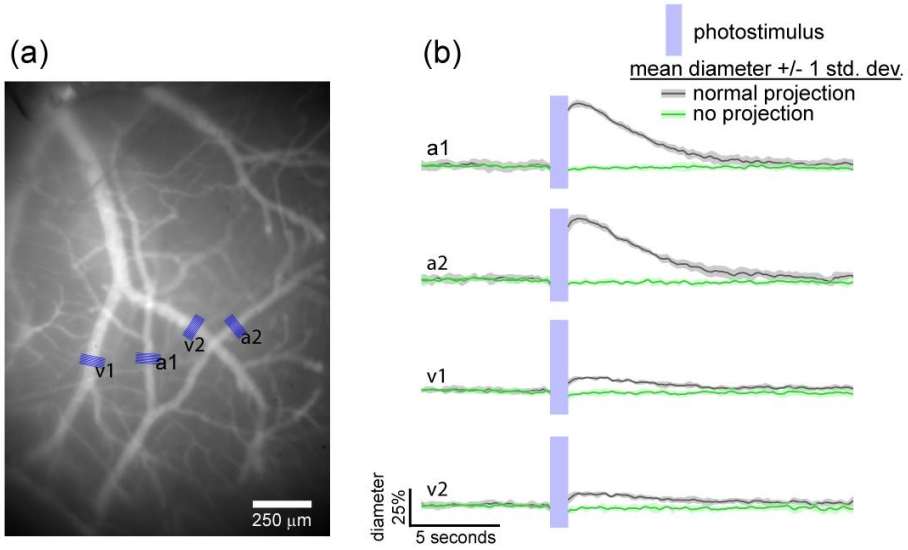

Figure 6.5. No projection control. The blood vessels of a ChR2+ mouse show no change with the DMD chip turned off (resulting in no projection) while the high power laser still operating. This basic control experiment shows that projecting blue light on the cortex is required. Visual stimulation due to the high power laser turning on during the stimulus did not cause any artifact in the recorded hemodynamic signal.

6.3.2 ChR2 induces a rapid metabolic transient

We imaged NADH fluorescence intensity as a signature of the metabolic status of the cortex following ChR2 photostimulation (5 ms pulsewidth at 66 Hz for 1 second, 445 nm, 4.5 mW/mm^2). When oxidized, NADH, an endogenous fluorescent protein involved in the citric acid cycle, glycolysis and other key metabolic pathways, becomes NAD+ and loses its fluorescence. The NADH signal decreased by about 4% following photostimulation and it recovered over several seconds (figure 6.6). This effect was not observed in wild-type mice (figure 6.6g and 6.7). As in the vascular experiment, the peak amplitude of the NADH response depended on the area of stimulation.

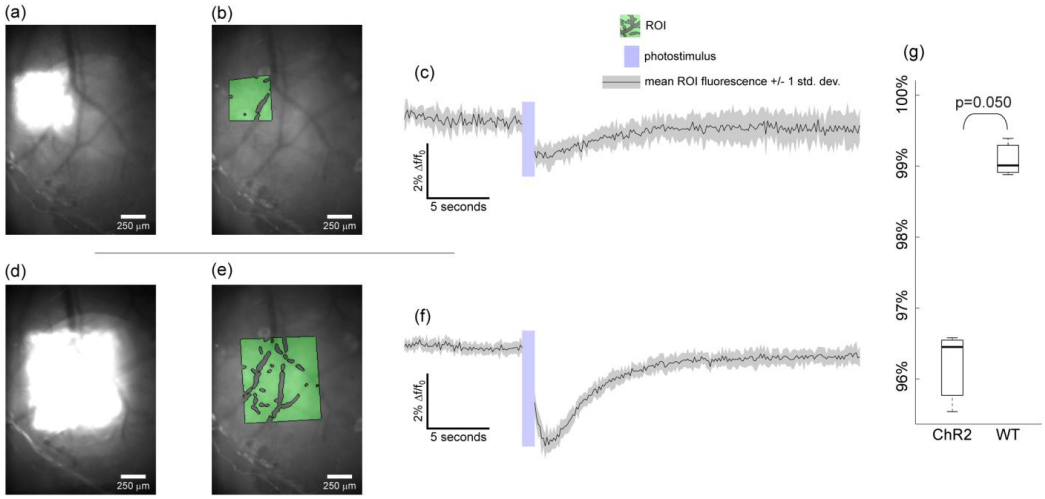

Figure 6.6. Transient metabolic increase following ChR2 stimulation. Nicotinamide adenine dinucleotide (NADH) is a coenzyme involved in cellular metabolism. Under increased metabolic load it is oxidized to NAD+. NADH fluoresces while NAD+ does not. We imaged this fluorescent signal before and after ChR2 stimulation (5 ms pulsewidth at 66 Hz for 1 second, 445 nm, 4.5 mW/mm2) of different cortical areas. The large area stimulus (d) caused a correspondingly large decrease (f) in the fluorescence intensity of the region of interest (ROI) displayed in (e). The smaller area photostimulus (a) caused a smaller response (c). 10 trials were conducted at each location per animal. The study was replicated in 3 ChR2 mice and 3 WT mice with the peak fluorescence change for the large photostimulus plotted in (g). A p-value of 0.05 was found for a one-tailed signed rank test.

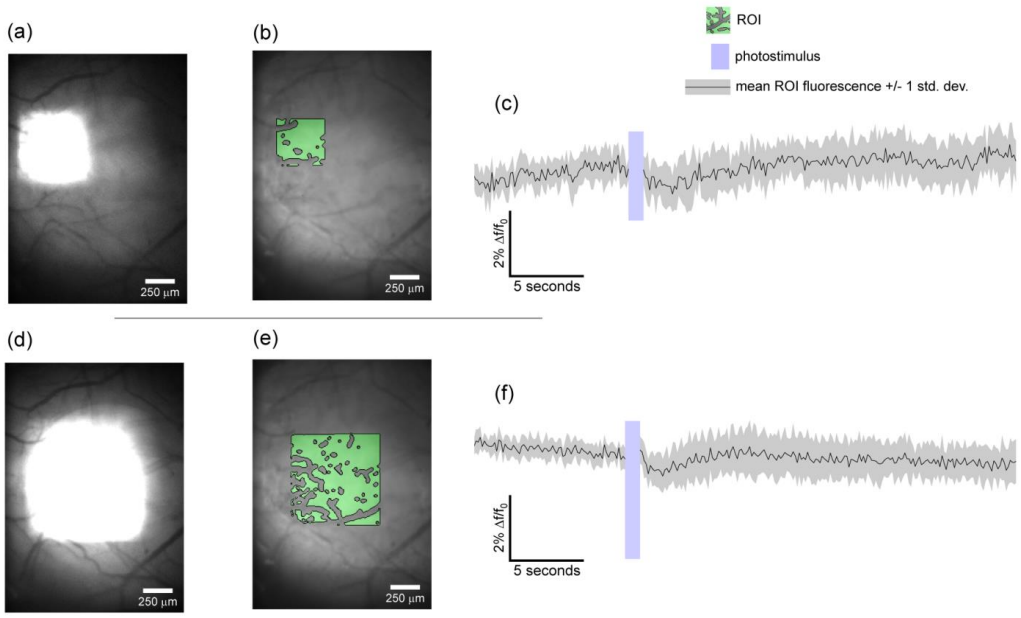

Figure 6.7. Wild type NADH control. Projecting a small (a) or large (d) photostimulus onto the cortex of a wild type mouse did not cause a change in the NADH fluorescence intensity (c) & (f). Blood vessels were excluded from the ROIs (b) & (e).

6.3.3 Colocalization of photostimulus and cortical potentials

Since neurovascular and neurometabolic coupling begin, causally, with neural activity, we mapped cortical potentials evoked by optogenetic stimulation (figure 6.8). We fabricated electrode arrays on a transparent insulative polymer so that when implanted on top of the dura matter and under a cranial window, photostimuli could still be patterned onto the cortex[191]. The potentials were of greatest amplitude near the photostimulus location, suggesting that stimulus-correlated activity is predominantly colocalized with the photostimulation location. Stimulating larger cortical volumes (figure 6.9a) induced larger amplitude potentials spread over a larger cortical area. When we used the microprojector to avoid projecting onto the electrode sites and traces (figure 6.9b), the recorded potentials were nearly the same (figure 6.9c), ruling out any significant photoelectric effect. The photoelectric effect for these types of electrodes has been characterized previously[191].

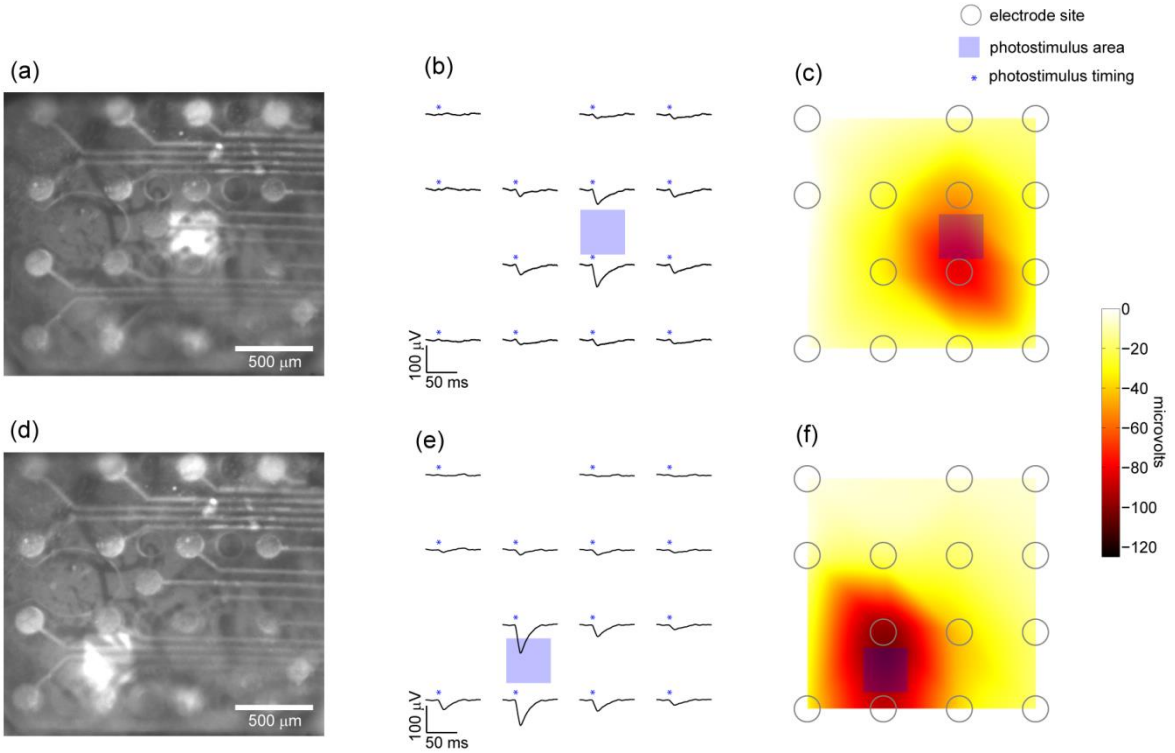

Figure 6.8. Optogenetically evoked potentials colocalize with the photostimulus location. We implanted microfabricated electrocorticography electrode arrays under a cranial window in Thy1-ChR2/H134R mice (a, b, g). Photostimulation of small areas (a & b) caused optogenetically evoked potentials (b & e, respectively) that were largest at sites nearest the stimulus. The stimulus was easily localized with cubic spline interpolation (c & f) of the peak potentials.

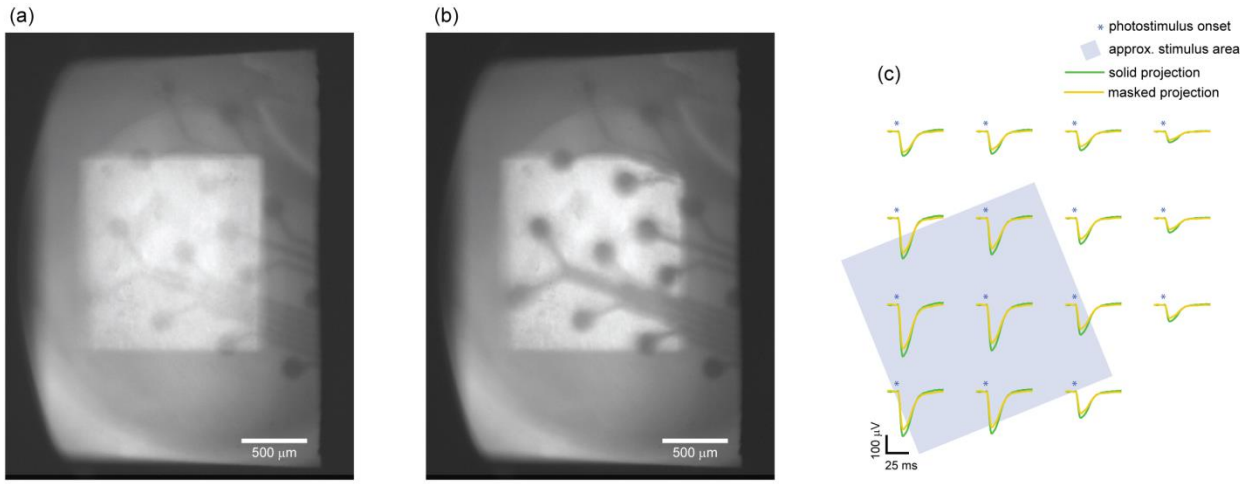

Figure 6.9. Photostimulation based on imaging. We co-registered the microprojector's pixels with the camera pixels so that we could create photostimulus patterns based on images. In (a) we projected a solid square, while in (b) we avoided projecting onto the electrode sites and traces. The resulting potentials from (a) and (b) were nearly identical in amplitude (c).

6.4 Discussion

Optogenetic excitation of pyramidal neurons caused arterial dilation and venous distension. The amplitude of venous distension was relatively modest. More prolonged photostimulus pulse train (>10 seconds), like those used in optogenetic fMRI and PET protocols, may have caused a larger and cumulative venous response. Our findings were consistent with previous sensory stimulation investigations which found that arterial volume changes are larger than venous volume changes for brief stimuli[263]. Further investigation of the dependence of the differential response between arteries and veins on the duration of the photostimulus should be explored to better inform the interpretation of optogenetic fMRI. Interestingly, and perhaps uniquely to this study, due to the use of a microprojector, the amplitude of the arterial and venous response depended on the area of cortex stimulation.

Additional studies that investigate the specific neurovascular coupling mechanisms involved are needed. Astrocyte mediated and nitric oxide induced vasodilation should still be explored in the context of optogenetics. We were able to rule out the direct photostimulation of perivascular nerves causing a disproportionate contribution to the hemodynamic response by using blood vessel-avoiding photostimulus patterns (figure 6.2). The microprojector could be used in future experiments to investigate the spatial

relationship between activated regions and blood vessel proximity. Spatial activation studies of the neurovascular coupling could also be done with sensory (e.g. whisker barrel field) stimulation, but optogenetic stimulation enabled defined areas to be easily targeted (figure 6.2). Replicating this study with other transgenic lines to investigate other cell types, such as GABAergic interneurons[216], would be of great interest and would exemplify the cell type-specificity of this method.

The cationic currents induced by ChR2 stimulation appear to cause a rapid change in the NAD+/NADH redox state. It is likely that cellular membrane currents and downstream metabolic processes are temporally tightly coupled. Other metabolically demanding cellular events (e.g. neurotransmitter release) could also be affected indirectly by optogenetically induced metabolic transients. Since ChR2 stimulation led to NADH oxidation, and NAD+/NADH is involved in glycolysis and citric acid cycle, our findings are consistent with the understanding of the PET brain glucose metabolism study[8]. As is necessary for PET, they used lengthy photostimulus patterns (30 s on/ 30 s off). We found that only one second of stimulation evoked sizable metabolic changes. Effects of similar amplitude have been reported using electrical stimulation in brain slices[265,266]. *In vivo*, electrical stimulation was previously found to not only induce a NADH transient, but to also increase extracellular potassium concentration $[K^+]_o$[267]. Severely increased $[K^+]_o$ is associated with cortical spreading depression (CSD)[268] and is also theorized to play a large role in migraine with aura[269], a pathophysiology resulting in dilated cerebral vessels. Moderate increases in $[K^+]_o$ are known to activate inward rectifier K^+ channels in the smooth muscles cells lining arterioles, leading to vasodilation[270]. This is one of several neurovascular-coupling mechanisms that are likely involved in the optogenetic hemodynamic response.

Photostimulus related fMRI artifacts have been reported in wild type subjects by multiple groups[6,150]. We conducted our study with both ChR2 expressing and WT mice to control for this potential artifact. The vascular and NADH response in WT mice was non-zero, indicating that there was an artifact, but the response in ChR2 expressing mice was always significantly larger (figure 6.2f and

figure 6.6g). We chose a photostimulus irradiance level (4.5 mW/mm^2) that was greater than, but close to the presumed minimum (1 mW/mm^2) for exciting ChR2 *in vivo*[271]. The use of transgenic mice rather than viral transfection in rats may have allowed us to use less light. New opsin variants that are more sensitive, pass more current, stay open longer and are activated by longer wavelengths[272] may reduce the artifact problem by requiring less light to be applied.

New technological approaches that integrate optical imaging and optogenetic stimulation could push forward the study of neurovascular coupling. Optical coherence tomography could be used to image vascular diameters and blood flow hundreds of micrometers, or even millimeters, into the cortex as it responds to optogenetic modulation. Two-photon excitation has been successfully applied to optogenetically excite individual neurons[122], and two-photon imaging has been widely used to study neurovascular coupling[273], so entirely two-photon based imaging and optogenetic approaches may be possible with further developments to excite larger populations of neurons.

Optogenetic stimulation of pyramidal neurons causes both hemodynamic and metabolic changes in the cortex. One second of photostimulation was sufficient to produce sizable and rapid effects that could be imaged optically. For these relatively brief stimulus trains, arteries dilated more than veins, and the amplitude of vasodilation corresponded to the area of cortex recruited. Similarly, the amplitude of the NADH response depended on photostimulus area, and the time course of the NADH signal suggested tight temporal coupling between cationic fluxes and cellular metabolism. Our findings provide direct optical evidence in support of studies using optogenetics with fMRI and PET, and the DMD optical system we developed provides a platform for spatially and temporally precise cell type-specific neurovascular and neurometabolic coupling studies.

Chapter 7: Discussion & Future Directions

7.1 Introduction

The goal of developing an understanding of signals measured at the cortical surface based on intracortical neural activity spans the research presented in the previous chapters. Cortical potentials and hemodynamic signals measured epidurally were linked to neural activity within the cortex. We leveraged additional technologies, beyond micro-ECoG and neurovascular imaging, to either record or directly modulate cortical activity. Results from these approaches were often complimentary, and these newly integrated technologies exist as neural interfaces to further study the cortex.

7.2 Synthesis of results

Micro-ECoG signals are related to spikes recorded within the cortex, and a portion of the micro-ECoG signals results from localized current sinks. Subsets of sorted spiking neurons are significantly phase coupled to the micro-ECoG signal in a brain state (figure 3.4) and stimulus (figure 3.7) dependent manner. Spikes are the fundamental unit of neural activity, and they generate larger current sources when acting in synchrony. Driving synchronous depolarization with optogenetic stimulation from the cortical surface created large current sinks near the surface and resulted in negative micro-ECoG potentials (figures 4.3 and 4.7), but creating current sinks deeper within the cortex resulted in positive micro-ECoG potentials (figure 4.10). The location of depolarization affected the phase of the resulting cortical potential, consistent with the originally hypothesized interpretation of CSD analysis [101]. Taken together, these results suggest the hypothesis that synchronized spikes generate current sinks that result in a component of the micro-ECoG signal. This hypothesis could be tested by combining the methodology described in chapters 3 and 4. Micro-ECoG and intracortical arrays would provide a 3D sampling of potentials within the cortex. CSD analysis generalized in three dimensions [274] could be applied to localize activity beyond the knowledge of where the stimulus was applied, and complex cross coherence between spikes and micro-ECoG signals could be analyzed as a function of optogenetic drive. These

studies would help further the understanding of signal generators from different cortical layers, along the vertical dimension.

Optogenetic stimulation of the cortex and SEPs provide complimentary views of micro-ECoG neural source localization across the cortical surface, the horizontal dimensions. SEPs generated micro-ECoG potentials with spatially defined amplitude maps for each limb (figure 5.2). Localizing the activated region of cortex is usually the goal of sensory mapping. However, localization results calculated from SEPs cannot be readily compared to a known truth location to determine their accuracy. The location of the stimulus is known for optogenetic stimulation of the brain, so optogenetic micro-ECoG can be used to test localization algorithms. Localizing neural activity is an essential application of ECoG in patients with epilepsy.

7.3 Applications to neurological disorders

Micro-ECoG, optogenetics, and intracortical recordings would be a useful combination for studying epilepsy and neural excitability disorders in animal models. Epilepsy has many causes, but one unifying concept is the balance between excitation and inhibition. Optogenetics can bias both excitation and inhibition and micro-ECoG is perfectly positioned to record these effects. Multiple groups have attempted to use optogenetics to block seizures, and some have reported success [275–278]. These studies recorded epileptiform activity from a one or a small number of electrodes. Micro-ECoG could help provide additional spatial information to these studies, and the newly engineered chloride conducting Channelrhodopsins [279] could provide an order of magnitude larger chloride current, compared to halorhodopsin, to stop the most robust epileptic positive feedback neural activity. In addition to engineering neural interfaces to detect and block seizure-producing foci, these tools could be used to do basic research into the mechanisms of the disease. The excitability of the cortex could be assayed with optogenetics and micro-ECoG. This optogenetic excitability testing paradigm has been used to study stroke [280], and could be applied to study traumatic brain injury, cortical spreading depression, and mouse models of migraine [281]. These related disorders of excitatory/inhibitory balance also have a

significant neurovascular component that can be understood with the concept of the neurovascular unit [282].

7.4 Future of optogenetics and neurovascular coupling

Optical systems and optogenetics provide new tools to study the neurovascular unit, and one of its key functions, neurovascular coupling (chapter 2). Optogenetics will enable a cell type specific dissection of neurovascular coupling. Stimulating pyramidal neurons causes arterial dilation (figure 6.2), which is consistent with the logic that pyramidal neurons are primarily glutamatergic and therefore increase the activity and metabolism of the cortex. Exploring the hemodynamic response of specifically stimulating GABAergic neurons would be the next step. This optogenetic study would be additionally novel because the hemodynamic response to caged GABA does not appear to have been previously tested. Alternatively, inhibiting excitatory neurons optogenetically would be expected to have a similar effect as exciting inhibitory inter neurons, but the opsins available prior to April 2014 required strong and sustained green or yellow light excitation which would have caused confounding heating artifacts. The new bistable chloride Channelrhodopsin does not require sustained photoexcitation to block action potentials [279] and could enable neurovascular studies with specific neuron types to be silenced in a temporally and spatially defined manner.

Initial optogenetic spatial studies of neurovascular coupling suggest that the volume of cortical activation influences the size of major arteries (figure 6.2). Further spatial studies of neurovascular coupling and neurometabolic relationships could help determine distance to vessel relationships. Metabolic distance to vessel relationships are pronounced when imaging NADH in the cortex under mild hypoxia [283]. Similar distance to vessel studies can't be done with intrinsic optical signals due to hemoglobin, because hemoglobin is necessarily inside blood cells, in the vessel. Instead, regions between vessels could be stimulated optogenetically and hemodynamic changes could be measured. The amplitude of hemodynamic changes could be mapped onto the region of stimulation to create a spatial map, visualizing neurovascular coupling as a function of distance. The DMD system described in chapter

6 could be readily modified to do such a study. Studies with OCT would add spatial dimensions and velocity measurements, and perhaps a steerable laser would be a well paired spatial stimulation approach. Continued optical and optogenetic development increases the number of research opportunities.

7.5 Conclusion

Micro-ECoG can be understood in the context of more macroscopic signals and microscopic neurophysiological processes. The biophysics governing LFPs and ECoG holds for micro-ECoG and provides a frame work for conceptualizing optogenetic experiments of micro-ECoG (chapter 4) and the coherence between spikes and cortical potentials (chapter 3). Describing these relationships provides a basis for applying micro-ECoG as a chronic neural interface for BCI and basic research applications. Optogenetics and micro-ECoG, combined with *in vivo* imaging, form a platform to study neurovascular coupling and other fundamental neurophysiological functions.

References

[1] Moran D 2010 Evolution of brain–computer interface: action potentials, local field potentials and electrocorticograms *Current Opinion in Neurobiology* **20** 741–5

[2] Williams J C, Rennaker R L and Kipke D R 1999 Long-term neural recording characteristics of wire microelectrode arrays implanted in cerebral cortex *Brain Research Protocols* **4** 303–13

[3] Yizhar O, Fenno L E, Davidson T J, Mogri M and Deisseroth K 2011 Optogenetics in neural systems *Neuron* **71** 9–34

[4] Nagel G, Szellas T, Huhn W, Kateriya S, Adeishvili N, Berthold P, Ollig D, Hegemann P and Bamberg E 2003 Channelrhodopsin-2, a directly light-gated cation-selective membrane channel *Proceedings of the National Academy of Sciences* **100** 13940–5

[5] Boyden E S, Zhang F, Bamberg E, Nagel G and Deisseroth K 2005 Millisecond-timescale, genetically targeted optical control of neural activity *Nat Neurosci* **8** 1263–8

[6] Lee J H, Durand R, Gradinaru V, Zhang F, Goshen I, Kim D-S, Fenno L E, Ramakrishnan C and Deisseroth K 2010 Global and local fMRI signals driven by neurons defined optogenetically by type and wiring *Nature* **465** 788–92

[7] Kahn I, Knoblich U, Desai M, Bernstein J, Graybiel A M, Boyden E S, Buckner R L and Moore C I 2013 Optogenetic drive of neocortical pyramidal neurons generates fMRI signals that are correlated with spiking activity *Brain Research* **1511** 33–45

[8] Thanos P K, Robison L, Nestler E J, Kim R, Michaelides M, Lobo M-K and Volkow N D 2013 Mapping Brain Metabolic Connectivity in Awake Rats with μPET and Optogenetic Stimulation *J. Neurosci.* **33** 6343–9

[9] Pashaie R, Anikeeva P, Lee J H, Prakash R, Yizhar O, Prigge M, Chander D, Richner T and Williams J 2013 Optogenetic Brain Interfaces *Biomedical Engineering, IEEE Reviews in*

[10] Wang W, Degenhart A D, Collinger J L, Vinjamuri R, Sudre G P, Adelson P D, Holder D L, Leuthardt E C, Moran D W, Boninger M L, Schwartz A B, Crammond D J, Tyler-Kabara E C and Weber D J 2009 Human motor cortical activity recorded with Micro-ECoG electrodes, during individual finger movements *Annual International Conference of the IEEE Engineering in Medicine and Biology Society, 2009. EMBC 2009* Annual International Conference of the IEEE Engineering in Medicine and Biology Society, 2009. EMBC 2009 (IEEE) pp 586–9

[11] Kellis S, Miller K, Thomson K, Brown R, House P and Greger B 2010 Decoding spoken words using local field potentials recorded from the cortical surface *Journal of Neural Engineering* **7** 056007

[12] Penfield W and Rasmussen T 1950 *The cerebral cortex of man; a clinical study of localization of function* vol xv (Oxford, England: Macmillan)

[13] Penfield W and Jasper H 1954 Epilepsy and the functional anatomy of the human brain.

[14] Leuthardt E C, Schalk G, Wolpaw J R, Ojemann J G and Moran D W 2004 A brain–computer interface using electrocorticographic signals in humans *J. Neural Eng.* **1** 63–71

[15] Leuthardt E C, Miller K J, Schalk G, Rao R P N and Ojemann J G 2006 Electrocorticography-based brain computer Interface-the seattle experience *IEEE Transactions on Neural Systems and Rehabilitation Engineering* **14** 194–8

[16] Wilson J A, Felton E A, Garell P C, Schalk G and Williams J C 2006 ECoG factors underlying multimodal control of a brain-computer interface *Neural Systems and Rehabilitation Engineering, IEEE Transactions on* **14** 246–50

[17] Schalk G, Kubánek J, Miller K J, Anderson N R, Leuthardt E C, Ojemann J G, Limbrick D, Moran D, Gerhardt L A and Wolpaw J R 2007 Decoding two-dimensional movement trajectories using electrocorticographic signals in humans *Journal of Neural Engineering* **4** 264–75

[18] Schalk G, Miller K J, Anderson N R, Wilson J A, Smyth M D, Ojemann J G, Moran D W, Wolpaw J R and Leuthardt E C 2008 Two-dimensional movement control using electrocorticographic signals in humans *Journal of Neural Engineering* **5** 75–84

[19] Miller K J, Leuthardt E C, Schalk G, Rao R P N, Anderson N R, Moran D W, Miller J W and Ojemann J G 2007 Spectral Changes in Cortical Surface Potentials during Motor Movement *J. Neurosci.* **27** 2424–32

[20] Leuthardt E C, Miller K, Anderson N R, Schalk G, Dowling J, Miller J, Moran D W and Ojemann J G 2007 ELECTROCORTICOGRAPHIC FREQUENCY ALTERATION MAPPING *Neurosurgery* **60** 260???271

[21] Crone N E, Boatman D, Gordon B and Hao L 2001 Induced electrocorticographic gamma activity during auditory perception *Clinical Neurophysiology* **112** 565–82

[22] Edwards E, Soltani M, Deouell L Y, Berger M S and Knight R T 2005 High Gamma Activity in Response to Deviant Auditory Stimuli Recorded Directly From Human Cortex *Journal of Neurophysiology* **94** 4269 –4280

[23] Edwards E, Soltani M, Kim W, Dalal S S, Nagarajan S S, Berger M S and Knight R T 2009 Comparison of Time–Frequency Responses and the Event-Related Potential to Auditory Speech Stimuli in Human Cortex *Journal of Neurophysiology* **102** 377 –386

[24] Sinai A, Bowers C W, Crainiceanu C M, Boatman D, Gordon B, Lesser R P, Lenz F A and Crone N E 2005 Electrocorticographic high gamma activity versus electrical cortical stimulation mapping of naming *Brain* **128** 1556 –1570

[25] Edwards E, Nagarajan S S, Dalal S S, Canolty R T, Kirsch H E, Barbaro N M and Knight R T 2010 Spatiotemporal imaging of cortical activation during verb generation and picture naming *NeuroImage* **50** 291–301

[26] Kellis S, Miller K, Thomson K, Brown R, House P and Greger B 2010 Decoding spoken words using local field potentials recorded from the cortical surface *Journal of Neural Engineering* **7** 056007

[27] Takahashi H, Ejiri T, Nakao M, Nakamura N, Kaga K and Herve T 2003 Microelectrode array on folding polyimide ribbon for epidural mapping of functional evoked potentials *IEEE Trans. Biomed. Eng.* **50** 510–6

[28] Stieglitz T, Schuetter M and Koch K P 2005 Implantable biomedical microsystems for neural prostheses *Engineering in Medicine and Biology Magazine, IEEE* **24** 58–65

[29] Hollenberg B A, Richards C D, Richards R, Bahr D F and Rector D M 2006 A MEMS fabricated flexible electrode array for recording surface field potentials *J. Neurosci. Met.* **153** 147–53

[30] Molina-Luna K, Buitrago M M, Hertler B, Schubring M, Haiss F, Nisch W, Schulz J B and Luft A R 2007 Cortical stimulation mapping using epidurally implanted thin-film microelectrode arrays *J Neurosci Methods* **161** 118–25

[31] Hosp J A, Molina-Luna K, Hertler B, Atiemo C O, Stett A and Luft A R 2008 Thin-film epidural microelectrode arrays for somatosensory and motor cortex mapping in rat *Journal of Neuroscience Methods* **172** 255–62

[32] Thongpang S, Richner T J, Brodnick S K, Schendel A, Kim J, Wilson J, Hippensteel J, Krugner-Higby L, Moran D, Ahmed A S and Williams J 2011 A micro-electrocorticography platform and deployment strategies for chronic BCI applications. *Clin. EEG Neurosci.* **42** 259

[33] Viventi J, Kim D-H, Vigeland L, Frechette E S, Blanco J A, Kim Y-S, Avrin A E, Tiruvadi V R, Hwang S-W, Vanleer A C, Wulsin D F, Davis K, Gelber C E, Palmer L, Van der Spiegel J, Wu J, Xiao J, Huang Y, Contreras D, Rogers J A and Litt B 2011 Flexible, foldable, actively multiplexed, high-density electrode array for mapping brain activity in vivo *Nat Neurosci* **14** 1599–605

[34] Crone N, Miglioretti D, Gordon B and Lesser R 1998 Functional mapping of human sensorimotor cortex with electrocorticographic spectral analysis. II. Event-related synchronization in the gamma band *Brain* **121** 2301–15

[35] Pfurtscheller G and Aranibar A 1977 Event-related cortical desynchronization detected by power measurements of scalp EEG *Electroencephalography and Clinical Neurophysiology* **42** 817–26

[36] Pfurtscheller G and Lopes da Silva F H 1999 Event-related EEG/MEG synchronization and desynchronization: basic principles *Clinical Neurophysiology* **110** 1842–57

[37] Crone N E, Miglioretti D L, Gordon B, Sieracki J M, Wilson M T, Uematsu S and Lesser R P 1998 Functional mapping of human sensorimotor cortex with electrocorticographic spectral analysis. I. Alpha and beta event-related desynchronization. *Brain* **121** 2271 –2299

[38] Crone N E, Hao L, Hart J, Boatman D, Lesser R P, Irizarry R and Gordon B 2001 Electrocorticographic gamma activity during word production in spoken and sign language *Neurology* **57** 2045–53

[39] Crone N E, Boatman D, Gordon B and Hao L 2001 Induced electrocorticographic gamma activity during auditory perception *Clinical Neurophysiology* **112** 565–82

[40] Jacobs J and Kahana M J 2009 Neural Representations of Individual Stimuli in Humans Revealed by Gamma-Band Electrocorticographic Activity *J. Neurosci.* **29** 10203–14

[41] Aoki F, Fetz E E, Shupe L, Lettich E and Ojemann G A 1999 Increased gamma-range activity in human sensorimotor cortex during performance of visuomotor tasks *Clinical Neurophysiology* **110** 524–37

[42] Crone N E, Sinai A and Korzeniewska A 2006 High-frequency gamma oscillations and human brain mapping with electrocorticography *Progress in Brain Research* Event-Related Dynamics of Brain Oscillations vol Volume 159, ed Christa Neuper and Wolfgang Klimesch (Elsevier) pp 275–95

[43] Cheyne D, Bells S, Ferrari P, Gaetz W and Bostan A C 2008 Self-paced movements induce high-frequency gamma oscillations in primary motor cortex *NeuroImage* **42** 332–42

[44] Ray S, Crone N E, Niebur E, Franaszczuk P J and Hsiao S S 2008 Neural Correlates of High-Gamma Oscillations (60–200 Hz) in Macaque Local Field Potentials and Their Potential Implications in Electrocorticography *The Journal of Neuroscience* **28** 11526 –11536

[45] Logothetis N K, Pauls J, Augath M, Trinath T and Oeltermann A 2001 Neurophysiological investigation of the basis of the fMRI signal *Nature* **412** 150–7

[46] Mukamel R, Gelbard H, Arieli A, Hasson U, Fried I and Malach R 2005 Coupling Between Neuronal Firing, Field Potentials, and fMRI in Human Auditory Cortex *Science* **309** 951–4

[47] Niessing J, Ebisch B, Schmidt K E, Niessing M, Singer W and Galuske R A W 2005 Hemodynamic Signals Correlate Tightly with Synchronized Gamma Oscillations *Science* **309** 948–51

[48] Nir Y, Fisch L, Mukamel R, Gelbard-Sagiv H, Arieli A, Fried I and Malach R 2007 Coupling between Neuronal Firing Rate, Gamma LFP, and BOLD fMRI Is Related to Interneuronal Correlations *Current Biology* **17** 1275–85

[49] Adesnik H and Scanziani M 2010 Lateral competition for cortical space by layer-specific horizontal circuits *Nature* **464** 1155–60

[50] Yizhar O, Fenno L E, Prigge M, Schneider F, Davidson T J, O'Shea D J, Sohal V S, Goshen I, Finkelstein J, Paz J T and Deisseroth K 2011 Neocortical excitation/inhibition balance in information processing and social dysfunction *Nature*

[51] Sohal V S, Zhang F, Yizhar O and Deisseroth K 2009 Parvalbumin neurons and gamma rhythms enhance cortical circuit performance *Nature* **459** 698–702

[52] Canolty R T, Edwards E, Dalal S S, Soltani M, Nagarajan S S, Kirsch H E, Berger M S, Barbaro N M and Knight R T 2006 High Gamma Power Is Phase-Locked to Theta Oscillations in Human Neocortex *Science* **313** 1626–8

[53] Canolty R T and Knight R T 2010 The functional role of cross-frequency coupling *Trends in Cognitive Sciences* **14** 506–15

[54] Whittingstall K and Logothetis N K 2009 Frequency-Band Coupling in Surface EEG Reflects Spiking Activity in Monkey Visual Cortex *Neuron* **64** 281–9

[55] Mazzoni A, Whittingstall K, Brunel N, Logothetis N K and Panzeri S 2010 Understanding the relationships between spike rate and delta/gamma frequency bands of LFPs and EEGs using a local cortical network model *NeuroImage* **52** 956–72

[56] Miller K J, Hermes D, Honey C J, Sharma M, Rao R P N, den Nijs M, Fetz E E, Sejnowski T J, Hebb A O, Ojemann J G, Makeig S and Leuthardt E C 2010 Dynamic modulation of local population activity by rhythm phase in human occipital cortex during a visual search task *Front Hum Neurosci* **4** 197

[57] Buzsáki G, Anastassiou C A and Koch C 2012 The origin of extracellular fields and currents — EEG, ECoG, LFP and spikes *Nat Rev Neurosci* **13** 407–20

[58] Miller K J, Leuthardt E C, Schalk G, Rao R P N, Anderson N R, Moran D W, Miller J W and Ojemann J G 2007 Spectral Changes in Cortical Surface Potentials during Motor Movement *J. Neurosci.* **27** 2424–32

[59] Miller K J, Sorensen L B, Ojemann J G and den Nijs M 2009 Power-law scaling in the brain surface electric potential *PLoS Comput. Biol.* **5** e1000609

[60] Miller K J 2010 Broadband Spectral Change: Evidence for a Macroscale Correlate of Population Firing Rate? *J. Neurosci.* **30** 6477–9

[61] Miller K J, Honey C J, Hermes D, Rao R P, denNijs M and Ojemann J G 2014 Broadband changes in the cortical surface potential track activation of functionally diverse neuronal populations *NeuroImage* **85, Part 2** 711–20

[62] Van Winsun W, Sergeant J and Geuze R 1984 The functional significance of event-related desynchronization of alpha rhythm in attentional and activating tasks *Electroencephalography and Clinical Neurophysiology* **58** 519–24

[63] Dujardin K, Derambure P, Defebvre L, Bourriez J L, Jacquesson J M and Guieu J D 1993 Evaluation of event-related desynchronization (ERD) during a recognition task: effect of attention *Electroencephalography and Clinical Neurophysiology* **86** 353–6

[64] Klimesch W, Doppelmayr M, Russegger H, Pachinger T and Schwaiger J 1998 Induced alpha band power changes in the human EEG and attention *Neuroscience Letters* **244** 73–6

[65] Harris K D and Thiele A 2011 Cortical state and attention *Nat Rev Neurosci* **12** 509–23

[66] Klimesch W 1999 EEG alpha and theta oscillations reflect cognitive and memory performance: a review and analysis *Brain Research Reviews* **29** 169–95

[67] Krause C M, Heikki Lang A, Laine M, Kuusisto M and Pörn B 1996 Event-related. EEG desynchronization and synchronization during an auditory memory task *Electroencephalography and Clinical Neurophysiology* **98** 319–26

[68] Krause C M, Sillanmäki L, Koivisto M, Saarela C, Häggqvist A, Laine M and Hämäläinen H 2000 The effects of memory load on event-related EEG desynchronization and synchronization *Clinical Neurophysiology* **111** 2071–8

[69] Stipacek A, Grabner R H, Neuper C, Fink A and Neubauer A C 2003 Sensitivity of human EEG alpha band desynchronization to different working memory components and increasing levels of memory load *Neuroscience Letters* **353** 193–6

[70] Pfurtscheller G and Neuper C 1992 Simultaneous EEG 10 Hz desynchronization and 40 Hz synchronization during finger movements *Neuroreport* **3** 1057–60

[71] Toro C, Deuschl G, Thatcher R, Sato S, Kufta C and Hallett M 1994 Event-related desynchronization and movement-related cortical potentials on the ECoG and EEG *Electroencephalography and Clinical Neurophysiology/Evoked Potentials Section* **93** 380–9

[72] Leocani L, Toro C, Manganotti P, Zhuang P and Hallett M 1997 Event-related coherence and event-related desynchronization/synchronization in the 10 Hz and 20 Hz EEG during self-paced movements *Electroencephalography and Clinical Neurophysiology/Evoked Potentials Section* **104** 199–206

[73] Babiloni C, Carducci F, Cincotti F, Rossini P M, Neuper C, Pfurtscheller G and Babiloni F 1999 Human Movement-Related Potentials vs Desynchronization of EEG Alpha Rhythm: A High-Resolution EEG Study *NeuroImage* **10** 658–65

[74] Pfurtscheller G, Graimann B, Huggins J E, Levine S P and Schuh L A 2003 Spatiotemporal patterns of beta desynchronization and gamma synchronization in corticographic data during self-paced movement *Clinical Neurophysiology* **114** 1226–36

[75] Poulet J F A and Petersen C C H 2008 Internal brain state regulates membrane potential synchrony in barrel cortex of behaving mice *Nature* **454** 881–5

[76] Bekker A Y, Kaufman B, Samir H and Doyle W 2001 The use of dexmedetomidine infusion for awake craniotomy *Anesthesia & Analgesia* **92** 1251–3

[77] Cormack J, Orme R and Costello T 2005 The role of α2-agonists in neurosurgery *Journal of Clinical Neuroscience* **12** 375–8

[78] Souter M J, Rozet I, Ojemann J G, Souter K J, Holmes M D, Lee L and Lam A M 2007 Dexmedetomidine Sedation During Awake Craniotomy for Seizure Resection: Effects on Electrocorticography *Journal of Neurosurgical Anesthesiology* **19** 38–44

[79] Nelson L E, Lu J, Guo T, Saper C B, Franks N P and Maze M 2003 The α2-adrenoceptor agonist dexmedetomidine converges on an endogenous sleep-promoting pathway to exert its sedative effects *Anesthesiology* **98** 428–36

[80] Oda Y, Toriyama S, Tanaka K, Matsuura T, Hamaoka N, Morino M and Asada A 2007 The Effect of Dexmedetomidine on Electrocorticography in Patients with Temporal Lobe Epilepsy Under Sevoflurane Anesthesia *Anesthesia & Analgesia* **105** 1272 –1277

[81] Nunez P L and Srinivasan R 2006 *Electric Fields of the Brain: The Neurophysics of EEG* (Oxford University Press)

[82] Malmivuo J and Plonsey R 1995 *Bioelectromagnetism: Principles and Applications of Bioelectric and Biomagnetic Fields* (Oxford University Press)

[83] Slutzky M W, Jordan L R, Krieg T, Chen M, Mogul D J and Miller L E 2010 Optimal spacing of surface electrode arrays for brain–machine interface applications *J. Neural Eng.* **7** 026004

[84] Bundy D T, Zellmer E, Gaona C M, Sharma M, Szrama N, Hacker C, Freudenburg Z V, Daitch A, Moran D W and Leuthardt E C 2014 Characterization of the effects of the human dura on macro- and micro-electrocorticographic recordings *J. Neural Eng.* **11** 016006

[85] Wodlinger B, Degenhart A D, Collinger J L, Tyler-Kabara E C and Wang W 2011 The impact of electrode characteristics on electrocorticography (ECoG) *2011 Annual International Conference of the IEEE Engineering in Medicine and Biology Society,EMBC* 2011 Annual International Conference of the IEEE Engineering in Medicine and Biology Society,EMBC pp 3083–6

[86] Rosen G, La Porte N, Diechtiareff B, Pung C, Nissanov J, Gustafson C, Bertrand L, Gefen S, Fan Y, Tretiak O, Manly K, Park M, Williams A, Connolly M, Capra J and Williams R 2003 Informatics center for mouse genomics *Neuroinformatics* **1** 327–42

[87] Granger C W J 1969 Investigating Causal Relations by Econometric Models and Cross-spectral Methods *Econometrica* **37** 424–38

[88] Gray C M and Singer W 1989 Stimulus-specific neuronal oscillations in orientation columns of cat visual cortex *Proceedings of the National Academy of Sciences of the United States of America* **86** 1698–702

[89] Silva L, Amitai Y and Connors B 1991 Intrinsic oscillations of neocortex generated by layer 5 pyramidal neurons *Science* **251** 432–5

[90] Murthy V N and Fetz E E 1992 Coherent 25- to 35-Hz oscillations in the sensorimotor cortex of awake behaving monkeys *Proceedings of the National Academy of Sciences of the United States of America* **89** 5670 –5674

[91] Donoghue J P, Sanes J N, Hatsopoulos N G and Gaal G 1998 Neural Discharge and Local Field Potential Oscillations in Primate Motor Cortex During Voluntary Movements *J Neurophysiol* **79** 159–73

[92] Pesaran B, Pezaris J S, Sahani M, Mitra P P and Andersen R A 2002 Temporal structure in neuronal activity during working memory in macaque parietal cortex *Nat Neurosci* **5** 805–11

[93] Scherberger H, Jarvis M and Andersen R 2005 Cortical Local Field Potential Encodes Movement Intentions in the Posterior Parietal Cortex *Neuron* **46** 347–54

[94] Montemurro M A, Rasch M J, Murayama Y, Logothetis N K and Panzeri S 2008 Phase-of-Firing Coding of Natural Visual Stimuli in Primary Visual Cortex *Current Biology* **18** 375–80

[95] Rasch M J, Gretton A, Murayama Y, Maass W and Logothetis N K 2008 Inferring Spike Trains From Local Field Potentials *J Neurophysiol* **99** 1461–76

[96] Mollazadeh M, Aggarwal V, Thakor N V, Law A J, Davidson A and Schieber M H 2009 Coherency between spike and LFP activity in M1 during hand movements *Neural Engineering, 2009. NER '09. 4th International IEEE/EMBS Conference on* Neural Engineering, 2009. NER '09. 4th International IEEE/EMBS Conference on pp 506–9

[97] Denker M, Roux S, Lindén H, Diesmann M, Riehle A and Grün S 2011 The Local Field Potential Reflects Surplus Spike Synchrony *Cerebral Cortex* **21** 2681–95

[98] Csicsvari J, Jamieson B, Wise K D and Buzsáki G 2003 Mechanisms of Gamma Oscillations in the Hippocampus of the Behaving Rat *Neuron* **37** 311–22

[99] Fries P, Nikolic D and Singer W 2007 The gamma cycle *Trends in Neurosciences* **30** 309–16

[100] Lindén H, Tetzlaff T, Potjans T C, Pettersen K H, Grün S, Diesmann M and Einevoll G T 2011 Modeling the Spatial Reach of the LFP *Neuron* **72** 859–72

[101] Mitzdorf U 1985 Current source-density method and application in cat cerebral cortex: investigation of evoked potentials and EEG phenomena *Physiological Reviews* **65** 37–100

[102] Nagel G, Brauner M, Liewald J F, Adeishvili N, Bamberg E and Gottschalk A 2005 Light Activation of Channelrhodopsin-2 in Excitable Cells of Caenorhabditis elegans Triggers Rapid Behavioral Responses *Current Biology* **15** 2279–84

[103] Levasseur J E, Wei E P, Raper A J, Kontos A A and Patterson J L 1975 Detailed description of a cranial window technique for acute and chronic experiments *Stroke* **6** 308–17

[104] Morii S, Ngai A C and Winn H R 1986 Reactivity of Rat Pial Arterioles and Venules to Adenosine and Carbon Dioxide: With Detailed Description of the Closed Cranial Window Technique in Rats *J. Cerebr. Blood F. Met.* **6** 34–41

[105] Kawamura S, Schürer L, Goetz A, Kempski O, Schmucker B and Baethmann A 1990 An improved closed cranial window technique for investigation of blood-brain barrier function and cerebral vasomotor control in the rat *Int J Microcirc Clin Exp* **9** 369–83

[106] Mayhan W 1991 Disruption of the blood-brain barrier in open and closed cranial window preparations in rats *Stroke* **22** 1059–63

[107] Yoder E J, Kleinfeld D and others 2002 Cortical imaging through the intact mouse skull using two-photon excitation laser scanning microscopy *Microsc. Res. Techniq.* **56** 304–5

[108] Grutzendler J, Kasthuri N and Gan W-B 2002 Long-term dendritic spine stability in the adult cortex *Nature* **420** 812–6

[109] Zuo Y, Lin A, Chang P and Gan W-B 2005 Development of Long-Term Dendritic Spine Stability in Diverse Regions of Cerebral Cortex *Neuron* **46** 181–9

[110] Drew P J, Shih A Y, Driscoll J D, Knutsen P M, Blinder P, Davalos D, Akassoglou K, Tsai P S and Kleinfeld D 2010 Chronic optical access through a polished and reinforced thinned skull *Nature Methods* **7** 981–4

[111] Trachtenberg J T, Chen B E, Knott G W, Feng G, Sanes J R, Welker E and Svoboda K 2002 Long-term in vivo imaging of experience-dependent synaptic plasticity in adult cortex *Nature* **420** 788–94

[112] Schendel A A, Thongpang S, Brodnick S K, Richner T J, Lindevig B D B, Krugner-Higby L and Williams J C 2013 A cranial window imaging method for monitoring vascular growth around chronically implanted micro-ECoG devices *Journal of Neuroscience Methods* **218** 121–30

[113] Xu H-T, Pan F, Yang G and Gan W-B 2007 Choice of cranial window type for in vivo imaging affects dendritic spine turnover in the cortex *Nature Neuroscience* **10** 549–51

[114] Holtmaat A J G D, Trachtenberg J T, Wilbrecht L, Shepherd G M, Zhang X, Knott G W and Svoboda K 2005 Transient and Persistent Dendritic Spines in the Neocortex In Vivo *Neuron* **45** 279–91

[115] Zuo Y, Yang G, Kwon E and Gan W-B 2005 Long-term sensory deprivation prevents dendritic spine loss in primary somatosensory cortex *Nature* **436** 261–5

[116] Holtmaat A, Wilbrecht L, Knott G W, Welker E and Svoboda K 2006 Experience-dependent and cell-type-specific spine growth in the neocortex *Nature* **441** 979–83

[117] Ogawa S, Lee T M, Kay A R and Tank D W 1990 Brain magnetic resonance imaging with contrast dependent on blood oxygenation *PNAS* **87** 9868–72

[118] Helmchen F and Denk W 2005 Deep tissue two-photon microscopy *Nat Meth* **2** 932–40

[119] Kleinfeld D, Mitra P P, Helmchen F and Denk W 1998 Fluctuations and stimulus-induced changes in blood flow observed in individual capillaries in layers 2 through 4 of rat neocortex *PNAS* **95** 15741–6

[120] Kleinfeld D and Denk W 2000 Two-photon Imaging of Neocortical Microcirculation *Imaging neurons: a laboratory manual*

[121] Mohanty S K, Reinscheid R K, Liu X, Okamura N, Krasieva T B and Berns M W 2008 In-Depth Activation of Channelrhodopsin 2-Sensitized Excitable Cells with High Spatial Resolution Using Two-Photon Excitation with a Near-Infrared Laser Microbeam *Biophysical Journal* **95** 3916–26

[122] Rickgauer J P and Tank D W 2009 Two-photon excitation of channelrhodopsin-2 at saturation *PNAS* **106** 15025–30

[123] Papagiakoumou E, Anselmi F, Bègue A, de Sars V, Glückstad J, Isacoff E Y and Emiliani V 2010 Scanless two-photon excitation of channelrhodopsin-2 *Nat Meth* **7** 848–54

[124] Prakash R, Yizhar O, Grewe B, Ramakrishnan C, Wang N, Goshen I, Packer A M, Peterka D S, Yuste R, Schnitzer M J and Deisseroth K 2012 Two-photon optogenetic toolbox for fast inhibition, excitation and bistable modulation *Nat Meth* **9** 1171–9

[125] Andrasfalvy B K, Zemelman B V, Tang J and Vaziri A 2010 Two-photon single-cell optogenetic control of neuronal activity by sculpted light *PNAS* **107** 11981–6

[126] Packer A M, Peterka D S, Hirtz J J, Prakash R, Deisseroth K and Yuste R 2012 Two-photon optogenetics of dendritic spines and neural circuits *Nat Meth* **9** 1202–5

[127] Fercher A F and Briers J D 1981 Flow visualization by means of single-exposure speckle photography *Optics Communications* **37** 326–30

[128] Dunn A K, Bolay H, Moskowitz M A and Boas D A 2001 Dynamic Imaging of Cerebral Blood Flow Using Laser Speckle *J Cereb Blood Flow Metab* **21** 195–201

[129] Li N, Pelled G, Gilad A A, Walczak P and Thakor N V 2011 An in vivo optical system: Control and monitor cortical activity with improved laser speckle contrast imaging and optogenetics *2011 5th International IEEE/EMBS Conference on Neural Engineering (NER)* 2011 5th International IEEE/EMBS Conference on Neural Engineering (NER) pp 76–9

[130] Li N 2012 *Functional brain imaging and optogenetic manipulations for the study of plasticity* Ph.D. (United States -- Maryland: The Johns Hopkins University)

[131] Li N, Thakor N V and Pelled G 2013 Laser speckle contrast reveals cerebral blood flow dynamics evoked by optogenetically controlled neuronal activity vol 8586 p 85860F–85860F–7

[132] Miao P, Lu H, Liu Q, Li Y and Tong S 2011 Laser speckle contrast imaging of cerebral blood flow in freely moving animals *J. Biomed. Opt* **16** 090502–090502–3

[133] Scott N A 2011 Optical probing of hemodynamic responses in vivo with channelrhodopsin-2

[134] Scott N A and Murphy T H 2012 Hemodynamic Responses Evoked by Neuronal Stimulation via Channelrhodopsin-2 Can Be Independent of Intracortical Glutamatergic Synaptic Transmission *PLoS ONE* **7** e29859

[135] Xie Y, Chen S, Anenberg E and Murphy T H 2013 Resistance of optogenetically evoked motor function to global ischemia and reperfusion in mouse in vivo *J Cereb Blood Flow Metab* **33** 1148–52

[136] Grinvald A, Lieke E, Frostig R D, Gilbert C D and Wiesel T N 1986 Functional architecture of cortex revealed by optical imaging of intrinsic signals *Nature* **324** 361–4

[137] Frostig R D, Lieke E E, Ts'o D Y and Grinvald A 1990 Cortical functional architecture and local coupling between neuronal activity and the microcirculation revealed by in vivo high-resolution optical imaging of intrinsic signals. *PNAS* **87** 6082–6

[138] Ayling O G S, Harrison T C, Boyd J D, Goroshkov A and Murphy T H 2009 Automated light-based mapping of motor cortex by photoactivation of channelrhodopsin-2 transgenic mice *Nat. Meth.* **6** 219–24

[139] Ji L, Zhou J, Zafar R, Kantorovich S, Jiang R, Carney P R and Jiang H 2012 Cortical Neurovascular Coupling Driven by Stimulation of Channelrhodopsin-2 *PLoS ONE* **7** e46607

[140] Pisauro M A, Dhruv N T, Carandini M and Benucci A 2013 Fast Hemodynamic Responses in the Visual Cortex of the Awake Mouse *J. Neurosci.* **33** 18343–51

[141] Fujimoto J G, Pitris C, Boppart S A and Brezinski M E 2000 Optical Coherence Tomography: An Emerging Technology for Biomedical Imaging and Optical Biopsy *Neoplasia* **2** 9–25

[142] Schmitt J M 1999 Optical coherence tomography (OCT): a review *IEEE Journal of Selected Topics in Quantum Electronics* **5** 1205–15

[143] Fercher A F, Hitzenberger C K, Kamp G and El-Zaiat S Y 1995 Measurement of intraocular distances by backscattering spectral interferometry *Optics Communications* **117** 43–8

[144] Ha¨usler G and Lindner M W 1998 “Coherence Radar” and “Spectral Radar”—New Tools for Dermatological Diagnosis *J. Biomed. Opt* **3** 21–31

[145] White B, Pierce M, Nassif N, Cense B, Park B, Tearney G, Bouma B, Chen T and de Boer J 2003 In vivo dynamic human retinal blood flow imaging using ultra-high-speed spectral domain optical coherence tomography *Opt. Express* **11** 3490–7

[146] Choudhury N, Zhang Z, Zhao F, Gu L and Mohanty S 2012 Label free optical detection of optogenetic activation of cells using phase-sensitive Fourier domain optical coherence tomography *Visualization, Image Processing and Computation in Biomedicine*

[147] Buxton R B, Wong E C and Frank L R 1998 Dynamics of blood flow and oxygenation changes during brain activation: The balloon model *Magn. Reson. Med.* **39** 855–64

[148] Glover G H 1999 Deconvolution of Impulse Response in Event-Related BOLD fMRI *NeuroImage* **9** 416–29

[149] Lee S-P, Duong T Q, Yang G, Iadecola C and Kim S-G 2001 Relative changes of cerebral arterial and venous blood volumes during increased cerebral blood flow: Implications for BOLD fMRI *Magn. Reson. Med.* **45** 791–800

[150] Christie I N, Wells J A, Southern P, Marina N, Kasparov S, Gourine A V and Lythgoe M F 2013 fMRI response to blue light delivery in the naïve brain: Implications for combined optogenetic fMRI studies *NeuroImage* **66** 634–41

[151] Aravanis A M, Wang L-P, Zhang F, Meltzer L A, Mogri M Z, Schneider M B and Deisseroth K 2007 An optical neural interface: in vivo control of rodent motor cortex with integrated fiberoptic and optogenetic technology *J. Neural Eng.* **4** S143–S156

[152] Zorzos A N, Scholvin J, Boyden E S and Fonstad C G 2012 Three-dimensional multiwaveguide probe array for light delivery to distributed brain circuits *Opt. Lett.* **37** 4841–3

[153] Guo Z V, Hart A C and Ramanathan S 2009 Optical interrogation of neural circuits in Caenorhabditis elegans *Nat Meth* **6** 891–6

[154] Stirman J N, Brauner M, Gottschalk A and Lu H 2010 High-throughput study of synaptic transmission at the neuromuscular junction enabled by optogenetics and microfluidics *Journal of Neuroscience Methods* **191** 90–3

[155] Leifer A M, Fang-Yen C, Gershow M, Alkema M J and Samuel A D T 2011 Optogenetic manipulation of neural activity in freely moving Caenorhabditis elegans *Nat Meth* **8** 147–52

[156] Stirman J N, Crane M M, Husson S J, Gottschalk A and Lu H 2012 A multispectral optical illumination system with precise spatiotemporal control for the manipulation of optogenetic reagents *Nat. Protocols* **7** 207–20

[157] Jerome J, Foehring R C, Armstrong W E, Spain W and Heck D H 2011 Parallel optical control of spatiotemporal neuronal spike activity using high-speed digital light processing *Front. Syst. Neurosci.* **5** 70

[158] Sakai S, Ueno K, Ishizuka T and Yawo H 2013 Parallel and patterned optogenetic manipulation of neurons in the brain slice using a DMD-based projector *Neuroscience Research* **75** 59–64

[159] Tsuda S, Kee M Z L, Cunha C, Kim J, Yan P, Loew L M and Augustine G J 2013 Probing the function of neuronal populations: Combining micromirror-based optogenetic photostimulation with voltage-sensitive dye imaging *Neuroscience Research* **75** 76–81

[160] Zahid M, Vélez-Fort M, Papagiakoumou E, Ventalon C, Angulo M C and Emiliani V 2010 Holographic Photolysis for Multiple Cell Stimulation in Mouse Hippocampal Slices *PLoS ONE* **5** e9431

[161] Yang S, Papagiakoumou E, Guillon M, Sars V de, Tang C-M and Emiliani V 2011 Three-dimensional holographic photostimulation of the dendritic arbor *J. Neural Eng.* **8** 046002

[162] Reutsky-Gefen I, Golan L, Farah N, Schejter A, Tsur L, Brosh I and Shoham S 2013 Holographic optogenetic stimulation of patterned neuronal activity for vision restoration *Nature communications* **4** 1509

[163] Chance B, Cohen P, Jobsis F and Schoener B 1962 Intracellular Oxidation-Reduction States in Vivo The microfluorometry of pyridine nucleotide gives a continuous measurement of the oxidation state *Science* **137** 499–508

[164] Ji S, Chance B, Stuart B H and Nathan R 1977 Two-dimensional analysis of the redox state of the rat cerebral cortex in vivo by NADH fluorescence photography *Brain Research* **119** 357–73

[165] Frostig R D, Lieke E E, Ts'o D Y and Grinvald A 1990 Cortical functional architecture and local coupling between neuronal activity and the microcirculation revealed by in vivo high-resolution optical imaging of intrinsic signals. *PNAS* **87** 6082–6

[166] Ince C, Coremans J M C C and Bruining H A 1992 In Vivo NADH Fluorescence *Oxygen Transport to Tissue XIV* Advances in Experimental Medicine and Biology ed W Erdmann and D F Bruley (Springer US) pp 277–96

[167] Levine S P, Huggins J E, BeMent S L, Kushwaha R K, Schuh L A, Rohde M M, Passaro E A, Ross D A, Elisevich K V and Smith B J 2000 A direct brain interface based on event-related potentials *IEEE Transactions on Rehabilitation Engineering* **8** 180–5

[168] Stieglitz T 2001 Flexible biomedical microdevices with double-sided electrode arrangements for neural applications *Sensors and Actuators A: Physical* **90** 203–11

[169] Rubehn B, Bosman C, Oostenveld R, Fries P and Stieglitz T 2009 A MEMS-based flexible multichannel ECoG-electrode array *J. Neural Eng.* **6** 036003

[170] Stieglitz T, Kammer S, Koch K P, Wien S and Robitzki A 2002 Encapsulation of flexible biomedical microimplants with parylene C *IFESS 2002* **5**

[171] Rubehn B, Fries P and Stieglitz T 2009 MEMS-Technology for Large-Scale, Multichannel ECoG-Electrode Array Manufacturing *4th European Conference of the International Federation for Medical and Biological Engineering* pp 2413–6

[172] Hochberg L R, Serruya M D, Friehs G M, Mukand J A, Saleh M, Caplan A H, Branner A, Chen D, Penn R D and Donoghue J P 2006 Neuronal ensemble control of prosthetic devices by a human with tetraplegia *Nature* **442** 164–71

[173] Szarowski D H, Andersen M D, Retterer S, Spence A J, Isaacson M, Craighead H G, Turner J N and Shain W 2003 Brain responses to micro-machined silicon devices *Brain Research* **983** 23–35

[174] Barrese J C, Rao N, Paroo K, Triebwasser C, Vargas-Irwin C, Franquemont L and Donoghue J P 2013 Failure mode analysis of silicon-based intracortical microelectrode arrays in non-human primates *J. Neural Eng.* **10** 066014

[175] Saxena T, Karumbaiah L, Gaupp E A, Patkar R, Patil K, Betancur M, Stanley G B and Bellamkonda R V 2013 The impact of chronic blood–brain barrier breach on intracortical electrode function *Biomaterials* **34** 4703–13

[176] Miller K J, Zanos S, Fetz E E, Nijs M den and Ojemann J G 2009 Decoupling the Cortical Power Spectrum Reveals Real-Time Representation of Individual Finger Movements in Humans *J. Neurosci.* **29** 3132–7

[177] Miller K J 2010 Broadband Spectral Change: Evidence for a Macroscale Correlate of Population Firing Rate? *J. Neurosci.* **30** 6477–9

[178] Yazdan-Shahmorad A, Kipke D R and Lehmkuhle M J 2013 High gamma power in ECoG reflects cortical electrical stimulation effects on unit activity in layers V/VI *J. Neural Eng.* **10** 066002

[179] Manning J R, Jacobs J, Fried I and Kahana M J 2009 Broadband Shifts in Local Field Potential Power Spectra Are Correlated with Single-Neuron Spiking in Humans *J. Neurosci.* **29** 13613–20

[180] Radman T, Su Y, An J H, Parra L C and Bikson M 2007 Spike Timing Amplifies the Effect of Electric Fields on Neurons: Implications for Endogenous Field Effects *J. Neurosci.* **27** 3030–6

[181] Mitra P and Bokil H 2008 *Observed brain dynamics* (New York, New York, USA: Oxford University Press, New York, New York, USA)

[182] DeCoteau W E, Thorn C, Gibson D J, Courtemanche R, Mitra P, Kubota Y and Graybiel A M 2007 Oscillations of Local Field Potentials in the Rat Dorsal Striatum During Spontaneous and Instructed Behaviors *J Neurophysiol* **97** 3800–5

[183] DeCoteau W E, Thorn C, Gibson D J, Courtemanche R, Mitra P, Kubota Y and Graybiel A M 2007 Learning-related coordination of striatal and hippocampal theta rhythms during acquisition of a procedural maze task *Proceedings of the National Academy of Sciences* **104** 5644–9

[184] Ray S, Hsiao S S, Crone N E, Franaszczuk P J and Niebur E 2008 Effect of stimulus intensity on spike-LFP relationship in Secondary Somatosensory cortex *J Neurosci* **28** 7334–43

[185] Buzsaki G, Kennedy B, Solt V B and Ziegler M 1991 Noradrenergic Control of Thalamic Oscillation: the Role of alpha-2 Receptors *Eur J Neurosci* **3** 222–9

[186] Belitski A, Gretton A, Magri C, Murayama Y, Montemurro M A, Logothetis N K and Panzeri S 2008 Low-Frequency Local Field Potentials and Spikes in Primary Visual Cortex Convey Independent Visual Information *J. Neurosci.* **28** 5696–709

[187] Kayser C, Montemurro M A, Logothetis N K and Panzeri S 2009 Spike-Phase Coding Boosts and Stabilizes Information Carried by Spatial and Temporal Spike Patterns *Neuron* **61** 597–608

[188] Ludwig K A, Miriani R M, Langhals N B, Joseph M D, Anderson D J and Kipke D R 2009 Using a Common Average Reference to Improve Cortical Neuron Recordings From Microelectrode Arrays *Journal of Neurophysiology* **101** 1679 –1689

[189] Quiroga R Q, Nadasdy Z and Ben-Shaul Y 2004 Unsupervised spike detection and sorting with wavelets and superparamagnetic clustering *Neural Comput.* **16** 1661–87

[190] Harris K D, Henze D A, Csicsvari J, Hirase H and Buzsáki G 2000 Accuracy of Tetrode Spike Separation as Determined by Simultaneous Intracellular and Extracellular Measurements *Journal of Neurophysiology* **84** 401 –414

[191] Richner T J, Thongpang S, Brodnick S K, Schendel A A, Falk R W, Krugner-Higby L A, Pashaie R and Williams J C 2014 Optogenetic micro-electrocorticography for modulating and localizing cerebral cortex activity *J. Neural Eng.* **11** 016010

[192] Rouse A G, Williams J J, Wheeler J J and Moran D W 2013 Cortical Adaptation to a Chronic Micro-Electrocorticographic Brain Computer Interface *J. Neurosci.* **33** 1326–30

[193] Otto K J, Rousche P J and Kipke D R 2005 Microstimulation in auditory cortex provides a substrate for detailed behaviors *Hearing Research* **210** 112–7

[194] Venkatraman S, Elkabany K, Long J D, Yao Y and Carmena J M 2009 A System for Neural Recording and Closed-Loop Intracortical Microstimulation in Awake Rodents *IEEE Transactions on Biomedical Engineering* **56** 15–22

[195] Boyden E S, Zhang F, Bamberg E, Nagel G and Deisseroth K 2005 Millisecond-timescale, genetically targeted optical control of neural activity *Nat. Neurosci.* **8** 1263–8

[196] Zhang F, Wang L-P, Brauner M, Liewald J F, Kay K, Watzke N, Wood P G, Bamberg E, Nagel G, Gottschalk A and Deisseroth K 2007 Multimodal fast optical interrogation of neural circuitry *Nature* **446** 633–9

[197] Chow B Y, Han X, Dobry A S, Qian X, Chuong A S, Li M, Henninger M A, Belfort G M, Lin Y, Monahan P E and Boyden E S 2010 High-performance genetically targetable optical neural silencing by light-driven proton pumps *Nature* **463** 98–102

[198] Gradinaru V, Thompson K R, Zhang F, Mogri M, Kay K, Schneider M B and Deisseroth K 2007 Targeting and Readout Strategies for Fast Optical Neural Control In Vitro and In Vivo *J. Neurosci.* **27** 14231 –14238

[199] Royer S, Zemelman B V, Barbic M, Losonczy A, Buzsáki G and Magee J C 2010 Multi-array silicon probes with integrated optical fibers: light-assisted perturbation and recording of local neural circuits in the behaving animal *European J. Neurosci.* **31** 2279–91

[200] Anikeeva P, Andalman A S, Witten I, Warden M, Goshen I, Grosenick L, Gunaydin L A, Frank L M and Deisseroth K 2012 Optetrode: a multichannel readout for optogenetic control in freely moving mice *Nat. Neurosci.* **15** 163–70

[201] Wang J, Wagner F, Borton D A, Zhang J, Ozden I, Burwell R D, Nurmikko A V, van Wagenen R, Diester I and Deisseroth K 2012 Integrated device for combined optical neuromodulation and electrical recording for chronic in vivo applications *J. Neural Eng.* **9** 016001

[202] Cardin J A, Carlén M, Meletis K, Knoblich U, Zhang F, Deisseroth K, Tsai L-H and Moore C I 2010 Targeted optogenetic stimulation and recording of neurons in vivo using cell-type-specific expression of Channelrhodopsin-2 *Nat. Protocols* **5** 247–54

[203] Khurram A and Seymour J P 2013 Investigation of the photoelectrochemical effect in optoelectrodes and potential uses for implantable electrode characterization* *2013 35th Annual International Conference of the IEEE Engineering in Medicine and Biology Society (EMBC)* 2013 35th Annual International Conference of the IEEE Engineering in Medicine and Biology Society (EMBC) pp 3032–5

[204] Kwon K and Li W 2013 Integrated multi-LED array with three-dimensional polymer waveguide for optogenetics 2013 IEEE 26th International Conference on Micro Electro Mechanical Systems (MEMS) pp 1017–20

[205] Henry S. Forbes 1928 The cerebral circulation: I. observation and measurement of pial vessels *Arch. Neurol. Psy.* **19** 751–61

[206] Holtmaat A, Bonhoeffer T, Chow D K, Chuckowree J, Paola V D, Hofer S B, Hübener M, Keck T, Knott G, Lee W-C A, Mostany R, Mrsic-Flogel T D, Nedivi E, Portera-Cailliau C, Svoboda K, Trachtenberg J T and Wilbrecht L 2009 Long-term, high-resolution imaging in the mouse neocortex through a chronic cranial window *Nature Protocols* **4** 1128–44

[207] Drew P J, Shih A Y, Driscoll J D, Knutsen P M, Blinder P, Davalos D, Akassoglou K, Tsai P S and Kleinfeld D 2010 Chronic optical access through a polished and reinforced thinned skull *Nat. Meth.* **7** 981–4

[208] Aravanis A M, Wang L-P, Zhang F, Meltzer L A, Mogri M Z, Schneider M B and Deisseroth K 2007 An optical neural interface: in vivo control of rodent motor cortex with integrated fiberoptic and optogenetic technology *Journal of Neural Engineering* **4** S143–S156

[209] Yuen T G H, Agnew W F and Bullara L A 1987 Tissue response to potential neuroprosthetic materials implanted subdurally *Biomaterials* **8** 138–41

[210] Loeb G E, Bak M J, Salcman M and Schmidt E M 1977 Parylene as a Chronically Stable, Reproducible Microelectrode Insulator *IEEE Trans. Biomed. Eng.* **BME-24** 121 –128

[211] Schmidt E M, Mcintosh J S and Bak M J 1988 Long-term implants of Parylene-C coated microelectrodes *Med. Biol. Eng. Comput.* **26** 96–101

[212] Rodger D C, Fong A J, Li W, Ameri H, Ahuja A K, Gutierrez C, Lavrov I, Zhong H, Menon P R, Meng E, Burdick J W, Roy R R, Edgerton V R, Weiland J D, Humayun M S and Tai Y-C 2008 Flexible parylene-based multielectrode array technology for high-density neural stimulation and recording *Sensor Actuat B-Chem* **132** 449–60

[213] Ledochowitsch P, Olivero E, Blanche T and Maharbiz M M 2011 A transparent μECoG array for simultaneous recording and optogenetic stimulation 2011 Annual International Conference of the IEEE Engineering in Medicine and Biology Society,EMBC (IEEE) pp 2937–40

[214] Wilks S J, Richner T J, Brodnick S K, Kipke D R, Williams J C and Otto K J 2012 Voltage Biasing, Cyclic Voltammetry, & Electrical Impedance Spectroscopy for Neural Interfaces *J. Vis. Exp.*

[215] Arenkiel B R, Peca J, Davison I G, Feliciano C, Deisseroth K, Augustine G J, Ehlers M D and Feng G 2007 In Vivo Light-Induced Activation of Neural Circuitry in Transgenic Mice Expressing Channelrhodopsin-2 *Neuron* **54** 205–18

[216] Zhao S, Ting J T, Atallah H E, Qiu L, Tan J, Gloss B, Augustine G J, Deisseroth K, Luo M, Graybiel A M and Feng G 2011 Cell type-specific channelrhodopsin-2 transgenic mice for optogenetic dissection of neural circuitry function *Nat. Meth.* **8** 745–52

[217] Nagel G, Brauner M, Liewald J F, Adeishvili N, Bamberg E and Gottschalk A 2005 Light Activation of Channelrhodopsin-2 in Excitable Cells of Caenorhabditis elegans Triggers Rapid Behavioral Responses *Curr. Biol.* **15** 2279–84

[218] Lin J Y, Lin M Z, Steinbach P and Tsien R Y 2009 Characterization of Engineered Channelrhodopsin Variants with Improved Properties and Kinetics *Biophys. J.* **96** 1803–14

[219] Mattis J, Tye K M, Ferenczi E A, Ramakrishnan C, O'Shea D J, Prakash R, Gunaydin L A, Hyun M, Fenno L E, Gradinaru V, Yizhar O and Deisseroth K 2012 Principles for applying optogenetic tools derived from direct comparative analysis of microbial opsins *Nat. Meth.* **9** 159–72

[220] LEVASSEUR J E, WEI E P, RAPER A J, KONTOS H A and PATTERSON J L 1975 Detailed Description of a Cranial Window Technique for Acute and Chronic Experiments *Stroke* **6** 308–17

[221] Mostany R and Portera-Cailliau C 2008 A Craniotomy Surgery Procedure for Chronic Brain Imaging *J. Vis. Exp.*

[222] Yoder E J and Kleinfeld D 2002 Cortical imaging through the intact mouse skull using two-photon excitation laser scanning microscopy *Microsc. Res. Techniq.* **56** 304–5

[223] Pashaie R and Falk R 2013 Single Optical Fiber Probe for Fluorescence Detection and Optogenetic Stimulation *IEEE Trans. Biomed. Eng.* **60** 268 –280

[224] Stieglitz T, Beutel H and Meyer J U 1997 A flexible, light-weight multichannel sieve electrode with integrated cables for interfacing regenerating peripheral nerves *Sensor Actuat. A-Phys.* **60** 240–3

[225] Grumet A E, Wyatt Jr. J L and Rizzo III J F 2000 Multi-electrode stimulation and recording in the isolated retina *Journal of Neuroscience Methods* **101** 31–42

[226] Rousche P J, Pellinen D S, Pivin D P, Williams J C, Vetter R J and Kipke D R 2001 Flexible polyimide-based intracortical electrode arrays with bioactive capability *IEEE Trans. Biomed. Eng.* **48** 361–71

[227] Van Veen B D, Van Drongelen W, Yuchtman M and Suzuki A 1997 Localization of brain electrical activity via linearly constrained minimum variance spatial filtering *IEEE Trans. Biomed. Eng.* **44** 867–80

[228] Brunner P, Ritaccio A L, Lynch T M, Emrich J F, Wilson J A, Williams J C, Aarnoutse E J, Ramsey N F, Leuthardt E C, Bischof H and Schalk G 2009 A practical procedure for real-time functional mapping of eloquent cortex using electrocorticographic signals in humans *Epilepsy & Behavior* **15** 278–86

[229] Foutz T J, Arlow R L and McIntyre C C 2012 Theoretical principles underlying optical stimulation of a channelrhodopsin-2 positive pyramidal neuron *J Neurophysiol* **107** 3235–45

[230] Cardin J A, Carlén M, Meletis K, Knoblich U, Zhang F, Deisseroth K, Tsai L-H and Moore C I 2009 Driving fast-spiking cells induces gamma rhythm and controls sensory responses *Nature* **459** 663–7

[231] Kaiboriboon K, Lüders H O, Hamaneh M, Turnbull J and Lhatoo S D 2012 EEG source imaging in epilepsy—practicalities and pitfalls *Nat Rev Neurol* **8** 498–507

[232] Ji Z-G, Ito S, Honjoh T, Ohta H, Ishizuka T, Fukazawa Y and Yawo H 2012 Light-evoked Somatosensory Perception of Transgenic Rats That Express Channelrhodopsin-2 in Dorsal Root Ganglion Cells *PLoS ONE* **7** e32699

[233] Daou I, Tuttle A H, Longo G, Wieskopf J S, Bonin R P, Ase A R, Wood J N, Koninck Y D, Ribeiro-da-Silva A, Mogil J S and Séguéla P 2013 Remote Optogenetic Activation and Sensitization of Pain Pathways in Freely Moving Mice *J. Neurosci.* **33** 18631–40

[234] Llewellyn M E, Thompson K R, Deisseroth K and Delp S L 2010 Orderly recruitment of motor units under optical control in vivo *Nat Med* **16** 1161–5

[235] Arlow R L, Foutz T J and McIntyre C C 2013 Theoretical principles underlying optical stimulation of myelinated axons expressing channelrhodopsin-2 *Neuroscience* **248** 541–51

[236] Liske H, Towne C, Anikeeva P, Zhao S, Feng G, Deisseroth K and Delp S 2013 Optical inhibition of motor nerve and muscle activity in vivo *Muscle & Nerve* **47** 916–21

[237] Weber A I, Saal H P, Lieber J D, Cheng J-W, Manfredi L R, Dammann J F and Bensmaia S J 2013 Spatial and temporal codes mediate the tactile perception of natural textures *PNAS* 201305509

[238] Fenno L, Yizhar O and Deisseroth K 2011 The Development and Application of Optogenetics *Annual Review of Neuroscience* **34** 389–412

[239] Bernstein J G and Boyden E S 2011 Optogenetic tools for analyzing the neural circuits of behavior *Trends in Cognitive Sciences*

[240] Williams J C and Denison T 2013 From Optogenetic Technologies to Neuromodulation Therapies *Sci Transl Med* **5** 177ps6–177ps6

[241] Chow B Y and Boyden E S 2013 Optogenetics and Translational Medicine *Sci Transl Med* **5** 177ps5–177ps5

[242] Wilks S J, Koivuniemi A S, Thongpang S, Williams J C and Otto K J 2009 Evaluation of micro-electrocorticographic electrodes for electrostimulation *Annual International Conference of the IEEE Engineering in Medicine and Biology Society, 2009. EMBC 2009* Annual International

Conference of the IEEE Engineering in Medicine and Biology Society, 2009. EMBC 2009 pp 5510–3

[243] Mackevicius E L, Best M D, Saal H P and Bensmaia S J 2012 Millisecond Precision Spike Timing Shapes Tactile Perception *J. Neurosci.* **32** 15309–17

[244] Madisen L, Zwingman T A, Sunkin S M, Oh S W, Zariwala H A, Gu H, Ng L L, Palmiter R D, Hawrylycz M J, Jones A R, Lein E S and Zeng H 2010 A robust and high-throughput Cre reporting and characterization system for the whole mouse brain *Nat Neurosci* **13** 133–40

[245] Madisen L, Mao T, Koch H, Zhuo J, Berenyi A, Fujisawa S, Hsu Y-W A, Iii A J G, Gu X, Zanella S, Kidney J, Gu H, Mao Y, Hooks B M, Boyden E S, Buzsáki G, Ramirez J M, Jones A R, Svoboda K, Han X, Turner E E and Zeng H 2012 A toolbox of Cre-dependent optogenetic transgenic mice for light-induced activation and silencing *Nat Neurosci* **15** 793–802

[246] Kaczmarek K A, Webster J G, Bach-y-Rita P and Tompkins W J 1991 Electrotactile and vibrotactile displays for sensory substitution systems *IEEE Transactions on Biomedical Engineering* **38** 1–16

[247] Veraart C, Raftopoulos C, Mortimer J T, Delbeke J, Pins D, Michaux G, Vanlierde A, Parrini S and Wanet-Defalque M-C 1998 Visual sensations produced by optic nerve stimulation using an implanted self-sizing spiral cuff electrode *Brain Research* **813** 181–6

[248] Polasek K H, Hoyen H A, Keith M W, Kirsch R F and Tyler D J 2009 Stimulation Stability and Selectivity of Chronically Implanted Multicontact Nerve Cuff Electrodes in the Human Upper Extremity *IEEE Transactions on Neural Systems and Rehabilitation Engineering* **17** 428–37

[249] Ginn S L, Alexander I E, Edelstein M L, Abedi M R and Wixon J 2013 Gene therapy clinical trials worldwide to 2012 – an update *The Journal of Gene Medicine* **15** 65–77

[250] Towne C, Montgomery K L, Iyer S M, Deisseroth K and Delp S L 2013 Optogenetic Control of Targeted Peripheral Axons in Freely Moving Animals *PLoS ONE* **8** e72691

[251] Logothetis N K, Pauls J, Augath M, Trinath T and Oeltermann A 2001 Neurophysiological investigation of the basis of the fMRI signal *Nature* **412** 150–7

[252] Bohning D, Shastri A, McConnell K, Nahas Z, Lorberbaum J, Roberts D, Teneback C, Vincent D and George M 1999 A combined TMS/fMRI study of intensity-dependent TMS over motor cortex *Biological Psychiatry* **45** 385–94

[253] Paus T, Jech R, Thompson C J, Comeau R, Peters T and Evans A C 1997 Transcranial Magnetic Stimulation during Positron Emission Tomography: A New Method for Studying Connectivity of the Human Cerebral Cortex *J. Neurosci.* **17** 3178–84

[254] Desai M, Kahn I, Knoblich U, Bernstein J, Atallah H, Yang A, Kopell N, Buckner R L, Graybiel A M, Moore C I and Boyden E S 2011 Mapping brain networks in awake mice using combined optical neural control and fMRI *J Neurophysiol* **105** 1393–405

[255] Kahn I, Desai M, Knoblich U, Bernstein J, Henninger M, Graybiel A M, Boyden E S, Buckner R L and Moore C I 2011 Characterization of the Functional MRI Response Temporal Linearity via Optical Control of Neocortical Pyramidal Neurons *J. Neurosci.* **31** 15086–91

[256] Buxton R B, Wong E C and Frank L R 1998 Dynamics of blood flow and oxygenation changes during brain activation: The balloon model *Magnetic Resonance in Medicine* **39** 855–64

[257] Attwell D and Laughlin S B 2001 An Energy Budget for Signaling in the Grey Matter of the Brain *J Cereb Blood Flow Metab* **21** 1133–45

[258] Dudley D, Duncan W M and Slaughter J 2003 Emerging digital micromirror device (DMD) applications vol 4985 pp 14–25

[259] Boruah B R 2009 Dynamic manipulation of a laser beam using a liquid crystal spatial light modulator *American Journal of Physics* **77** 331–6

[260] Lothman E, LaManna J, Cordingley G, Rosenthal M and Somjen G 1975 Responses of electrical potential, potassium levels, and oxidative metabolic activity of the cerebral neocortex of cats *Brain Research* **88** 15–36

[261] Schindelin J, Arganda-Carreras I, Frise E, Kaynig V, Longair M, Pietzsch T, Preibisch S, Rueden C, Saalfeld S, Schmid B, Tinevez J-Y, White D J, Hartenstein V, Eliceiri K, Tomancak P and Cardona A 2012 Fiji: an open-source platform for biological-image analysis *Nat Meth* **9** 676–82

[262] Guizar-Sicairos M, Thurman S T and Fienup J R 2008 Efficient subpixel image registration algorithms *Opt. Lett.* **33** 156–8

[263] Drew P J, Shih A Y and Kleinfeld D 2011 Fluctuating and sensory-induced vasodynamics in rodent cortex extend arteriole capacity *PNAS* **108** 8473–8

[264] Sato Y, Nakajima S, Shiraga N, Atsumi H, Yoshida S, Koller T, Gerig G and Kikinis R 1998 Three-dimensional multi-scale line filter for segmentation and visualization of curvilinear structures in medical images *Medical Image Analysis* **2** 143–68

[265] Shuttleworth C W, Brennan A M and Connor J A 2003 NAD(P)H Fluorescence Imaging of Postsynaptic Neuronal Activation in Murine Hippocampal Slices *J. Neurosci.* **23** 3196–208

[266] Llano D A, Theyel B B, Mallik A K, Sherman S M and Issa N P 2009 Rapid and Sensitive Mapping of Long-Range Connections In Vitro Using Flavoprotein Autofluorescence Imaging Combined With Laser Photostimulation *J Neurophysiol* **101** 3325–40

[267] Lewis D V and Schuette W H 1975 NADH fluorescence and [K+]o changes during hippocampal electrical stimulation *J Neurophysiol* **38** 405–17

[268] Hansen A J and Zeuthen T 1981 Extracellular ion concentrations during spreading depression and ischemia in the rat brain cortex *Acta Physiologica Scandinavica* **113** 437–45

[269] Lauritzen M 1994 Pathophysiology of the migraine aura The spreading depression theory *Brain* **117** 199–210

[270] Filosa J A, Bonev A D, Straub S V, Meredith A L, Wilkerson M K, Aldrich R W and Nelson M T 2006 Local potassium signaling couples neuronal activity to vasodilation in the brain *Nat Neurosci* **9** 1397–403

[271] Aravanis A M, Wang L-P, Zhang F, Meltzer L A, Mogri M Z, Schneider M B and Deisseroth K 2007 An optical neural interface: in vivo control of rodent motor cortex with integrated fiberoptic and optogenetic technology *Journal of Neural Engineering* **4** S143–S156

[272] Lin J Y, Knutsen P M, Muller A, Kleinfeld D and Tsien R Y 2013 ReaChR: a red-shifted variant of channelrhodopsin enables deep transcranial optogenetic excitation *Nat Neurosci* **16** 1499–508

[273] Shih A Y, Driscoll J D, Drew P J, Nishimura N, Schaffer C B and Kleinfeld D 2012 Two-photon microscopy as a tool to study blood flow and neurovascular coupling in the rodent brain *J Cereb Blood Flow Metab* **32** 1277–309

[274] Łęski S, Wójcik D K, Tereszczuk J, Świejkowski D A, Kublik E and Wróbel A 2007 Inverse Current-Source Density Method in 3D: Reconstruction Fidelity, Boundary Effects, and Influence of Distant Sources *Neuroinform* **5** 207–22

[275] Tønnesen J, Sørensen A T, Deisseroth K, Lundberg C and Kokaia M 2009 Optogenetic control of epileptiform activity *PNAS* **106** 12162–7

[276] Wykes R C, Heeroma J H, Mantoan L, Zheng K, MacDonald D C, Deisseroth K, Hashemi K S, Walker M C, Schorge S and Kullmann D M 2012 Optogenetic and Potassium Channel Gene Therapy in a Rodent Model of Focal Neocortical Epilepsy *Sci Transl Med* **4** 161ra152–161ra152

[277] Krook-Magnuson E, Armstrong C, Oijala M and Soltesz I 2013 On-demand optogenetic control of spontaneous seizures in temporal lobe epilepsy *Nat Commun* **4** 1376

[278] Paz J T, Davidson T J, Frechette E S, Delord B, Parada I, Peng K, Deisseroth K and Huguenard J R 2013 Closed-loop optogenetic control of thalamus as a tool for interrupting seizures after cortical injury *Nat Neurosci* **16** 64–70

[279] Berndt A, Lee S Y, Ramakrishnan C and Deisseroth K 2014 Structure-Guided Transformation of Channelrhodopsin into a Light-Activated Chloride Channel *Science* **344** 420–4

[280] Anenberg E, Arstikaitis P, Niitsu Y, Harrison T C, Boyd J D, Hilton B J, Tetzlaff W and Murphy T H 2014 Ministrokes in Channelrhodopsin-2 Transgenic Mice Reveal Widespread Deficits in Motor Output Despite Maintenance of Cortical Neuronal Excitability *J. Neurosci.* **34** 1094–104

[281] Van den Maagdenberg A M J M, Pietrobon D, Pizzorusso T, Kaja S, Broos L A M, Cesetti T, van de Ven R C G, Tottene A, van der Kaa J, Plomp J J, Frants R R and Ferrari M D 2004 A Cacna1a Knockin Migraine Mouse Model with Increased Susceptibility to Cortical Spreading Depression *Neuron* **41** 701–10

[282] Hawkins B T and Davis T P 2005 The Blood-Brain Barrier/Neurovascular Unit in Health and Disease *Pharmacol Rev* **57** 173–85

[283] Kasischke K A, Lambert E M, Panepento B, Sun A, Gelbard H A, Burgess R W, Foster T H and Nedergaard M 2011 Two-photon NADH imaging exposes boundaries of oxygen diffusion in cortical vascular supply regions *J Cereb Blood Flow Metab* **31** 68–81

Appendix: Validation of spike-field complex cross coherence analysis

Calculating complex cross coherence was an essential tool for describing the phase-coupling relationship between spikes and micro-ECoG signals in Chapter 3. We relied on the Chronux 2.1 toolbox developed by Partha Mitra and many others. This toolbox uses multitaper Fourier methods to estimate the power spectral density and related measurements including complex cross coherence. The quality of this toolbox is very high and is widely applied, so its results aren't in question except for our use of it. To verify that were properly applying the Chronux 2.1 toolbox, we tested the complex cross coherence function (coherencysegcpt.m) with signals that we generated *de novo*. We systematically varied the parameters listed in table A1. Each parameter was varied over a specified range. All other parameters well held fixed. Given the number of parameters involved, exploring the entire parameter space was impossible, instead we chose reasonable default values.

A sinusoid oscillating at f_1 Hz represented the micro-ECoG signal. White noise was added to create a well defined signal to noise ratio. Spikes times were generated similar to a Poisson process, but the probability of a spike occurring was modulated through time, dependent on the phase of a second sinusoid oscillating at f_2 Hz. The phase difference between the two sinusoids was ρ if f_1=f_2, otherwise ρ represents the phase of the second sinusoid at $t = 0$. The time average spike spike rate S and the duration of the data T_{dur} were also systematically varied.

Table A1. Parameter space of spike-field coherence testing and corresponding figures.

Parameter	description	default value	varied range r_1:increment: r_2	corresponding figures
f_1	frequency of the sinusoid representing the micro-ECoG signal	15 Hz	2.5:5:97.5 Hz	A2, A4
f_2	frequency of the sinusoid modulating the spiking probability	15 Hz	2.5:5 :97.5 Hz	A3, A4
f_s	the sampling frequency	3051 Hz	250:250:5000 Hz	A5
ρ	the phase difference between f_1 and f_2	180 degrees	10:10:350 degrees	A6
S	the average spiking rate	5 Hz	20 values logarithmically spaced from 1 to 200 Hz	A7
SNR	the signal to noise ratio of the power in sinusoid 1 versus the white noise	1.0	30 values logarithmically spaced from 0.00001 to 100	A8
T_{dur}	duration of data segment	60 s	20 values logarithmically spaced from 5 to 300	A9

The following fixed parameters define exactly how complex cross coherence was calculated with the Chronux toolbox. The data was segmented into 1 second pieces and the coherency averaged over segments. The FFTs were padded to the next highest power of 2. A time-bandwidth product of 5 and 3 tapers were used. Jackknife confidence intervals were found at the α=0.05 level, and the confidence intervals were corrected for finite data length bias based on the number of degrees of freedom.

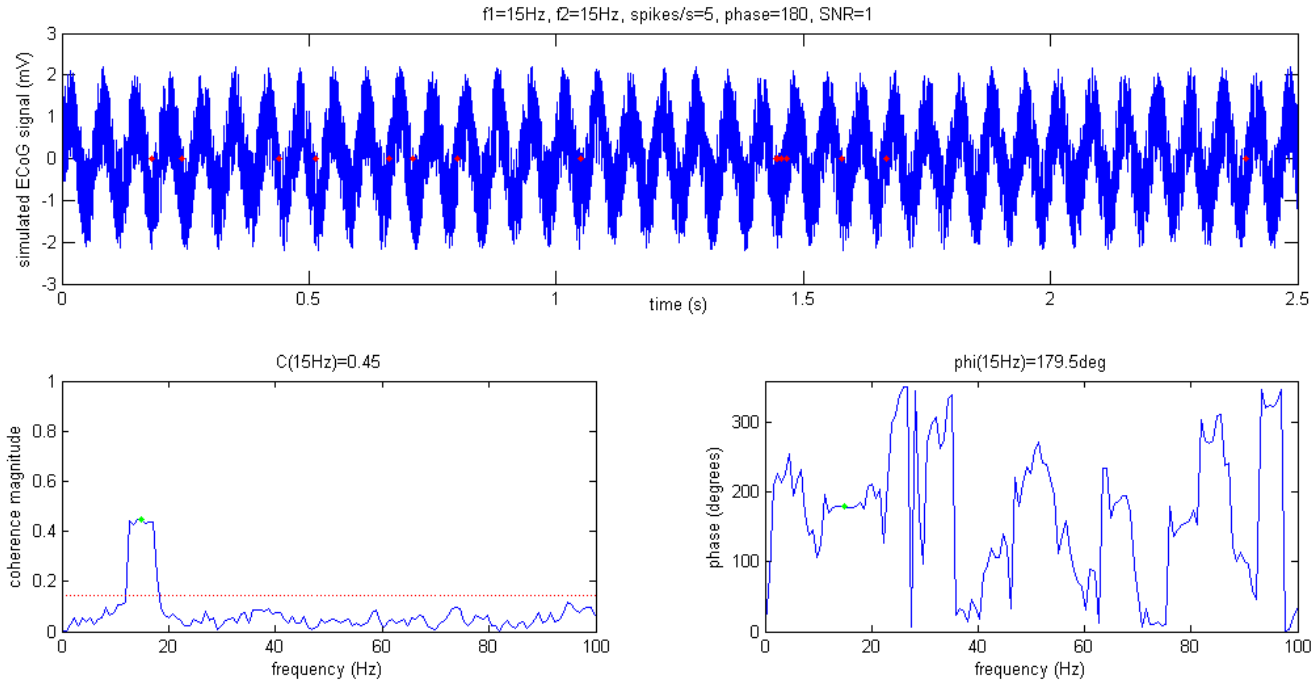

Figure A1. Example of generated data and coherence results for the default parameters in table A1. (above) A sinusoid with added white noise is plotted in blue. Spike times are plotted as red dots. (Lower left) The resulting coherence is plot in blue with the value at 15 Hz marked with a green dot. The minimum coherence level for significance at α=0.05 is plotted as a dotted red line. (Lower right) The phase of the coherency is plotted in blue. A phase difference of 180 degrees is observed at 15 Hz, marked in green. The phase information at insignificant coherence magnitudes is meaningless.

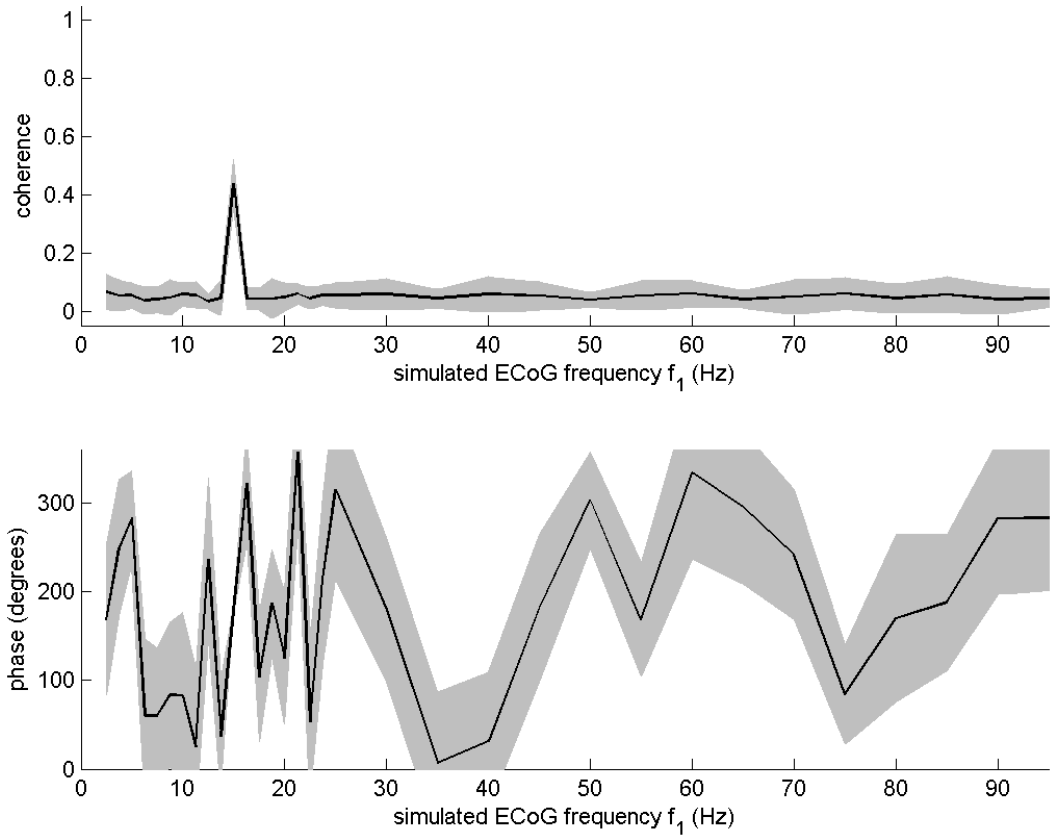

Figure A2. Systematic variation of f_1. Coherence was only found when f_1=f_2. Notice how the phase=180 degrees when f_1=f_2. The phase information is not meaningful unless the coherence is significant.

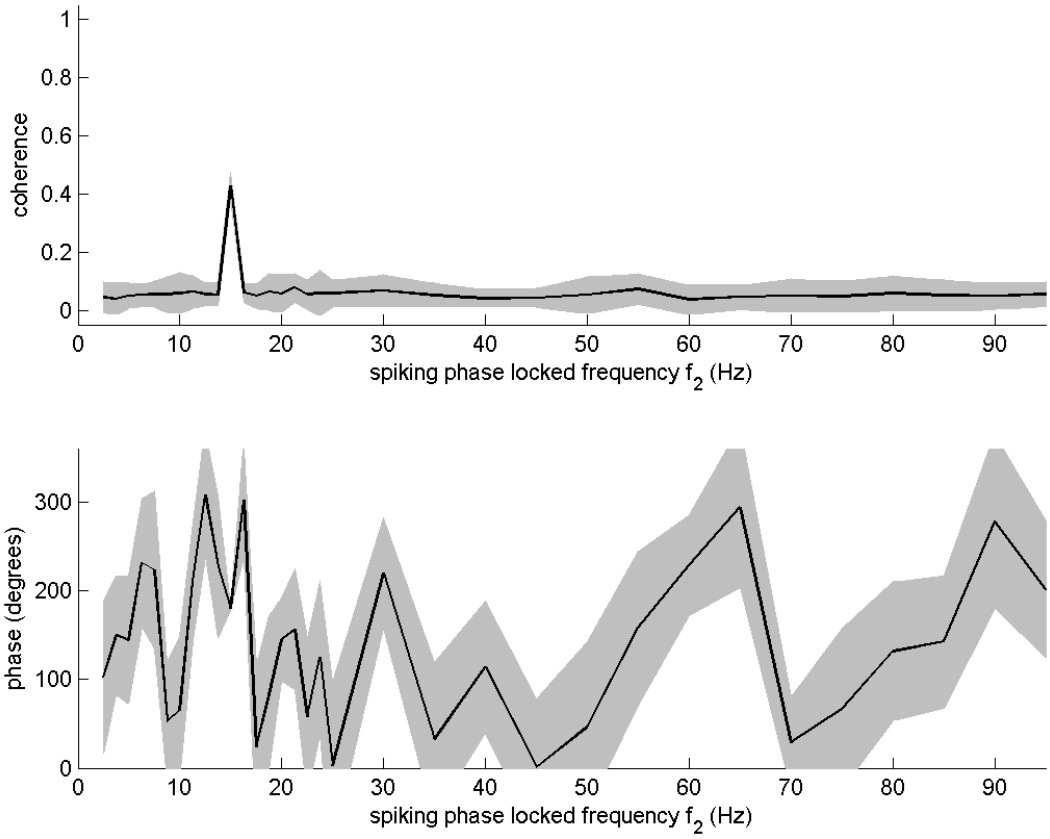

Figure A3. Systematic variation of f_2. Coherence was only found when f_1=f_2.

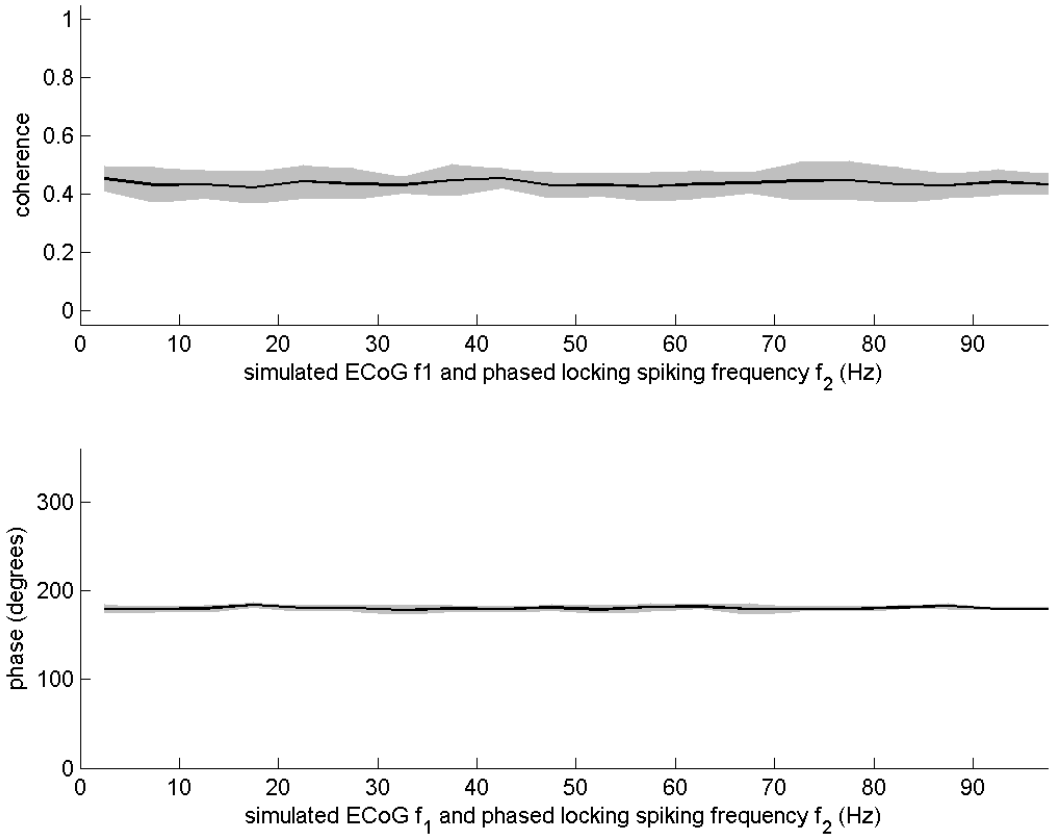

Figure A4. Systematic variation of f_1 and f_2 together. The coherence was invariant.

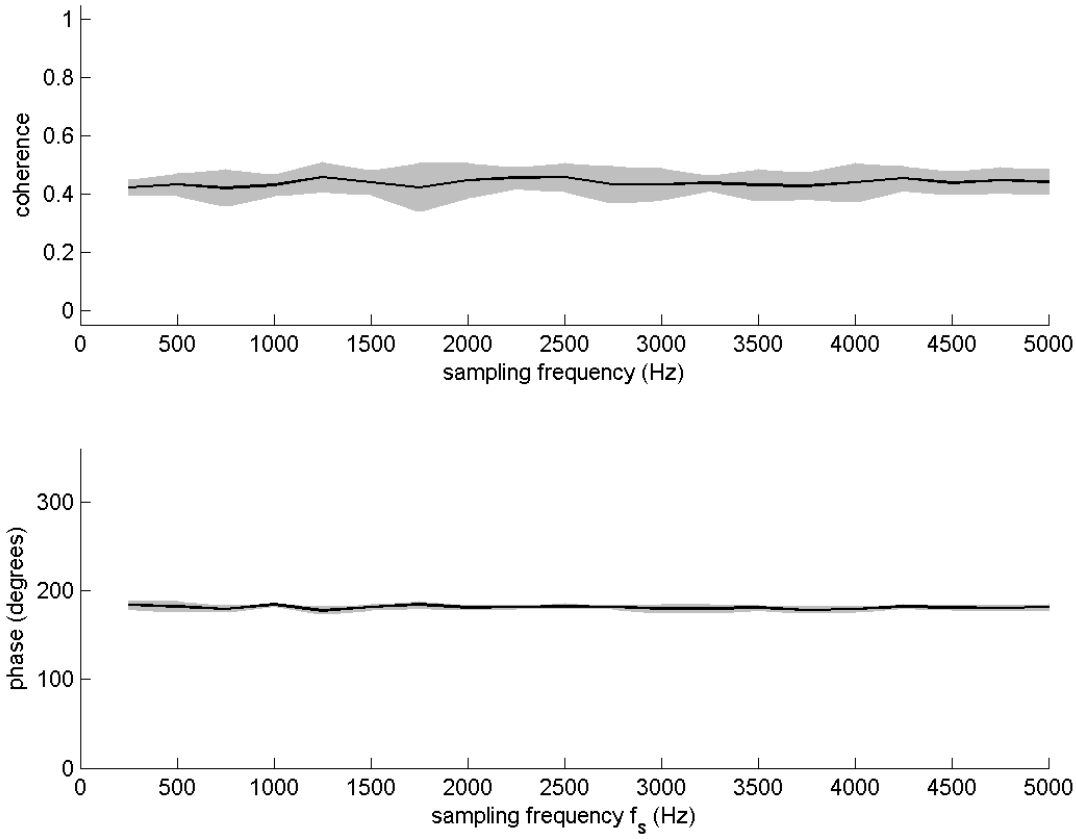

Figure A5. Systematic variation of f_s. The coherence was invariant.

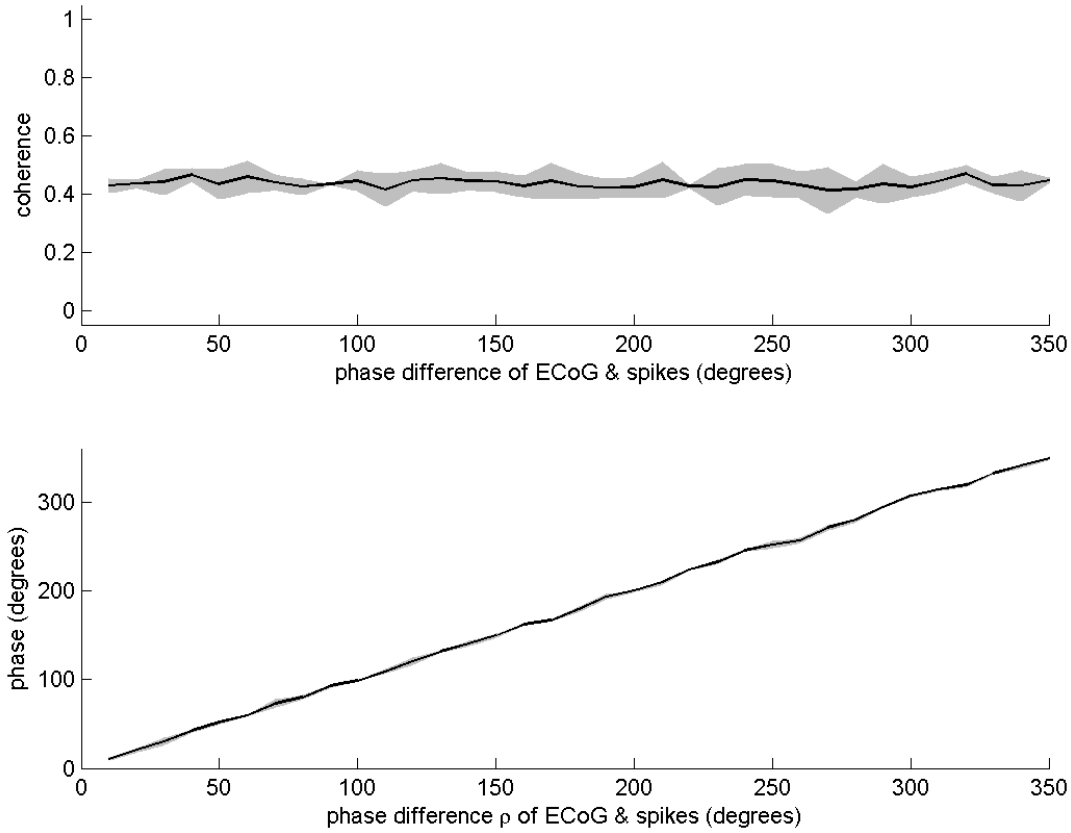

Figure A6. Systematic variation of ρ. The coherence was invariant and the specified phase difference (lower, x-axis) equals the coherence phase difference (lower, y-axis).

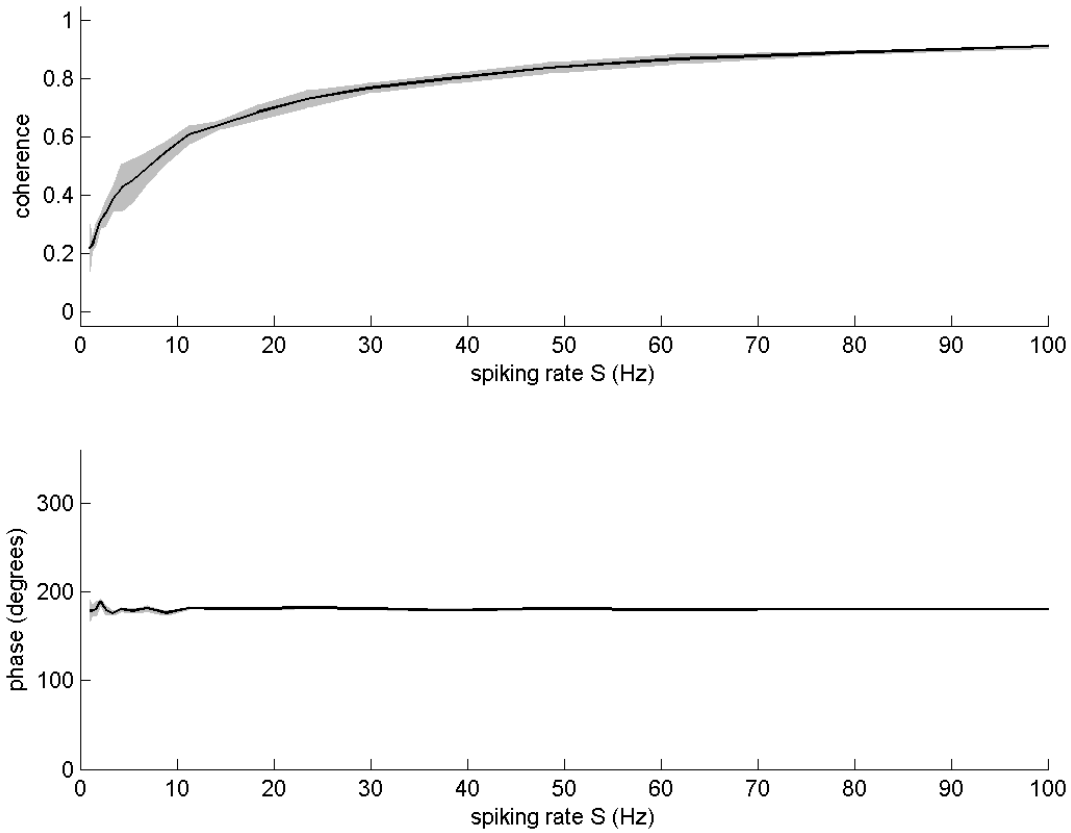

Figure A7. Systematic variation of S. The coherence has an monotonic increasing relationship with the spiking rate. This trend appears to fit a square root function. The phase was invariant. The confidence intervals were larger at low spiking rates.

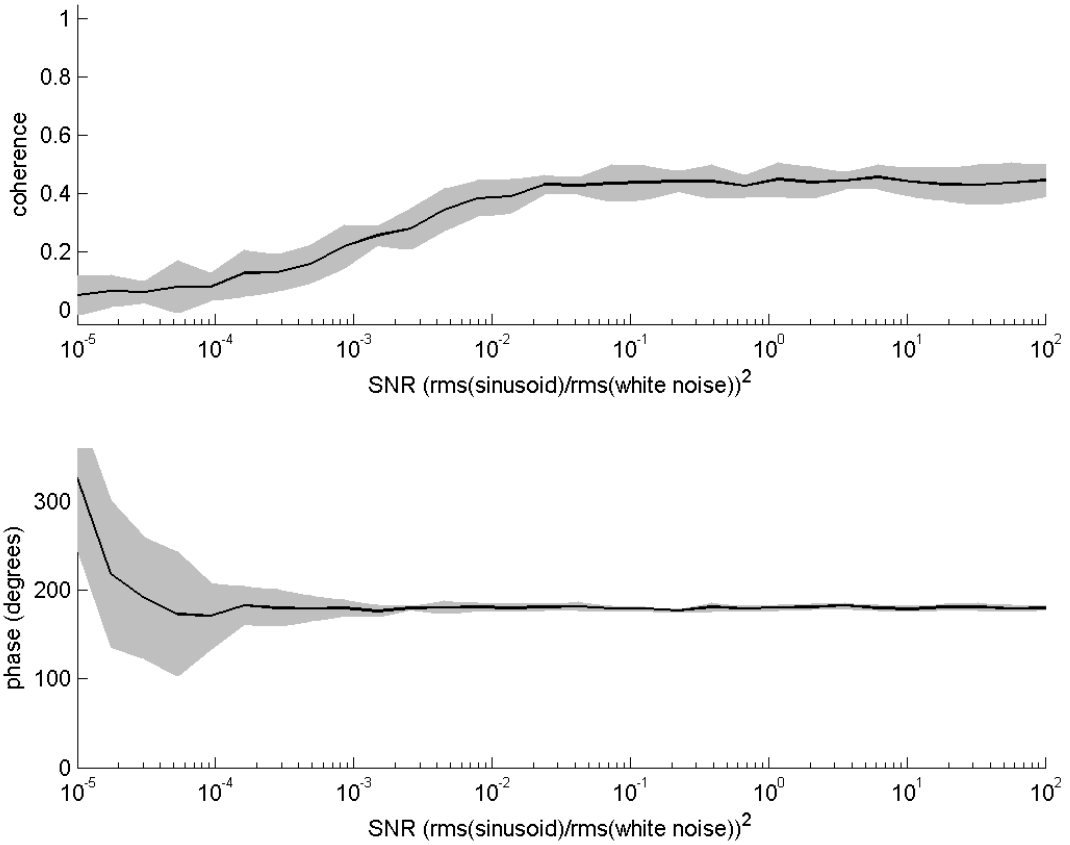

Figure A8. Systematic variation of SNR. The coherence was invariant above 0.01, but decreased as the SNR approached 0.00001. The confidence intervals of the phase increased as the SNR decreased.

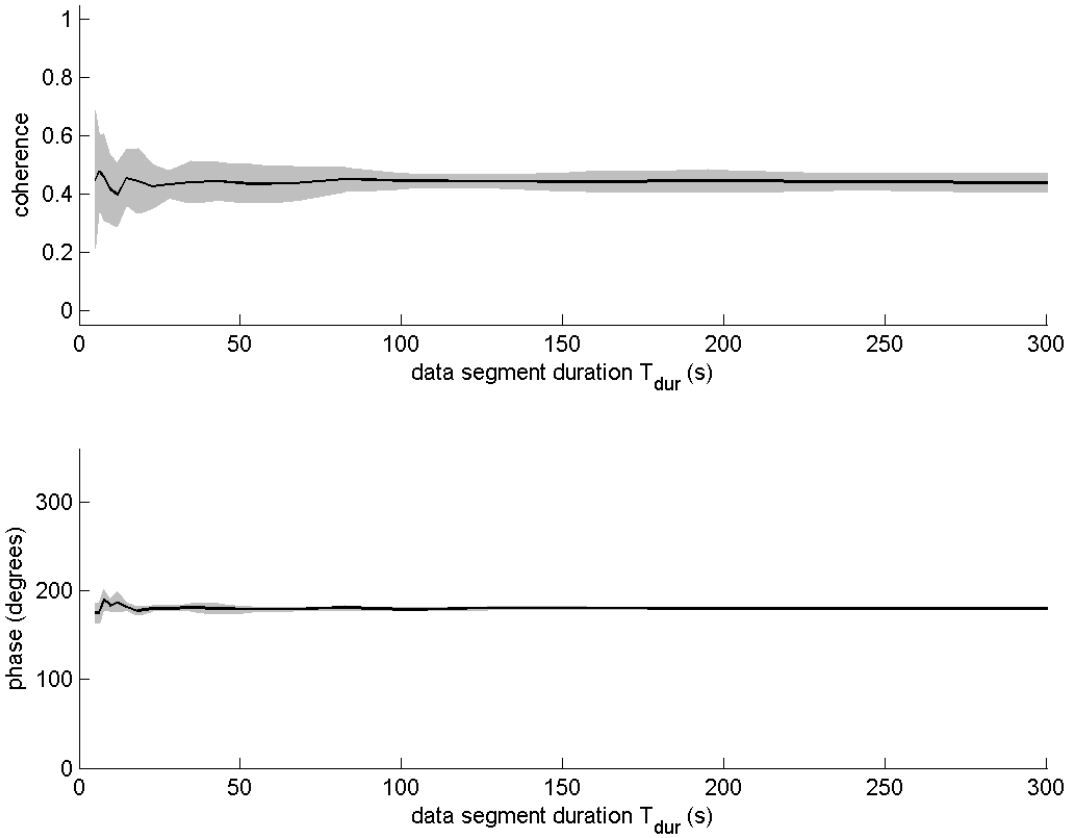

Figure A9. Systematic variation of T_{dur}. Coherence was invariant, but the confidence intervals increased for short data lengths.

In conclusion, figures A1-A9 suggest that the complex cross coherence algorithm used in chapter 3 is very robust over a range of parameters. The major assumption of this analysis is stationarity of the spike-phase distribution.